uOttawa

L'Université canadienne
Canada's university

FACULTÉ DES ÉTUDES SUPÉRIEURES ET POSTOCTORALES

uOttawa

L'Université canadienne
Canada's university

FACULTY OF GRADUATE AND POSDOCTORAL STUDIES

Sarah Elizabeth Agosta
AUTEUR DE LA THÈSE / AUTHOR OF THESIS

M.Sc. (Geography)
GRADE / DEGREE

Department of Geography
FACULTÉ, ÉCOLE, DÉPARTEMENT / FACULTY, SCHOOL, DEPARTMENT

Preservation and Diagenesis in Ancient Speleothems: Evidence from Bear Cave, Yukon Territory

TITRE DE LA THÈSE / TITLE OF THESIS

Bernard Lauriol
DIRECTEUR (DIRECTRICE) DE LA THÈSE / THESIS SUPERVISOR

Ian D. Clark
CO-DIRECTEUR (CO-DIRECTRICE) DE LA THÈSE / THESIS CO-SUPERVISOR

Joyce Lundberg

André Viau

Gary W. Slater
Le Doyen de la Faculte des études superieures et postdoctorales / Dean of the Faculty of Graduate and Postdoctoral Studies

Preservation and diagenesis in ancient speleothems: evidence from Bear Cave, Yukon Territory

Sarah Agosta

Thesis presented to the Faculty of Graduate and Postdoctoral Studies
in partial fulfillment of the requirements for the degree of
Master of Science in Physical Geography

Department of Geography
Faculty of Arts
University of Ottawa

Supervisors:
Dr. Bernard Lauriol (Department of Geography)
Dr. Ian D. Clark (Department of Earth Sciences)

Thesis Committee:
Dr. Andre Viau (Department of Geography, University of Ottawa)
Dr. Joyce Lundberg (Department of Geography, Carleton University)

Your file Votre référence
ISBN: 978-0-494-74177-1
Our file Notre référence
ISBN: 978-0-494-74177-1

Abstract

Speleothems are rare in high-latitude and high-altitude caves, which is why Bear Cave in the north-western Yukon Territory is particularly unique, as it houses some of the oldest and highest latitude speleothem in the world. In this study, a detailed petrographic and geochemical study was conducted along the profile of a 68-cm long late-Miocene flowstone from Bear Cave (BC1) to reveal the processes that took place at the time of deposition, in addition to those that followed, in aims to determine its paleoclimatic suitability. These studies suggest that softer facies are generally representative of disequilibrium conditions, where in-filled textures provide evidence for diagenic phenomena; these processes ultimately obscure the original climate signal, compromising the integrity of the flowstone in terms of its paleoclimatic suitability. Conversely, harder facies are likely deposited in isotopic equilibrium and resistant to post-depositional diagenesis, and are therefore more reliable for detailed paleoclimatic analysis. The variability of the calcite sequences in the profile of BC1 imply that environmental conditions have been considerably variable of the course of deposition, reflecting alternating cool/dry (softer facies) and warm/wet (harder facies) climatic conditions. Results from radiogenic ^{4}He-dating constrain the timeframe of deposition, with ages centering around 9.35 ± 0.52 Ma, which are in line with regional geomorphic interpretations. This study emphasizes the importance of a complimentary petrographic study in speleothem geochemical studies used in paleoclimatic and paleoenvironmental research.

Acknowledgements

This project would not have been possible without funding from NSERC (Natural Sciences and Engineering Research Council of Canada), NSTP (Northern Scientific Training Program), PCSP (Polar Continental Shelf Project) and the University of Ottawa.

Several people have also been instrumental in allowing this project to be completed. Special thanks to Dr. P. Middlestead from the G.G. Hatch laboratory, Dr. R. Mohapatra from the MAPL Noble Gas laboratory, and Dr. N. DeSilva from the Department of Earth Sciences at the University of Ottawa for their invaluable assistance in and outside of the lab. I must also acknowledge Dr. D. Lacelle for his counsel, Dr. T. Kluge and Dr. Werner Aeschbach-Hertig from the Department of Environmental Physics at the University of Heidelberg in Germany for their work on initial ^{4}He-dating on the BC1 flowstone, as well as Dr. D. Pinti & Dr. B. Ghaleb from UQAM for their additional discussion and measurements of ^{4}He-dating. My sincere gratitude is extended to the members of my committee, Dr. A. Viau and Dr. J. Lundberg, for their insightful comments and suggestions.

I must especially thank my research supervisors, Dr. B. Lauriol and Dr. I.D. Clark. I am forever indebted for their encouragement, patience, and guidance throughout the duration of this project, as well as the many opportunities that have been bestowed to me over the course of my two years at the University of Ottawa. It has been an honour being one of your students.

A warm message of thanks goes out to all my friends (too many to list here but you know who you are!) for providing the support and friendship that I needed to keep my sanity over the past two years. To my hard-working parents, Jo-Ann & Corrado, who sacrificed their lives for my sister and myself, I thank them for their unconditional love and care. To my wonderful sister Emily, who has become my best friend, I thank her for all her advice and support. I would not have made it this far without them and I love them all dearly. And finally, to Ken, thank you for always having faith in me, giving me the inspiration and motivation for completing this thesis, and periodically reminding me of my nerdy love of rocks...I love you.

Table of Contents

List of Figures

List of Tables

1. INTRODUCTION

Speleothems are secondary mineral deposits, chemically precipitated in caves, principally from carbonate seepage waters (Hill & Forti, 2004, p.690). Growing interest has been paid to these deposits over the past several decades, especially to carbonate speleothem, as they serve as valuable multi-proxy archives of climatic and environmental change, gained through petrographic (Hopley 2009; Martin-Garcia *et al.*, 2009; Jo *et al.*, 2010), and geochemical analyses (Fairchild *et al.*, 2006; White, 2007, p.136-175; Blyth *et al.*, 2008; Fairchild & Treble, 2009), with increasing interest in ancient speleothems (Lauriol *et al.*, 1997; Hopley *et al.*, 2007; Meyer *et al.*, 2009). The deposition of calcite and the uptake of various isotopes, trace elements and organic compounds from seepage waters can reveal important information about the conditions under which the speleothem was formed as the pathway of these seepage waters acts as a buffering zone, which serve to amplify, attenuate, or filter these environmental signals from the surface (Frappier, 2007). The cave environment protects these deposits from surface erosional processes and post-depositional diagenesis, providing a stable depositional environment for speleothem precipitated from seepage waters entering the cave from the land surface above (White, 2007, p.136; Turgeon & Lundberg, 2007, p.274). Speleothem deposits are ideal paleoclimatic and paleoenvironmental archives as their growth is sensitive to subtle changes occurring at the surface, such as variations in temperature, precipitation and vegetation (White, 2007, p.136), recording these conditions at the time of deposition. They are advantageous for paleo-research as they often have (i) high resolution stratigraphy (in some cases at the seasonal scale), (ii) potential for extensive spatial and temporal records, (iii) solid crystalline structure ideal for precise U-series dating and chemical analyses, and (iv) high preservation potential and resistance to post-depositional recrystallization and diagenesis (Turgeon & Lundberg, 2007, p.274). Stalagmites are typically considered as the ideal type of speleothem for paleoclimatic and paleoenvironmental archives; however a number of studies demonstrate the potential of flowstones in paleoclimatology (Baker *et al.*, 1995; Lauritzen, 1995; Spötl *et al.*, 2002; Holzkämper *et al.*, 2005; Drysdale *et al.*, 2006; Meyer *et al.*, 2008).

Although speleothems have been found to grow under extreme conditions (Spötl & Mangini, 2007), these deposits are generally rare in high-latitude/altitude caves where growth is impeded by colder conditions due to low organic activity and the obstruction of feedwater

conduits by permafrost growth. This is what makes Bear Cave in the north-western Yukon Territory a particularly interesting case, as it houses some of the oldest and highest latitude speleothems in the world, believed to be late-Tertiary in age (Lauriol *et al.*, 1997). The cave, located just below the Arctic Circle, is situated in the ice-free corridor of Beringia, shielding it from the onslaught of the Quaternary glaciations. Its isolation from glacial advance has allowed for the preservation of many calcite speleothems, including a 68 cm thick flowstone (BC1), likely one of the oldest in the cave.

Unique deposits such as these remain a keen interest in the scientific community in terms of their potential for paleoenvironmental and paleoclimatic reconstruction, providing insight into the conditions in the Beringian region preceding the establishment of permafrost. Geochemical proxies extracted from these deposits can be used to infer past conditions of climatic and environmental change, assuming that no diagenic modification has taken place, that the calcite has been deposited under isotopic equilibrium conditions, and that drip source/flow paths have remained constant (particularly in the case of flowstones). However many studies fail to investigate these assumptions, which if left unchecked, may act to obscure the original climate signal preserved in these deposits (modern or ancient), potentially having serious implications for the misinterpretation of speleothems records. Thus it is imperative to confirm the preservation of primary calcite and the integrity of geochemical signals prior to interpreting paleo-information from speleothems.

1.1. Thesis Structure and Research Objectives

The overall goal of this study is part of an ongoing collaborative effort to retrace the depositional history at Bear Cave Mountain, in aims to expand our knowledge of the environmental and climatic conditions at the limits of Beringia preceding the Quaternary, when permafrost was absent from the area. More specifically, the focus of this thesis is to explore the following research questions:

(I) What is the paleoclimatic suitability of the BC1 flowstone? Is it representative of initial equilibrium deposition, or has it undergone alteration by recrystallization or post-depositional diagenesis? What are the effects of this alteration on the crystalline structure and geochemistry? Are certain microfabrics more reliable for paleoclimatic analysis than others?

(II) What is the age of the BC1 flowstone? Can we constrain a timeframe of deposition or establish a chronology?

(III) What is the depositional history at Bear Cave? What can the BC1 flowstone convey with confidence about the environmental/climatic conditions at the time of deposition?

The BC1 flowstone is ideal to analyse for diagenic alterations and equilibrium depositional conditions as several different crystallographic textures can be observed throughout its profile, which includes alternating sequences of hard and soft calcite, ultimately linked to varying depositional conditions (Frisia *et al.*, 2000). Any section of the BC1 flowstone that was not originally deposited under equilibrium conditions or that may have been subject to post-depositional diagenesis should display distinctive petrographic characteristics and isotopic trends, which will not be representative of initial deposition. Harder sequences are generally regarded as reliable paleoclimate proxies as they form at near-equilibrium conditions, and are resistant to diagenic modification (Lohmann, 1987, p.77; Frisia *et al.*, 2000; Turgeon & Lundberg, 2001); therefore these facies should be the most reliable for detailed paleoclimatic analysis.

To address these central research questions and hypotheses, a multi-proxy approach is adopted with the methods outlined in the following paragraphs:

(1) A petrographic study is used to examine the characteristics of the individual microfabrics of BC1, in particular to disclose indications of preservation or alteration within several different microfabrics, revealing the conditions leading to and following formation.

(2) The detailed petrographic study along the growth axis of the BC1 flowstone is used concurrently with stable O-C isotope record to examine the geochemical signatures of the various microfabric types. Investigation of the changes in crystal fabrics and the variations in their respective isotopic signatures will aid in understanding their reliability as speleothem climate proxies.

(3) Trace element and stable isotope variations in two distinctly different fabrics (primary and diagenic calcite) are compared at a higher resolution in order to investigate their differences in geochemistry.

(4) A large focus of this study is to build upon a chronology of the BC1 flowstone, as little is known about the time during which it was deposited. To achieve this, a number of methods are employed, including: examination of invisible laminations by epi-fluorescence spectroscopy to obtain an indication of the crystal growth rate; a discussion of the geomorphic history of the Bear Cave region; relative age comparison by magnetostratigraphy; and absolute dating by radiogenic He-dating.

Due to the broad nature of this study, this chapter lays the foundation for this thesis, covering an extensive review of related concepts and background information. *Chapter 2* provides a description of the geology and regional climatic and vegetational history of the Bear Cave region, as well as a general description of the BC1 flowstone. *Chapter 3* outlines the methodology employed for this thesis, followed by a presentation of the results in *Chapter 4*, discussion and interpretation of the results in *Chapter 5*, with closing remarks offered in *Chapter 6*.

1 2 Speleothem development and preservation

1.2.1. Depositional mechanisms

Most speleothems form under similar depositional mechanisms: calcite is precipitated in thin sheets from seepage waters, occasionally forming annual laminations, similar to tree rings The rate of deposition is dependent on two main factors· (i) the concentration of Ca^{2+} in cave drip-waters, and (ii) the type of flow over its surface (Turgeon & Lundberg, 2007, p 275) Given that most speleothems are characterized by smooth surfaces, laminar flow is the dominant flow mechanism, leaving Ca^{2+} concentrations as the main control on deposition. This is ultimately governed by dissolution in the soil, epikarst and carbonate bedrock zones, the conditions that enhance or diminish dissolution ultimately control speleothem growth. The three main stages involved in speleothem deposition (illustrated in *Figure 1 1*) can be summarized by the following set of reactions

$$H_2O + CO_2 \rightarrow H_2CO_3 \textit{ (carbonic acid)} \quad [1]$$

$$CaCO_3 + H_2CO_3 \rightarrow Ca^{2+} + 2HCO_3 \textit{ (calcium bicarbonate dissolution)} \quad [2]$$

$$Ca^{2+} + 2HCO_3 \textit{ (aq)} \rightarrow CO_2 \textit{ (g)} + H_2O \textit{ (l)} + CaCO_3 \textit{ (s) (calcite)} \quad [3]$$

The process begins as rainfall, having a P_{CO_2} of ~$10^{-3.5}$ bars (White, 2007, p.139), is introduced into the soil column. As meteoric waters percolate downward throughout the soil column above the carbonate bedrock, a considerable amount of additional CO_2 is absorbed as the partial pressure of the soil CO_2 is much higher than atmospheric CO_2, reaching P_{CO_2} concentrations upwards of 10^{-1} (White, 2007, p.139); this is caused by the biological component of soils, involving plant root respiration, microbial processes and decaying organic matter This mixing of soil CO_2 and water results in the formation of carbonic acid (*Equation 1*) As the solution comes into equilibrium with the P_{CO_2} in the soil, the $CaCO_3$ dissolution capacity of the solution is increased; it becomes undersaturated with respect to $CaCO_3$, sometimes referred to as 'aggressive' water (Ford & Williams, 1989, p.44). This weak carbonic acid reacts with $CaCO_3$ as it seeps through the joints, cracks and pores of the carbonate bedrock, producing a calcium bicarbonate solution (*Equation 2*) The solution will continue to dissolve the $CaCO_3$, holding more Ca^{2+} ions in solution, until saturation is reached

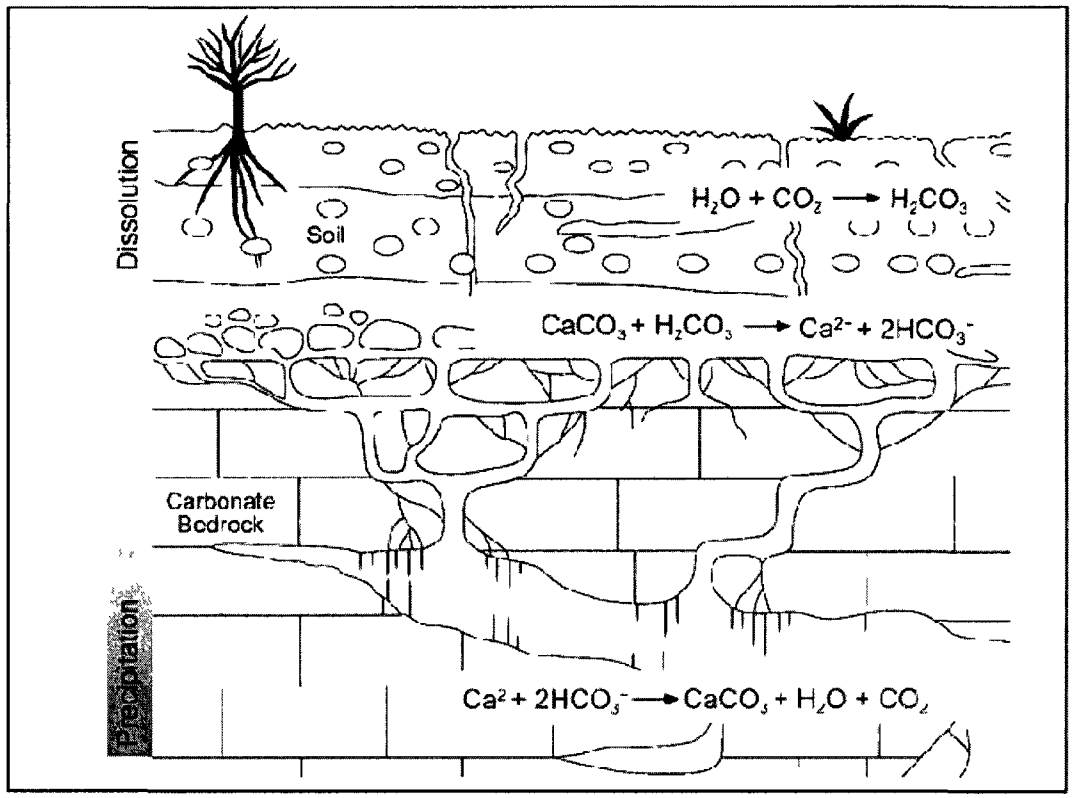

Figure 1.1. A simplified conceptual model for the deposition of calcite speleothems (Fairchild *et al.*, 2006).

The final phase of speleothem deposition involves the deposition of calcite. Because karstic waters enter the bedrock below the epikarst close to saturation, they migrate downward along fractures carrying the dissolved ions with little further dissolution (White, 2007, p.139). As the saturated $CaCO_3$-bearing drip waters reach the cave atmosphere, CO_2 is degassed as the P_{CO_2} of the liquid is out of equilibrium with that of the cave's atmosphere, which has a lower P_{CO_2} than the dripwaters, ~$10^{-2.5}$ bars (Turgeon & Lundberg, 2007, p.277; White, 2007, p.141). This degassing of CO_2 reduces the ability of the solution to hold the dissolved $CaCO_3$, and the solution becomes supersaturated with respect to calcite. In this circumstance, the solubility limit of the solution has been exceeded, and as a result, the chemical reaction reverses (*Equation 3*). Carbonate minerals then precipitate out of solution, forming a variety of speleothem deposits in the cave environment.

1.2.2. Post-depositional diagenesis and recrystallization

Although the cave environment acts to shield speleothems from land-surface processes which may alter or degrade them, it is possible for various meteoric and phreatic diagenic processes to significantly modify the primary texture in speleothems following deposition, resulting in the loss of primary texture and geochemical signatures in speleothems (Martin-Garcia et al. 2009). For instance, aragonite or high-Mg calcite both have a high reaction potential, and are likely to undergo diagenic alterations (Fairchild *et al.*, 2006). Aragonite-calcite transformations, or *Neomorphism*, is one example of potential changes that may occur after initial deposition, and the most commonly reported in speleothem studies. Metastable aragonite commonly precipitates in cave environments, and is known to change its crystal structure to that of calcite, the more stable polymorph (Hill & Forti, 1997, p.145). This change usually occurs across thin films of aqueous solution, with aragonite dissolving on one side and calcite precipitating on the other (Hill & Forti, 1997, p.316). This may include one of two processes: (1) *Calcitization*, with preservation of relict aragonite textures, or (2) *Dissolution-cementation*, which is a two-stage process where the original aragonitic texture is destroyed, and is characterized by calcite crystals in-filling the mold left by aragonite dissolution (Hopley *et al.*, 2009), commonly by equant/sparitic crystals (Frisia *et al.*, 2000). Where aragonite is replaced by calcite, it is unlikely that original chemical time series can be recovered due to the variable loss of species such as ^{13}C, ^{18}O, U, Sr, Ba and gain of Mg (Fairchild *et al.*, 2006).

Recrystallization of calcite is a lesser-known phenomenon, but does occur. *Metamorphism* of calcite can be brought on by changes in physical and chemical conditions. In the spelean environment, chemically active fluids are known to be the major culprit of recrystallization, where pooling waters on the surface of speleothems and migrating secondary infiltration waters result in dissolution at the growth front, increases in porosity, as well as physical and chemical transformations (Martin-Garcia *et al.*, 2009). Calcite crystals in speleothems generally grow with their long axis aligned with the direction of growth, therefore the presence of a mosaic of randomly-oriented and roughly equidimensional crystals may indicate recrystallization has occurred (Lauritzen & Lundberg, 1999). Equant calcites may be generated by porosity in-filling, with the enlargement of crystals by ripening over time, and may be more typical of more porous and impurity-rich flowstones (Frisia, 1996). These phenomena are uncommon in more compact speleothems, although modification may occur at the contact with fluid inclusions and hiatuses in growth; however petrographic evidence of modification of

primary inclusion shape by dissolution/precipitation reactions has yet to be observed in speleothem calcite (Fairchild *et al.*, 2006). In any case, the geochemistry of speleothems subject to diagenesis will be more variable and may display higher degrees of water-rock interaction (in an open, water-dominated system) than that of primary, unaltered speleothems (Lohmann, 1988, p.77). For these reasons, it is essential that a petrographic study is conducted prior to interpreting paleoclimatic information from speleothems.

1.2.3. Geographical context

Karst landscapes are generally well developed in tropical regions as these warm and wet areas facilitate high rates of weathering; these conditions permit the development of extensive speleothem chronologies. Higher bedrock dissolution rates in response to increases in temperature, vegetation and microorganism activity levels are common in warm and humid environments where soil CO_2 levels are elevated (Turgeon & Lundberg, 2007, p.276). Soils with abundant organics display higher P_{CO_2} levels and require higher concentrations of Ca^{2+} to reach saturation, therefore have higher depositional rates. However these areas also experience higher erosional rates (White, 2007, p.139): this increases the possibility of diagenesis and diffusion of secondary infiltration waters into the rock which may disrupt the primary climatic signal (Lohmann, 1988, p.58).

Speleothem deposition is rare in high-latitude and high-altitude caves. Speleothems such as stalagmites, stalactites and flowstones only form when the cave's interior temperature remains above the freezing point of water, and when groundwater circulation is unrestricted and the conduits that supply the dripwaters to the cave are not completely blocked (Spötl, 2007). In glacial and periglacial environments, seepage waters may be blocked by permafrost, ice cover, and glacial melt waters. In addition, colder conditions lead to dramatic decreases in biogenic CO_2 due to sparse vegetation (Spötl, 2007), which is why regions subject to periodic cold or arid conditions may only experience episodic deposition. The relationship between speleothem growth and permafrost is the primary control on deposition in colder environments, as speleothem feedwaters are extremely vulnerable to interference by the presence of permafrost (Lauriol *et al.*, 1997). In order to maintain the high levels of P_{CO_2} in the soil atmosphere necessary for later deposition in the cave atmosphere, the channels where feedwaters originate in the epikarst zone must be very small (normally much less than 1 mm in diameter). These thread-

like channels are among the first to become obstructed by ground ice and will be among the last to thaw. As a consequence, speleothem deposition will halt after permafrost becomes widespread above a cave; for this reason permafrost is one of the main factors that punctuate speleothem deposition at northern latitudes (Lauriol *et al.*, 1997). From a preservation standpoint, these regions may serve to slow down the weathering and erosional processes that degrade karstic regions in the humid sub-tropics, so long as the region has remained unglaciated, and the cave is not overwhelmed by high rates of frost shattering.

1.3. Structure and composition of speleothems

1.3.1. Mineralogy, crystal morphology and environmental conditions of formation

Calcite, aragonite, vaterite, huntite, magnesite, and dolomite are examples of calcium carbonate minerals commonly found in cave deposits (Hill & Forti, 2004, p.690), including ikaite in cold climate carbonate precipitates (Lacelle, 2007). Calcite is the most abundant mineral found in speleothems as it is the most stable form of calcium carbonate under the temperature, total pressure and carbon dioxide partial pressure of the cave environment; however aragonite does occur and can sometimes be interlayered with calcite (White, 2007, p.143). In a hand specimen, pure calcite is translucent or opaque white due to numerous fluid inclusions. The density and size of fluid inclusions are variable from one crystal form to another. Calcite is trigonal, with a rhombohedral or scalenohedral habit (Folk & Assereto, 1976). In most speleothems, it is present in either microcrystalline form, with the c-axis oriented roughly across the direction of growth, or as coarser columnar or palisade crystal aggregates with the c-axes oriented in the direction of growth (Folk & Assereto, 1976).

Calcite crystals can have many forms, from tabular or prismatic crystals to microcrystalline compositions. Common `length-fast´ calcite forms large clear columnar crystals on pre-existing calcite surfaces, whereas `length-slow´ calcite forms many small and narrow crystals, resembling bundles of fibers or `coconut meat´, which typically appears immediately after hiatuses in crystallization (Folk & Assereto, 1976). Variations in calcite crystal fabrics along the major growth axis of speleothems are climate related, generally associated with precipitation and evaporation (Lauritzen & Lundberg, 1999). Temperature does not seem to have an important role on the formation of different crystallographic textures in speleothems

(columnar, microcrystalline, dendritic, etc.): Lauritzen (1996) reported columnar calcite crystals forming in Norwegian caves at temperatures nearing 2°C. Rather the textures of calcite crystals in speleothems are governed by variations in drip rates and departures from equilibrium, or supersaturation levels of seepage waters (Frisia *et al.*, 2000); therefore changes in the crystal morphology have the potential to provide a record of changes in water availability (Fairchild & McMillan, 2007; Frisia *et al.*, 2000, Genty, 1992). Most speleothems grow in an intermediate range of supersaturations, or near-equilibrium conditions (White, 2007; p.142), where deviance from equilibrium growth (high supersaturations) may influence both the form and chemical properties (i.e. isotopic fractionation) of crystals (Kim & O'Neil, 1997). Columnar and microcrystalline fabrics form in quasi-equilibrium conditions (low supersaturation), where columnar fabrics are formed by constant drip waters that lack impurities, and microcrystalline fabrics are associated with high but variable drip rates, with periodic inputs of calcite growth inhibitors (Frisia *et al.*, 2000). These fabrics are generally characteristic of wet periods. Dendritic fabrics form in disequilibrium conditions, which is the result of prolonged outgassing and extremely low and unpredictable drip rates (Frisia *et al.*, 2000), most commonly associated with dry periods.

Some speleothems are composed of sequences of hard and soft calcite. Soft, high-porosity calcite may be produced from evaporative conditions near cave entrances or seasonally dry caves, and are often referred to as 'length-slow' calcite, often found to form following a major halt in deposition (Folk & Assereto, 1976). Most hard calcite is precipitated by the slow exsolution of CO_2 from solution by the enlargement and coalescence of crystallites deposited as syntaxial overgrowths on previously deposited crystals (Kendall & Broughton, 1978). These 'length-fast' calcite crystals are prominent in the humid interiors of caves, and form clear columnar crystals, which may be parallel or radiating slightly (Folk & Assereto, 1976). Spaces left between growing columns are sealed off by later deposition and constitute inclusions, normally filled with fluid (Ford & Williams, 1989, p.331). Variation in the abundance and scale of inclusions and/or organic content creates parallel growth layers, distinguishable by eye, and reflect variation in rates of deposition. Temporary cessations or hiatuses in deposition can be due to drying, periods of dissolving at the growth front, or by deposition of foreign particulates, such as dust, mud or organic grains (Ford & Williams, 1989, p.332). Syntaxial crystal growth may extend through such breaks, or new generations of crystals may form upon them with greater or lesser bonding (Ford & Williams, 1989, p.332).

1.3.2. Colour, form and rates of growth

Strong color banding (yellow, brown, red-brown) that is commonly observed in speleothems is due primarily to the incorporation of organic compounds from soil waters above the cave (Van Beynen *et al.,* 2001), Metals such as iron (red), copper (blue), and nickel (bright green) also provide color but rarely in visible concentrations (White, 2007, p.162). Annual banding, consisting of alternating light and dark lamina, can reflect seasonality in calcite deposition. Light bands are inclusion rich and generally deposited during the time of year when rainfall is more abundant, resulting in high leaf litter production and a surge of fulvic acids in the soil, which are lighter in colour (White, 2007, p.162). The darker inclusion-poor bands originate from dryer seasons, resulting from the extraction of darker humic acids from the soil (White, 2007, p.163). These alternating light and dark laminae couplets produce a highly resolved record of the environmental and climatic conditions during the time of deposition. Microscopic fluorescent banding in cave calcites is caused by the excitation of these humic and fulvic acids by an ultraviolet source, and has been used as tool for identifying annual laminations (Shopov, 2004); this is especially useful for samples that do not show visible laminations.

Speleothems come in a variety of forms; however, stalagmites and flowstones are most valued for paleoclimatic studies because of their simple geometry and potential for high resolution stratigraphy (White, 2007, p.139). Flowstones form by seepage flow on the walls and floors of caves, and accrete in layers roughly parallel to the host surface from seepage flow. The thickness of the flowstone can vary greatly from one place to another because of variations in flow of water down walls or across the cave floor (White, 2007, p.139). Normal growth rates for cold climate flowstones are similar to those observed in stalagmites, centering around ~1 μm/yr, where accretion can range upwards of several hundred μm/yr in temperate and tropical regions (Ford & Williams, 1989, p. 345; White, 2007, p.149). Not all speleothems however are represented by a continuous record of deposition; growth hiatuses can create discontinuities in the depositional record caused by drought, cold or change in groundwater routing (Frappier, 2007). Growth layering and hiatuses achieve their maximum development in flowstones (Ford & Williams, 1989, p.336), which can be in response to climatic changes or flow geometry.

1.4. Geochemistry

1.4.1. Stable isotope studies: $\delta^{18}O$ and $\delta^{13}C$

Oxygen has three naturally occurring isotopes, ^{16}O, ^{17}O and ^{18}O, with over 99% of the oxygen on earth belonging to ^{16}O (Harmon *et al.*, 2007, p.201). The isotopic signal of oxygen in speleothems is measured by the ratio of $^{18}O/^{16}O$ in water and calcite species; however the interpretation of these stable isotopes in speleothems is far from straightforward as many variables can be involved during the fractionation process. Variation in speleothem $\delta^{18}O$ values are the result of a complex interchange of environmental controls and processes in the ocean, atmosphere, soil column, epikarst and cave environment (illustrated in *Figure 1.2.*; Lachniet, 2009). In order to be able to properly interpret variations in speleothem $\delta^{18}O$, it is essential to have an understanding of the processes that control equilibrium and kinetic fractionation of $\delta^{18}O$ in water and carbonates. Fractionation is the process whereby one isotope is preferentially taken up over the other during a phase change, and typically expressed in δ notation in parts per mille (‰) relative to VPDB, (Vienna Pee Bee Belemnite), a calcite fossil from a limestone formation (Sharp, 2007, p.19). $\delta^{18}O$ values of precipitated carbonates are more enriched than their dripwater counterparts ($\delta^{18}O_{water}$ is referenced to VSMOW, or *Standard Mean Ocean Water*), hence $\delta^{18}O$ variations are referenced to the VPDB scale. Under equilibrium conditions, $\delta^{18}O$ fractionation for a given parcel of atmospheric moisture is controlled by the Rayleigh fractionation, a process of condensation and removal of precipitation (Fairchild *et al.*, 2006). Precipitation is isotopically heavier than the residual vapour, producing an effect of progressively larger fractionations, or more depleted $\delta^{18}O$ values from continued rainfall (McDermott, 2004). The rain-out effect relates to more depleted isotopic values further from the precipitation source, and has well-known correlations to latitude, altitude and continentality (Fairchild *et al.*, 2006). Changes in $\delta^{18}O$ values of the water vapour in the atmosphere are controlled primarily by temperature and relative humidity, whereas variability in the soil and epikarst zones are dominated by evaporation, and groundwater mixing (Lachniet, 2009). Varying moisture source histories can play a role in controlling isotopic composition, and most geographical locations display seasonal variations in the isotopic composition of precipitation;

however this signal is generally lost by soil and overburden filtering effects (McDermott, 2004). Over glacial-interglacial timescales, the $\delta^{18}O$ signature is dominated by changes in temperature and ocean/atmosphere circulation; however, at annual/biennial resolution sampling, and within interglacial periods, the magnitude of change is smaller, and variability in speleothem $\delta^{18}O$ may be influenced more by the processes in the soil, karst groundwater and cave, which can introduce uncertainty into the climatic interpretation of speleothem $\delta^{18}O$ records (Baker & Bradley, 2009). $\delta^{18}O$ values in calcite speleothems are typically found to range between 0‰ and -20‰ VPDB (Lachniet, 2009), where the more depleted the heavier ^{18}O is with respect to ^{16}O is generally interpreted as a reflection of colder conditions.

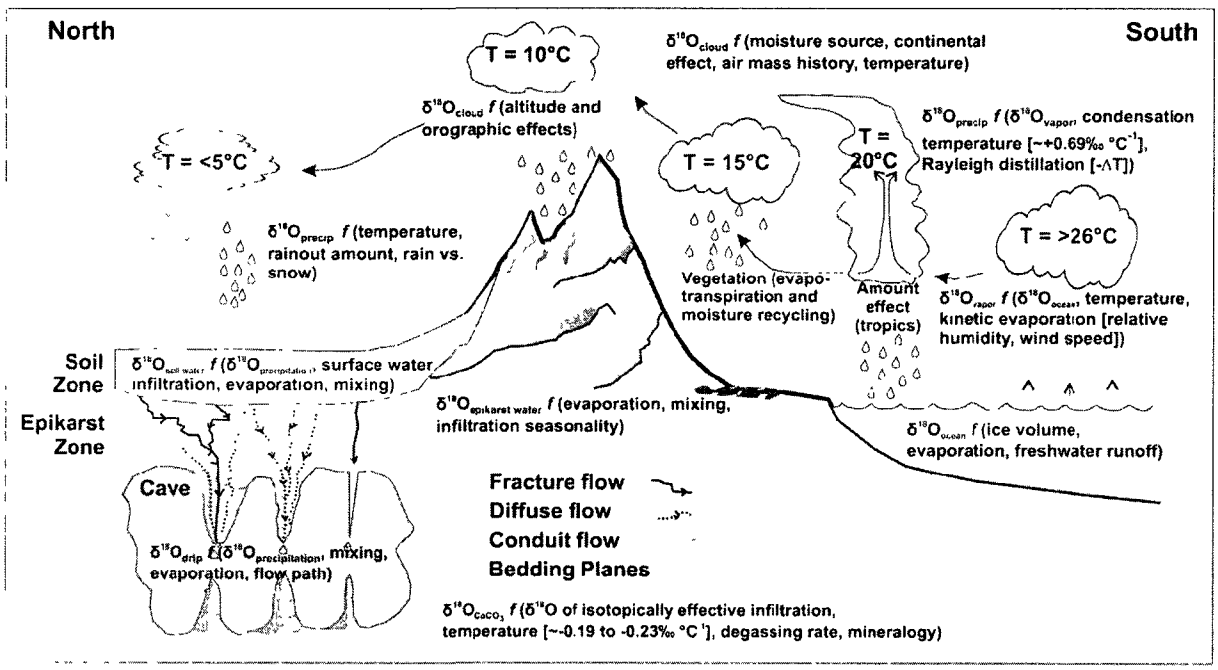

Figure 1.2. Conceptual diagram illustrating the primary controls on variations in speleothem $\delta^{18}O$ values (Lachniet, 2009).

The carbon isotopic signal in speleothem calcite arises from the $^{13}C/^{12}C$ ratio of dissolved inorganic carbon (DIC) in the dripwater, and is derived from processes occurring within the epikarst between biogenic and atmospheric CO_2, water, and the limestone bedrock (Harmon *et*

al., 2007, p.217). $\delta^{13}C$ values are also reported in δ notation in parts per mil (‰) relative to VPDB, and are found to have values ranging between -10 and +1.5 ‰ (Harmon *et al.*, 2007, p.218). Surface vegetation (C3/C4 photosynthetic pathways) and soil organic productivity will govern the amount of biogenic CO_2 available for dissolution; therefore changes in $\delta^{13}C$ of speleothem calcite will generally reflect changes in the level of organic activity in the soil column above the cave, and will respond accordingly to long-term changes in climate (McDermott, 2004). In addition, the specific photosynthetic pathway has an effect, where plants utilizing C4 pathways, typical of warm and arid environments, will yield CO_2 with higher $\delta^{13}C$ values than C3 plants which dominate in cool and moist climates (Harmon *et al.*, 2007, p.221, Hopley *et al.*, 2007). $\delta^{13}C$ ranges from -6‰ to +2‰ for C_4 vegetation, and from -14‰ to -6‰ for C_3 vegetation, therefore the mix of C_3 and C_4 vegetation varying with climate can be reflected in carbon isotope ratios found in speleothems (McDermott, 2004). However, many processes occurring within the soil, epikarst and cave zones may shift isotopic $\delta^{13}C$ values (i.e. evaporation, changes in groundwater routing, high seepage water flow, CO_2 loss by degassing in the epikarst, etc.), similar to the effects discussed for oxygen isotopes (McDermott, 2004).

Interpretation of $\delta^{13}C$ records for speleothems may present some ambiguity, which is why less attention has been paid to the stable carbon isotopes in speleothems. It is generally observed that cooler or dryer climates are associated with higher $\delta^{13}C$ values at sites where biogenic activity is the dominant control as changes in temperature have a relatively small effect on the fractionation between HCO_3 and calcite (Harmon *et al.*, 2007, p.219). However, transitions between C_3 and C_4 plants, usually associated with warmer and dryer conditions, may also correspond to higher $\delta^{13}C$ values (McDermott, 2004), adding ambiguity into the interpretation of $\delta^{13}C$ variations from speleothem records.

Advances in mass spectrometry have improved scientists' capability to reconstruct past climates at very high resolutions. Stable isotopes in speleothems have most commonly analyzed from microgram-sized powdered samples, where three main sampling protocol factors are generally considered in order to achieve higher resolution subsampling: (1) the diameter of the drill bit (typically 0.1 to 1 mm in diameter) and its effect on time averaging for each powdered sample; (2) the sampling interval or resolution; and (3) the nature of subsampling, either by spot sampling or micromilling of swaths which removes contiguous sections (Lachniet, 2009). Sampling by laser ablation has attained very high resolutions (>250 μm), although isotopic

fractionation associated with surface irregularities may be a consequence of this technique, leading to incorrect ^{18}O values (Fairchild *et al.*, 2006); micromilled samples do not experience this problem. Further enhancements on spot sampling resolution are obtainable with ion microprobe analysis, which may be as precise as 20 μm in spot size (Spotl & Mattey, 2006). These refinements on sampling resolution have resulted in an explosion of seasonal-scale speleothems studies (Kolodny *et al.*, 2003; Treble *et al.*, 2005; Baldini *et al.*, 2008; Mattey, *et al.*, 2008). One problem associated with this scale of sampling includes aliasing, or the undersampling of a periodic signal, may yield false trends and result in an underestimation of the true variability of the climate signal (Mattey *et al.*, 2008) however this problem may be diminished by subsampling with a drill bit smaller than the annual growth rate (Lachniet, 2009).

In terms of intercrystalline differences of $\delta^{13}C$ and $\delta^{18}O$ in speleothems, variations in the isotopic composition of calcite remain unclear. Various studies conducted by Dickson (1991, 1995 & 1997) have shown that natural calcite crystals can exhibit inconsistent isotopic values between synchronous, symmetrically-equivalent sectors of calcite, with variations up to 1‰, where $\delta^{13}C$ is twice as much affected as $\delta^{18}O$. Conversely, these intersectorial differences have been disclaimed by Klein and Lohmann, (1995). It is generally accepted however, that isotopic composition should be homogeneous among different crystallographic fabric types (Reeder *et al* , 1997), although studies have yet to explore this hypothesis.

1.4.2. Equilibrium vs. non-equilibrium deposition

In order to be able to interpret paleoclimate data from speleothems, the isotopes in the calcite crystals must be deposited in thermodynamic equilibrium with their parent dripwaters at slow degassing rates, in the humid interiors of caves where no evaporation is occurring (Hendy, 1971), meaning that the distribution of light and heavy isotopes between the aqueous and solid phase is only a function of temperature (Laurizten & Lundberg, 1999). Kinetic fractionations represent disequilibrium conditions that result in pronounced variations in observed $\delta^{18}O$ & $\delta^{13}C$ values, where the calcite may not be in isotopic equilibrium with their dripwaters, consequently obscuring the original climatic signal (Lachniet, 2009). Rapid crystallization, degassing in the epikarst and evaporation in the cave are common examples of such disequilibrium conditions (Fairchild *et al.*, 2006). In cold climate caves, the freezing of natural calcite-saturated waters and rapid calcite deposition can result in kinetic fractionations of $\delta^{18}O$ (Clark & Lauriol, 1992).

Fornaca *et al.* (1968), Fantidis & Ehhalt (1970) and Hendy (1971) were pioneers in acknowledging disequilibrium deposition in speleothems, where the coupled effect of evaporation and degassing produces distinctive trends with co-variation of $\delta^{18}O$ & $\delta^{13}C$. The 'Hendy Test' is commonly used to check for equilibrium deposition in speleothem, verified by an absence of covariance of these isotopes along a single lamina based on the premise that kinetic effects would lead to progressive enrichment in these isotopes as dripwaters moved over a stalagmite surface from the point of impact of the drip. Under equilibrium conditions, $\delta^{13}C$ will become enriched as a drip moves from the apex to the sides of the stalagmite due to a limited amount of bicarbonate, whereas $\delta^{18}O$ should not vary due to the relatively large amount of water available (Laurizten & Lundberg, 1999). If evaporation has occurred, significant amounts of water will be lost along the same trajectory so that both isotopes ($\delta^{18}O$ & $\delta^{13}C$) become enriched simultaneously, owing to kinetic effects as the heavier ^{13}C and ^{18}O molecules are preferentially fractionated. Varying rates of degassing and evaporation also give rise to distinctive isotopic trends (Gonzalez & Lohmann, 1987, p.93). *Figure 1.3* illustrates these changes in stable isotopic compositions owing to degassing and evaporation for carbonate deposition. Rapid degassing results in $\delta^{13}C$ enrichment due to the preferential release of dissolved $^{12}CO_2$, resulting in non-equilibrium with atmospheric CO_2; this is followed by evaporation, which results in the relative enrichment of $\delta^{18}O$ due to the preferential release of $H_2{}^{16}O$. Evaporation is almost always accompanied by degassing; as a result, both carbon and oxygen isotope compositions may exhibit a positive linear trend when these two processes take place simultaneously (Gonzalez & Lohmann, 1987, p.92). Therefore speleothems which exhibit a co-linear relationship between $\delta^{18}O$ and $\delta^{13}C$ should be regarded with suspicion as these variations are likely attributable to kinetic isotopic fractionations, and should not be used as geochemical proxies in paleoclimatic research. However, covariance of these isotopes with increasing $\delta^{18}O$ would have some paleoclimatic inference, as it would be indicative of significant drying and more evaporative conditions in the cave at the time of deposition, hence a dryer climate.

The Hendy Test has been carried out in a number of publications, but in actuality is very difficult to execute. Sampling along a single growth layer is flawed both in theory and practice due to limited sampling precision, speleothem geometry and variability in laminae thickness. Dorale & Liu (2009) argue that several other limitations exist within the 'Hendy Test' criteria in judging the paleoclimatic suitability of speleothems. One discrepancy is that it is possible that

isotopic equilibrium may occur in the center of the speleothem at the same time kinetic fractionations occur at the flanks. In addition, the criterion that there is no relationship between $\delta^{18}O$ and $\delta^{13}C$ along a growth band is based on the assumption that speleothem $\delta^{13}C$ values are not linked to climate, which is not necessarily true. Climate is directly related to soil bio-productivity and vegetation type, therefore in some cases, a coupling of $\delta^{13}C$ and $\delta^{18}O$ values may not related to kinetic isotope effects, but instead an indication of climatic change. Furthermore, the Hendy Test depends on the flow path of seepages waters, therefore speleothem geometry remains an important consideration. In place of the 'Hendy Test', Dorale & Liu (2009) advocate the need for replication of similar isotopic profiles between two or more stalagmites; however this too presents limitations, predominantly with respect to cost restrictions and cave conservation.

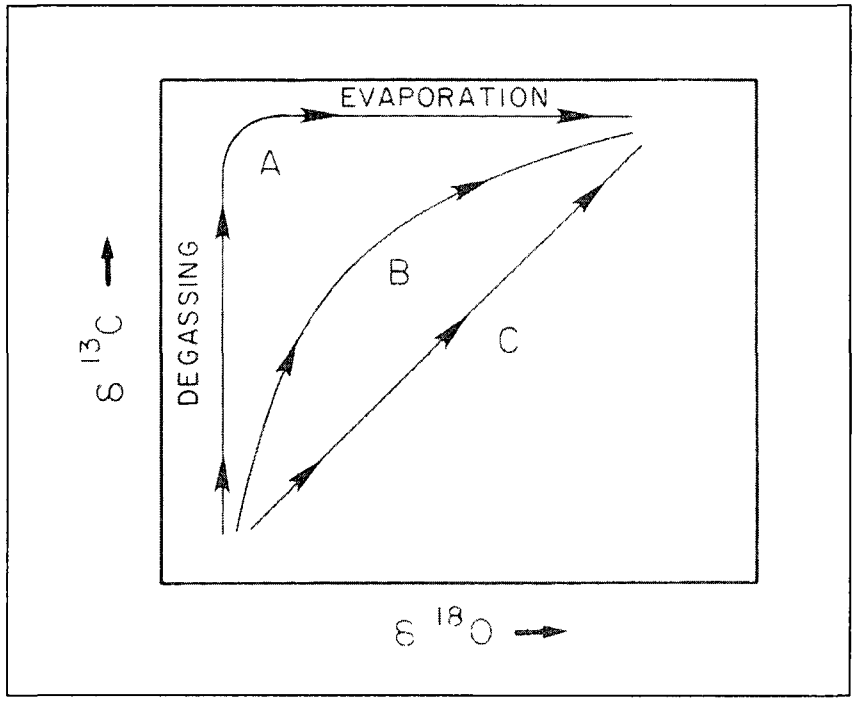

Figure 1.3. Changes in stable isotopic compositions due to degassing and evaporation during carbonate deposition (Gonzalez & Lohmann, 1987, p.94). Arrows along the X and Y axis indicate relative enrichment. If degassing is followed by evaporation, oxygen isotopic compositions are then enriched at fixed carbon values (line A). Simultaneous evaporation and degassing results in slopes determined by the relative importance of these two processes (lines B & C).

1.4.3. Trace element studies

Minor (100 ppm – 10 000 ppm) and trace (100 ppm to 10 ppb) amounts of exotic elements carried by dripwaters or aerosols may be incorporated into speleothems (Fairchild & Treble, 2009); these constituents can serve as important archives in paleoenvironmental research (Smith *et al.*, 2009; Fairchild *et al.*, 2007; Cruz *et al.*, 2007; Johnson *et al.*, 2006; Roberts *et al.*, 1998). Insoluble and organic matter usually deposits on the intercrystalline boundaries, where metal ions, such as Mg^{+}, may substitute into the calcite crystal lattice in an amount that may relate to temperature at the time of deposition (Lauritzen & Lundberg, 1999). An increasing number of studies have focused on the paleoclimatic and paleoenvironmental significance of the colour of speleothems and its relation to the variations in organic, chemical and isotopic composition (Ayalon *et al.*, 1999; Blyth *et al.*, 2008; McGarry and Baker, 2000; Perrette *et al.*, 2005; Van Beynen *et al.*, 2001; Fairchild & Treble, 2009). Although organic content is believed to be the main cause of colour variation in speleothems, variations in trace elements, predominantly iron oxides and hydroxides, were initially believed be the source of pigmentation (White, 2007, p.162).

Variations in trace elemental concentrations, isotope composition, and organic compounds also have paleoclimatic significance as they reflect changes in hydrochemical and weathering processes in the epikarst zone above the cave as well as other external processes (Van Beynen, 2007). These elements can either become incorporated into the crystal lattice, or present within the detrital fractions between the crystals or in the fluid inclusions (White, 2007, p.159). Trace element variations in speleothems have a high potential to reflect multiple aspects of seasonality and other climatic events; these variations are likely due to the same processes that causes variations in layer thickness and crystal morphology related to growth kinetics (Frisia *et al.*, 2000; Cruz *et al.*, 2007), and have been known to correlate with rainfall and temperature variations on the surface (White, 2007, p.159). Sympathetic variations in U, Mg, Sr, Na, Ba, F, and P have been observed within annual laminae (Fairchild *et al.*, 2001; Treble *et al.*, 2003). The ratios of Mg and Sr to Ca have been linked to seasonal temperature changes which are related to the residence time of water in the unsaturated zone (Roberts *et al.*, 1998). In theory, Mg/Ca and Sr/Ca are higher during drier conditions or low flow periods due to the selective leaching of Mg and Sr relative to Ca from soil (Huang *et al.*, 2001; Fairchild *et al.*, 2000), and are used to

interpret relative variations in rainfall amount (Cruz *et al.*, 2007). Higher Mg/Ca ratios are also found in drip waters or cave pools that have undergone significant degrees of evaporation or prior calcite deposition, and when coinciding with increases in $\delta^{13}C$, may be indicative of diagenically altered speleothem due to the high $\delta^{13}C$ value of the carbonate host rocks and their reservoir of Sr^{2+} and Mg^{2+} ions (Hopley *et al.*, 2009).

Many high resolution trace elemental analysis studies have been conducted on speleothems, employing a number of different methods, such as the electron microprobe, and micro x-ray fluorescence spectrometry (Fairchild *et al.*, 2006), as well as those produced from individually drilled powdered samples, including atomic absorption spectrometry (AA), inductively-coupled mass spectrometry (ICP-MS), and inductively-coupled plasma atomic emission spectrometry (ICP-AES) (Fairchild & Treble, 2009). One of the advantages of these traditional powdered sample methods is that it allows for the simultaneous analysis of both trace elements and stable isotopes, which can enhance multi-proxy time series (Fairchild *et al.*, 2006). Most published trace elemental studies have been produced from LA-ICP-MS in particular (Hoffman *et al.*, 2009; Tipper *et al.*, 2008; Desmarchelier *et al.*, 2006) because of its high precision (ppt-ppq detection limits), and its capacity as a rapid trace elemental technique with the possibility of revealing information about isotopic constituents (Fairchild & Treble, 2009). This method however can be fairly costly, whereas ICP-AES is robust and relatively inexpensive. Solution-based analysis by ICP-MS or ICP-AES offers a high level of analytical accuracy, but required detailed attention from trained analysts to achieve reliable results (Fairchild & Treble, 2009). Na, Mg, Ca, Sr and Ba are elements that have traditionally been targeted for analysis by ICP-AES, with typical powdered sample sizes ranging from 100-5000 µg, and dilutions of around 1x to 4000x (Fairchild & Treble, 2009). Micro-analysis of laminations along the growth axis of speleothems have proved to be difficult due to the high spatial resolution of the growth layers (ranging from several micrometers up to a millimetre in some cases), and although time consuming, high resolution powdered sampling can be obtained with the use of a micromill (Fairchild *et al.*, 2006).

Technological advances in mass spectrometry have permitted analysis of smaller samples by ICP-MS which has found that trace elements can vary along single crystal faces (Paquette and Reeder, 1990), as well as variations between different calcite fabrics due to surface crystal structure and geometry (Reeder & Grams, 1987).

1.5. Dating techniques applied to ancient speleothems

The ^{238}U decay series, illustrated in *Figure 1.4*, offers many possibilities for dating cave calcites, where most speleothems can be dated using the $^{238}U/^{230}Th$ decay series. This is based on the principle that uranium is soluble and easily mobilized in karstic waters; therefore uranium may be incorporated into speleothems by infiltration waters. Thorium is insoluble and immobile in karstic ground waters, thus it can be assumed that any ^{230}Th found speleothems is the result of uranium decay (White, 2007, p.143). Therefore with the knowledge of the half-lives of these isotopes, we can obtain a measure of the time elapsed since deposition.

Many dates obtained from speleothems are clustered in the Holocene and early Quaternary period as most samples fall within the conventional 350 Ka limit of this dating technique. New advances on speleothem dating techniques by TIMS (Thermal Ionization Mass Spectrometry) and MC-ICP-MS (Multi Collector-Inductively Coupled Plasma Mass Spectrometry) push this limit to about 600 ka (J. Lundberg, 2010; personal communication).

Few specimens have dated past the Quaternary period, mainly due to the fact that preservation of ancient speleothems over time are rare, and also because a greater experimental uncertainty exists with retrieving such dates. Although this uncertainty remains, it is possible to obtain dates from ancient speleothems. $^{238}U/^{206}Pb$ dating is promising for dating speleothems of Quaternary age and older as this method has no upper limit; however it requires that speleothems have an inherently high uranium concentration (>10 ppm) and very low Pb concentrations (<10 ppb) where the initial state of U-series disequilibrium can be difficult to estimate (Richards *et al.*, 1998). In addition, and as with many other dating techniques, this method can be considerably expensive.

Radiogenic helium (He) dating, or He produced from radio-isotopes, is a developing dating method that utilizes U-series decay. These decay series feature many instances of alpha (α) decay (*Figure 1.4*), that is, the expulsion of ^{4}He nuclei (Clark & Fritz, 1997, p.241). Helium is a member of the noble gases, which are chemically stable and inert. The production of radiogenic ^{4}He in the crust is dominated by the α-decay of the ^{238}U, ^{235}U and ^{232}Th decay chains; therefore the production rate, number of ^{4}He atoms per gram of rock per year ($^{4}He\ g^{-1}\ yr^{-1}$) is directly proportional to the concentrations of these radio-elemental bi-products (Farley, 2002). The production of ^{4}He from each radio-isotope, R, is given by *Equation 5*, as outlined by Ballentine & Burnard (2002):

$$^{4}He \text{ atoms } g^{-1} yr^{-1} = X_R [R] (N_A/A_R) \times 10^{-6} (e^{\lambda t} - 1) \times yield_R \quad [4]$$

Where:

X_R = Fractional natural abundance of isotope R

N_A = Avogadro`s number (6.023×10^{23})

A_R = Molar mass of R (g)

λ = Decay constant of R (yr^{-1})

yield = Number of λ particles emitted in the complete decay chain

[R] = Concentration of R in ppm

t = Age (yr)

Given that the ^{238}U decay chain ultimately yields eight ^{4}He atoms ($\lambda_{238} = 1.55 \times 10^{10}$, $X_{238} = 0.9928$), with seven from ^{235}U ($\lambda_{235} = 9.85 \times 10^{-10}$, $X_{235} = 0.0072$), and six from ^{232}Th decay ($\lambda_{232} = 4.95 \times 10^{11}$, $X_{232} = 1.000$), and assuming the initial concentration of ^{4}He in the rock is zero, the number of ^{4}He atoms produced in one gram of rock per year becomes:

$$^{4}He \text{ atoms } g^{1} yr^{1} = (3.115 \times 10^{6} + 1.272 \times 10^{5}) [U] + 7.710 \times 10^{5} [Th] \quad [5]$$

Therefore, $$Age = He^{4} ccSTP \times [(6.023 \times 10^{23}/22414) / (He^{4} \text{ atoms } g^{-1} yr^{-1})] \quad [6]$$

This dating method has the potential to be used as a valuable tool for dating ancient speleothems; however several limitations exist. The potential for loss of He gas from the sample by diffusion can result in unreliable and unusually low ages. Furthermore, limited analytical precision and the methodological complexity of this method add to the uncertainty (Farley, 2002).

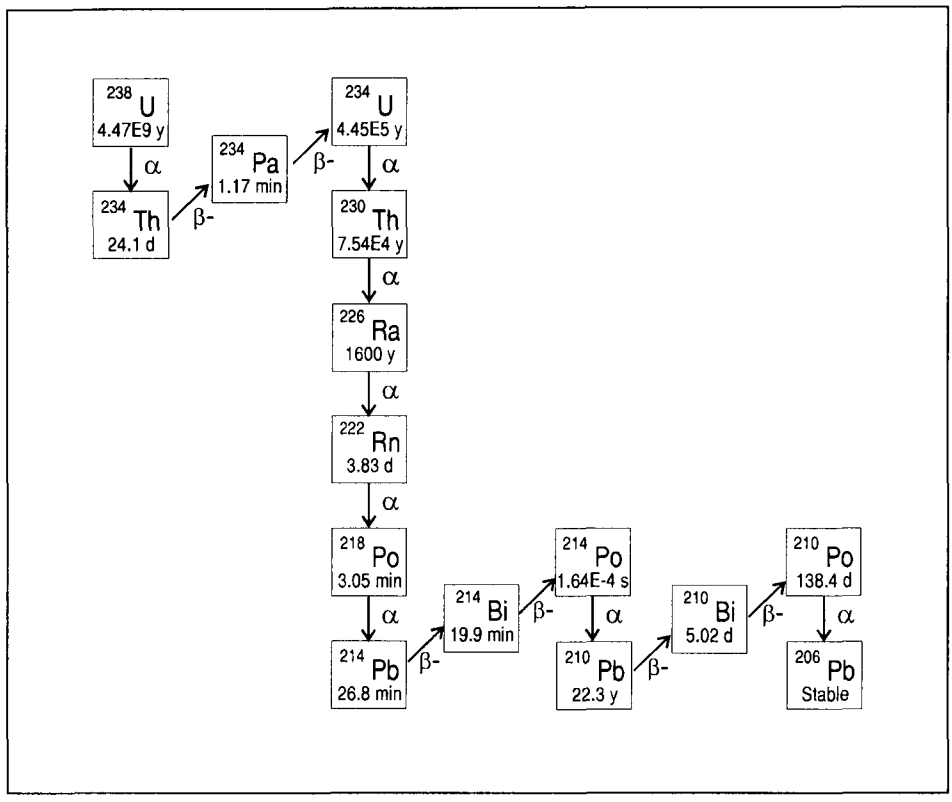

Figure 1.4. The ^{238}U decay series (Clark & Fritz, 1997, p.239).

Many speleothems contain a measureable quantity of natural remnant magnetism, either of chemical or detrital origin, therefore speleothems can provide a comprehensive record of paleomagnetism during the time of deposition (Latham *et al.*, 1988). Although magnetic reversal records may only provide a lower-resolution relative age record in comparison to higher resolution dating methods (i.e. U-series dating), they can provide useful hints about the time and length of deposition in extensive chronologies, in particular for older speleothems which fall outside the range of U-Th dating. The lengths of polarity intervals range from 0.01 Ma to several tens of millions of years (White, 2007, p.147); however the shorter-lived events (subchrons) are more apt to be captured over the timeframe speleothem deposition. The last known reversal occurred 780 ka BP, therefore the correlation of speleothem magnetostratigraphy with the known geomagnetic polarity timescale can be used to generate a fixed time reference from the sedimentary sequence of a speleothem. This can also be used in conjunction with faunal assemblages (Hopley *et al.*, 2007), volcanic ash layers, or other known geological events to further refine age estimations.

2. REGIONAL SETTING & SAMPLE DESCRIPTION

2.1. Bear Cave, Yukon Territory

The study region is situated in Fishing Branch Ni'iinlii'njik Park in the North-western Yukon Territory. Bear Cave is located in the center of this reserve (66°30'N, 139°20' W), in the Northern Ogilvie Mountain range, just south of the Arctic Circle (*Figure 2.1*). Established in 1999, access to this ecological reserve is currently restricted in order to protect nearly 7000 km^2 of habitat including a flourishing grizzly bear population, invaluable salmon runs along the Porcupine River, as well as a network of ancient limestone caves (Environment Yukon, 2010). This chapter will include a description of the geological development of the cave as well as a brief history of the regional climate and vegetation of the area. This will be follow by a general description of the BC1 flowstone.

2.1.1. Geology

Bear Cave Mountain reaches an altitude of 990 m, and sits roughly 500 m above the bed of the Fishing Branch River. The cave itself is a short remnant cave, measuring 220 m in length, and is situated on the south-facing limestone cliff, 867 m above sea level (*Figure 2.2*). It consists of three main chambers which contain an abundance of speleothems, some of which measure over 3 m in depth (Lauriol *et al.*, 1997). These mountains are composed of platformal limestone deposited sometime during the lower and middle Devonian, which include the Ogilvie & Gossage formations (Norris, 1978) that were later folded and faulted at the Cretaceous-Tertiary boundary as a part of the Laramide orogeny (*Figure 2.3*). Evidence for paleo-terraces along the Porcupine River suggests that a hydrographic network was established in the area during the early Tertiary (Duk-Rodkin & Hughes, 1994), which allowed for the development of a series of caves in these mountains, Bear Cave being the largest. The continuous incision of the Porcupine River through these mountains resulted in the isolation of the caves above the hydrographic network during the mid- to late-Tertiary, at which time it is likely that speleothem formation could have started (Lauriol *et al.*, 1997). Following major depositional hiatuses, speleothem growth would likely have continued until the establishment of permafrost in the area at the onset of the early Pleistocene glacial period (Lauriol *et al.*, 1997).

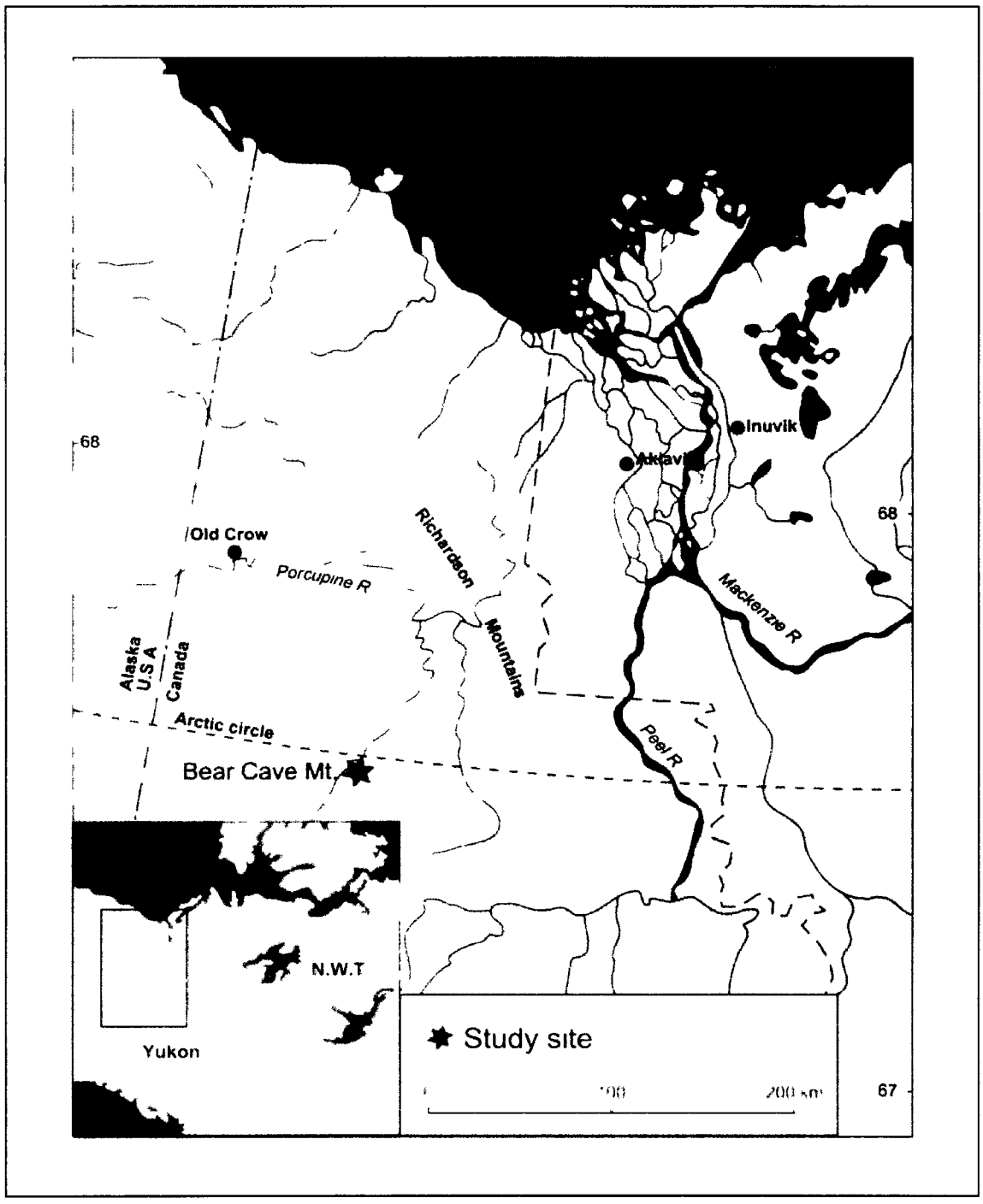

Figure 2.1. Location of Bear Cave Mountain, Yukon Territory, N 66°30', W 139°20'.

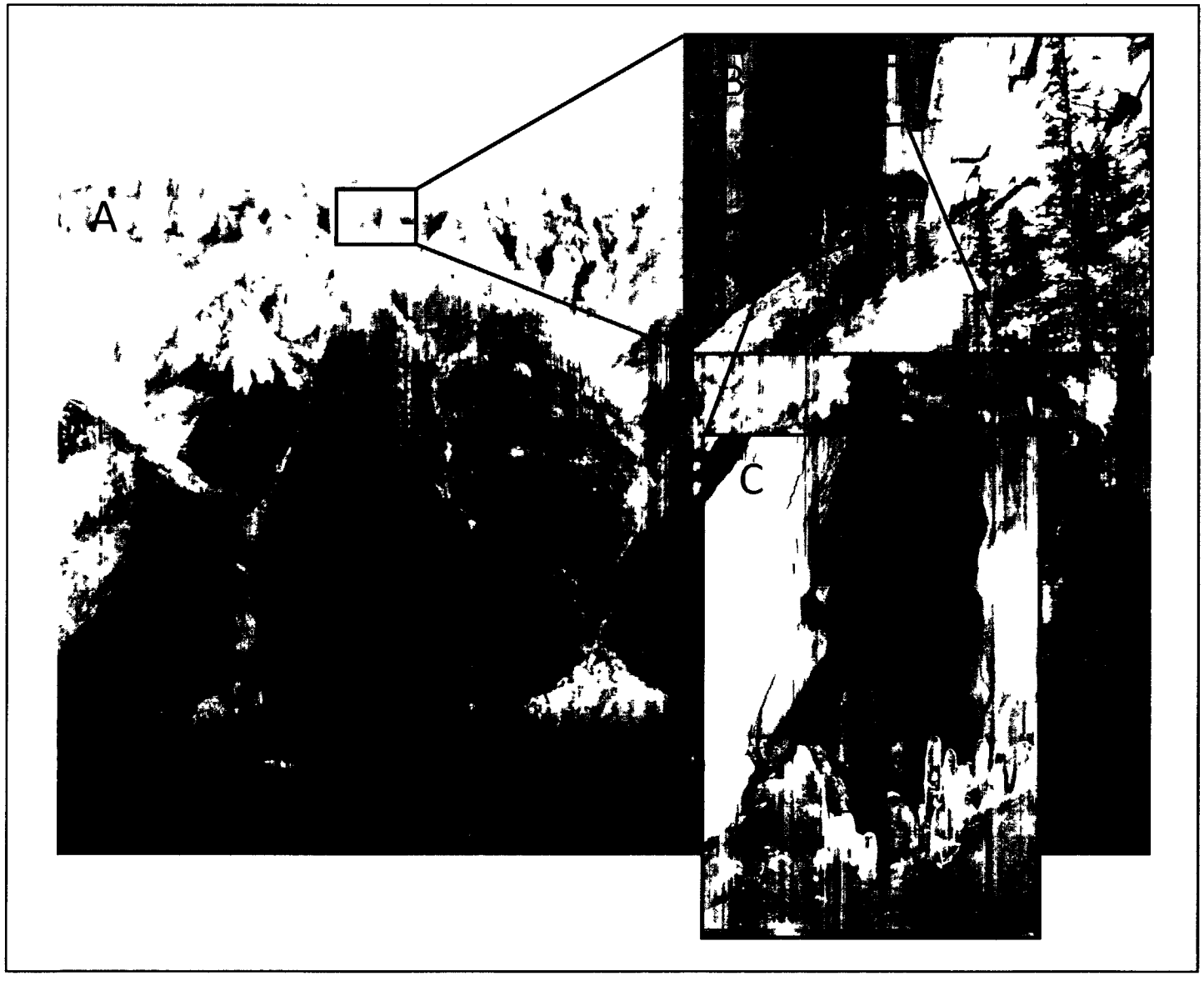

Figure 2.2. Bear Cave Mountain, Yukon Territory (N 66°30', W 139°30'), with a view of the SE face of the mountain (A), the cave entrance (B), and the cave interior (C), Photos: B.Lauriol.

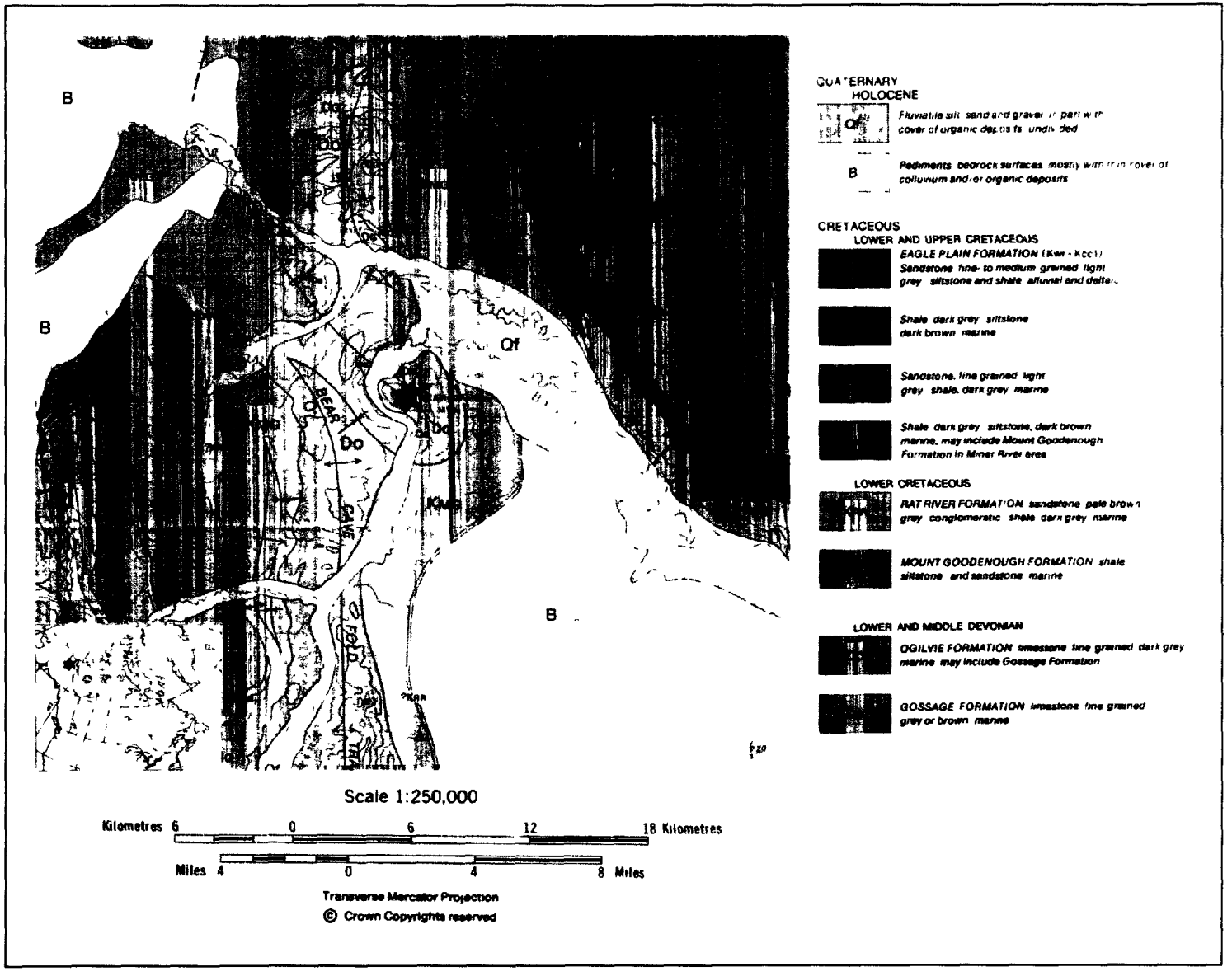

Figure 2.3. Geological map of the Porcupine River Basin, Northern Yukon Territory. Map center: N 66°30', W 139°20' (Geological survey of Canada; Norris, 1978).

Present conditions inside the cave are fairly constant with mean annual air temperatures lingering around -2°C, allowing for the preservation of ice on the cave walls (*Figure 2.2.C*), prohibiting erosive surface streams from flowing into the cave and wearing away the ancient calcite deposits.

2.1.2. Regional climate and vegetation: past and present

The landscape of the northern Yukon Territory was an especially different scene during the Tertiary in comparison to the present day. The undeveloped St-Elias mountain range in Alaska permitted the circulation of warm and humid air from the Pacific toward central Yukon. Continental positions and ocean gateways during the mid-Pliocene were essentially the same as today, however sea level was ~25 m higher than present (*Miller et al., 2010*), likely also permitting greater exchange of waters and heat from the Pacific. As a result, conditions in the northern Yukon Territory were generally warmer and wetter during this period. Mid-Pliocene CO_2 concentrations are estimated to have been similar to modern atmospheric levels, centering around ~400 ± 50 ppmv (*Miller et al., 2010*). As described by Ritchie (1987), studies on late-Eocene deposits in the Northern Yukon Territory have found that tree species typical of warm and humid subtropical environments (*Sequoia, Tilia, Ulmus, Quercus*, etc.) dominated ~48 Ma. The rise of genus such as *Picea, Alnus, Betula* and *Sphagnum* toward the end of the epoch indicates declining average annual temperatures, from roughly 20-25 °C at the beginning of the Eocene to 11-13 °C toward the end. The Oligocene saw a return to warmer temperatures (13-20°C) around the beginning of the epoch, with the appearance of species such as *Acer, Gingko*, and *Metasequoia*; however the progressive return to deciduous-dominated forests toward the end of the epoch indicates slight cooling (8-12°C). The Miocene epoch was distinguished by cooler conditions, where temperatures averaged around -5 to 12°C in the northern Yukon. The region was dominated by a mixed coniferous and deciduous forest (*Picea, Pinus, Tsuga, Abies*, and *Larix*), with the appearance of more softwood and some ericaceous shrubs (*Betula, Salix*) toward the mid-Miocene. Similar conditions prevailed into the mid-Pliocene, with the frequency of more deciduous species spread across a rich boreal forest indicating the climate was warmer than the present day. Global circulation models indicate that average annual surface air temperatures were generally warmer during the mid-Pliocene than present conditions, particularly in the

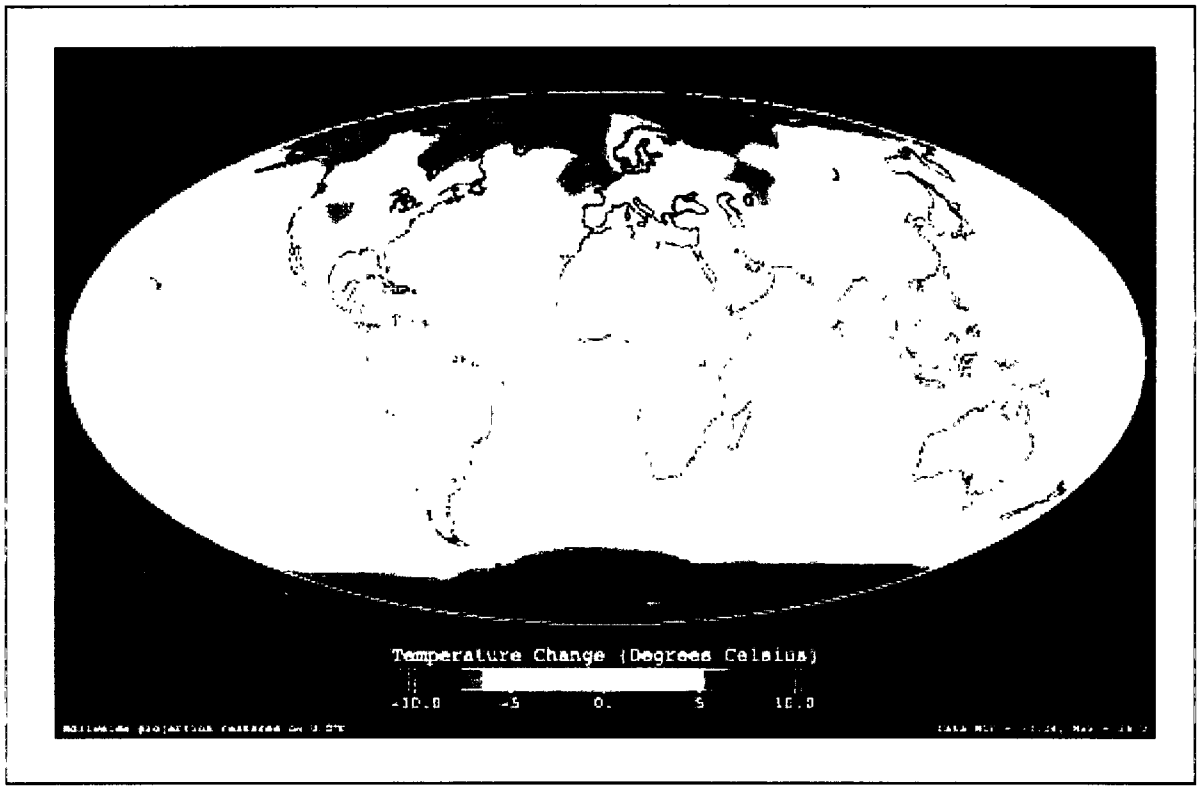

Figure 2.4. Annual average surface air temperature as simulated by the GISS GCM based on mid-Pliocene boundary conditions supplied by the USGS PRISM Project, version 2 (Dowsett, *et al.*, 1999).

Northern Yukon, where temperatures were upwards of 7-9°C warmer than today (*Figure 2.4*). The presence of iron oxides in cryoturbated paleosols in the region suggests that permafrost was absent or much deeper in the late Tertiary in comparison to modern day conditions (Tarnocai & Schweger, 1991).

The Quaternary period is characterized by the alternation of glacial and interglacial periods; however the study region, as with most of the northern Yukon Territory, remained ice-free during the Pleistocene glacial periods. As a result, permafrost was thicker during these cold glacial periods and most of the valleys and plateaus were characterized by a steppe grassland. During the warmer interglacials, permafrost extent would have diminished and thaw depths deepened in the northern Yukon, allowing for various tree species to invade the area (Hopkins *et*

al , 1982, p.33). Pollen profiles at Bluefish basin in the Northern Yukon indicate a cooling trend at the beginning of the Pleistocene, by the transition of a coniferous forest (*Pinus*, *Picea*, *Corylus*, and *Larix*) to shrub tundra from 1.6 to 0.7 Ma, as well as the presence of pseudoform ice wedges (Matthews *et al.*, 1990). Detailed information is only available for the last of the glacial-interglacial cycles, where we see warmer conditions prevail around 150 ka with the reappearance of a few trees in the pollen records (Thibodeau, 1988). Relict ice wedges and Old Crow tephra found in exposed sediments dating back ~130 ka indicates cooling likely induced by explosive volcanic activity in the Aleutian Arc - Alaska Peninsula (Ritchie, 1987, p.23). Increases in sedge and grass species in the pollen record suggest warming around 60 ka, with a return to colder temperatures again around 37 Ka, with spruce, birch and sedges dominating in the record; this suggests temperatures were likely similar, if not slightly colder than present conditions (Lichti-Federovich, 1973). According to Ritchie (1987, p.83), the end of the Pleistocene was marked again by warmer temperatures, with grassy tundra on the plateaus and the extension of treed tundra in the valleys by 14 ka. A return to cooler conditions at the beginning of the Holocene (~12 ka) is shown in the record by a decline of the grasses and shrubby tundra dominating in the valleys. Gradual warming occurred over northern Yukon from 8 to 5 ka, with increasing percentages of *Betula*, *Salix*, *Picea* and *Alnus*.

At present, the region possesses a continental sub-Arctic type climatic regime, with long cold winters and short mild summers. Mean annual air temperatures recorded at the nearest meteorological station at Old Crow (250 m a.s.l.), fall around -9.0 ± 3.0°C (January T°C - 31.1°C; July T°C 14.6°C; Environment Canada, 2004). Total annual precipitation is relatively low, totalling 265 mm, half of which falls as snow (Environment Canada, 2004). Cyclonic activities are responsible for some of the precipitation; however rainfall during the summer months frequently results from local convection (Wahl et al., 1987). These climatic conditions are conducive to the maintenance of continuous permafrost in the area (Heginbottom *et al.*, 1995), and to the development of primitive brunisols and cryosols (Tarnocai & Schweger, 1991). The modern region is dominated by sub-Arctic tundra vegetation, dominated by black spruce (*Picea mariana*) in the valleys and Dryas-rich tundra on plateaus (Ritchie, 1987, p.116).

2.2. BC1 flowstone

A 68 cm-thick flowstone, labelled BC1, was recovered from the first main chamber of Bear Cave in 1987. Originally formed in one of the inner chambers, continuous incision and erosion of the mountains brought it closer to the present day cave entrance. Stratigraphically, this formation is likely one of the oldest calcite in the cave (Lauriol *et al.* 1997). The flowstone was originally deposited against the cave wall and on a conglomerate of rounded sandstone, quartz, quartzite, chert and calcite gravels in a fissure approximately 50 cm wide (*Figure 2.5.A*). Deposition would have continued until the passage was filled. Both the conglomerate and the flowstone were then dissected by a cave stream that enlarged the passage, leaving the deposit hanging, until it eventually fell to the cave floor where it was discovered resting in four blocks (*Figure 2.5.B*). After the stream dried up, a new phase of ancient speleothem deposition followed in other parts of the cave (Lauriol *et al.* 1997).

Figure 2.6 presents a high-resolution scan of the flowstone in cross section. BC1 is segmented in 4 blocks, labelled BC1-1 through BC1-4 from the base to the top of the sample. Each block is separated by a discontinuity representing a major depositional hiatus. This flowstone has well defined crystal structures with distinct colour variations, which makes it an ideal specimen for crystallographic analysis. It consists of two main types of crystal fabrics: a harder, dense, dark-brown translucent fabric, and a softer, more porous, lightly-coloured opaque calcite.

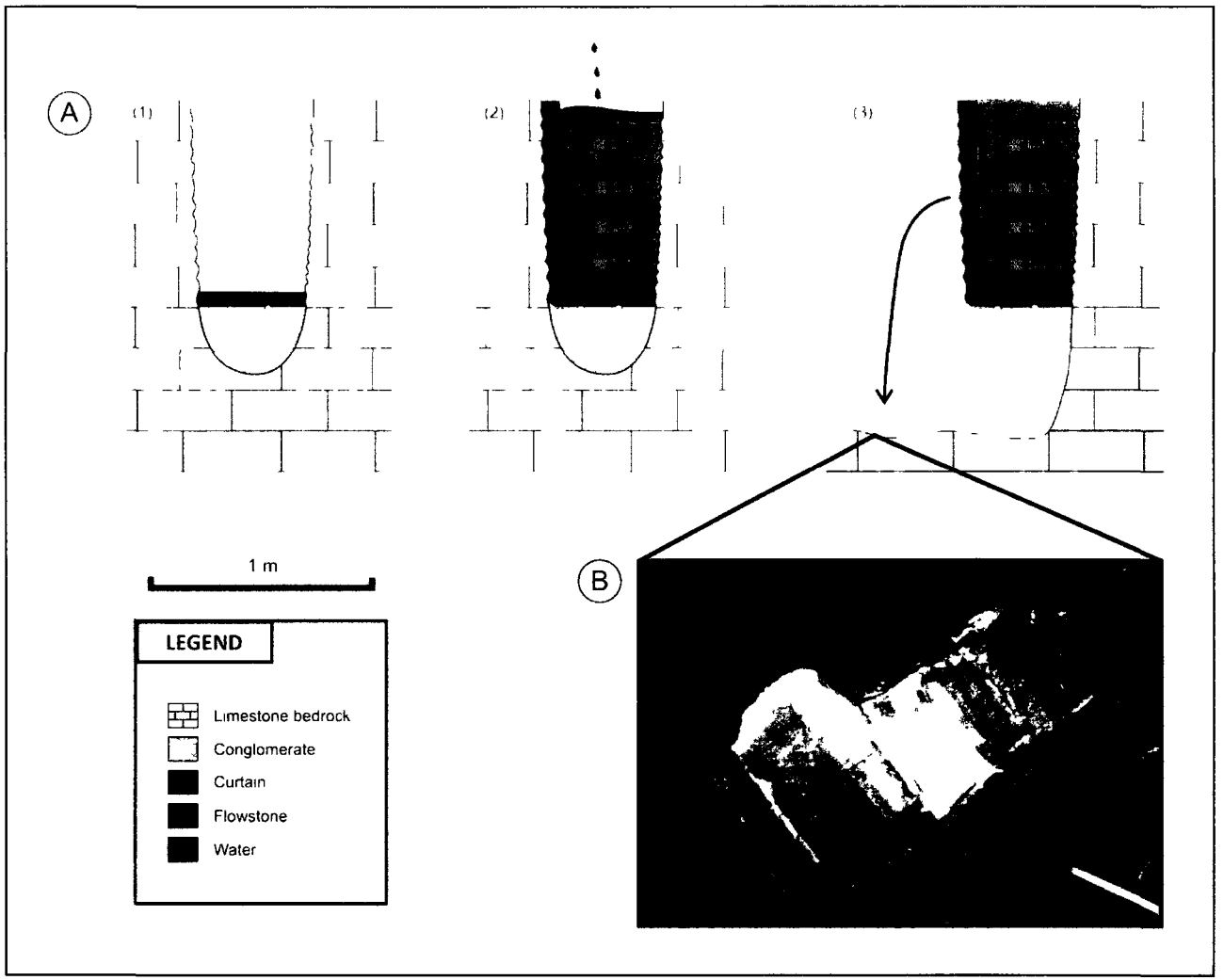

Figure 2.5. (A) Development of the BC1 flowstone: (1) Passage enlargement and deposition of rounded sandstone, quartz, quartzite, chert and calcite gravels on the cave floor; (2) Establishment of a curtain speleothem along the wall and floor of the cave followed by the deposition of BC1-1, BC1-2, BC1-3 and BC1-4; (3) Continued erosion of the cave and collapse of BC1 on the cave floor. (B) BC1 flowstone as discovered on the cave floor.

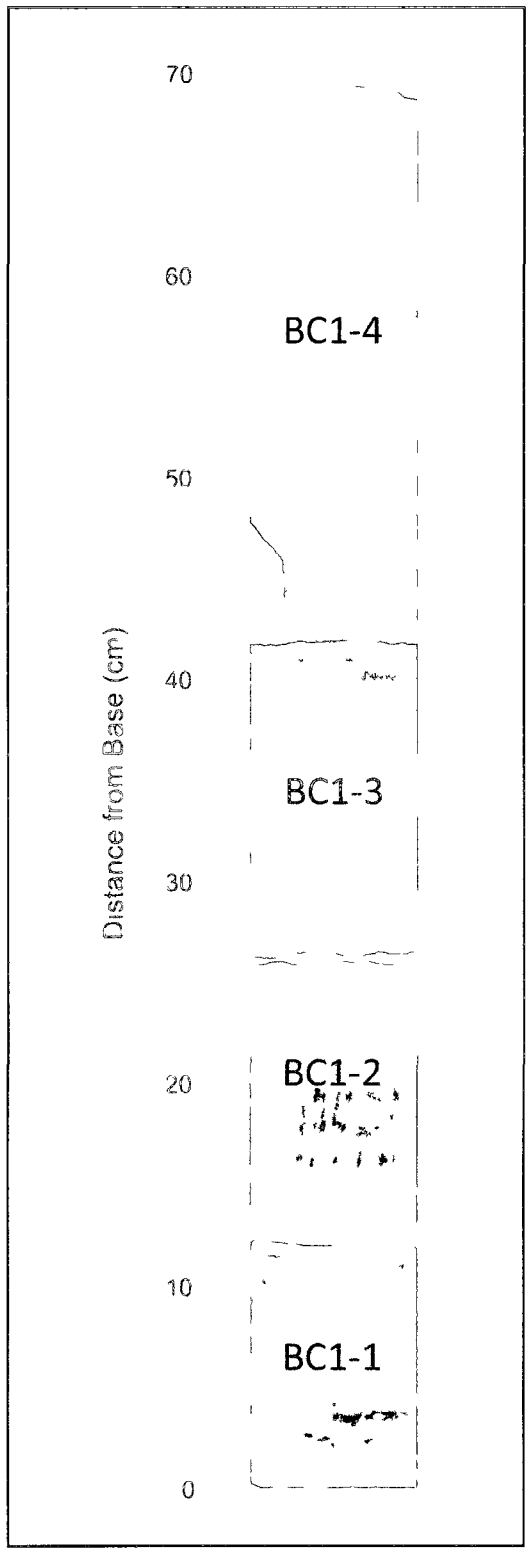

Figure 2.6. High resolution cross-sectional scans of the BC1 flowstone. Individual blocks are labelled BC1-1 through BC1-4 from the base to the top of the flowstone.

3. METHODOLOGY

Due to the exploratory nature of this study, a multi-proxy approach was adopted in order to explore the suitability of the BC1 flowstone for paleoclimate studies. This project combines new research (crystallography, epi-fluorescence, trace elements, and additional sampling of stable isotopes) with previously collected data relevant to this study (stable isotopes and paleomagnetism). These data was used in conjunction with new and old dating techniques as outlined in the subsections below.

3.1. Petrography

A comprehensive petrographic study was carried out along the growth axis of BC1 in the fall of 2008, including a detailed crystallographic study documenting the changes in crystal fabric, scanning electron micrograph (SEM) imagery to view the crystal boundaries in greater detail, and epi-fluorescent spectroscopy to study any invisible laminations caused by varying intensities (concentration and composition) of organic material. Crystal fabrics were defined using the terminology of Folk & Assereto (1976), Kendall & Broughton (1978), Frisia *et al.* (2000), Railsback (2000) and Couchoud (2007).

3.1.1. Crystallographic study

The changes in crystal morphology along the growth axis of the BC1 flowstone were documented using petrographic thin sections. When cutting the sample, attempts were made to avoid transitions in crystal fabrics when making thin sections as 1-2 mm may have been lost due to saw width. Due to the large nature of the crystals, crossed-polar images of the crystals in thin section were taken at 1.25x (total magnification) with an Olympus BX41 microscope and Olympus U-CMAD3 camera. The entire profile of BC1 was documented by acquiring and stitching together sequential petrographic images of each thin section running parallel to the growth axis of the flowstone. Petrographic transects of the crystals in thin section are presented in *Appendix I.* Several adjacent transects from each thin section were obtained in order to ensure homogeneity and representativeness. The images of the crystals were sampled at a resolution of 1.5 mm using *Corel Draw*© in order to document the changes in crystal morphology along the BC1 profile. Sampling was conducted in close proximity to the same profile used for geochemical analysis.

3.1.2. Scanning Electron Micrography

Scanning electron micrograph (SEM) images of selected individual crystals were obtained at the Scanning Electron Microscope Laboratory in the Department of Earth and Atmospheric Sciences at L'Université du Québec à Montréal (UQAM) using a HITACHI S-4300SE/N (VP-SEM). In addition to the SEM images, select trace elemental concentrations were obtained from various organic and inorganic substances present on the intercrystalline boundaries. Crystal samples were extracted from the flowstone using a rock saw and hammer, and samples were cleaned in dilute 0.10 M HCl for 10 minutes followed by an ultrasonic bath in order to decontaminate the surface and expose the crystal boundaries.

3.2. Geochemistry

The geochemistry of BC1 was investigated in two studies. The first includes a comprehensive stable isotope ($\delta^{13}C$ & $\delta^{18}O$) record spanning the entire length of the flowstone, combining new and old data. A near-continuous record was obtained by D. Lacelle in 2006 (Lacelle, 2007) however some sections of the flowstone remained unsampled; additional sampling was carried out more recently in February of 2009, which completes the record. An additional study involves higher-resolution analysis of stable isotopes ($\delta^{13}C$ & $\delta^{18}O$) and select trace elements within small transects of two distinctly different microfabrics in order to investigate any differences between the two. This study was also completed in the winter of 2009.

3.2.1. Stable isotope profile ($\delta^{13}C$ & $\delta^{18}O$)

$\delta^{13}C$ and $\delta^{18}O$ were sampled along the growth axis of BC1 at 1.5 to 10 mm intervals; only blocks 2 and 3 were sampled at a higher resolution due to cost restrictions. Approximately 0.5 µg powdered samples were obtained on thick sections using a Merchantek EO Micromill and a #4 (400 µm in diameter) tungsten carbide drill bit where drill pass depths did not exceed 500µm. This traditional method of sample drilling allows for the same powdered material to be analyzed for both stable C-O isotopes and trace elements (see section *3.5*). Samples were weighed into glass exetainers, where 0.1mL of 100% H_3PO_4 was subsequently added to the side, then capped and He-flushed while horizontal. The powdered samples were allowed to react with the

phosphoric acid at 25°C for 24 hrs, and the $^{18}O/^{16}O$ and $^{13}C/^{12}C$ ratios of the flowstone were determined from CO_2 gas produced from this reaction. The resultant CO_2 gas was analyzed in continuous flow using a Gas Bench II interfaced with a Finnigan Mat Delta$^+$ XP isotope mass spectrometer at the G.G. Hatch Isotope Laboratory, University of Ottawa. Stable isotope data for C and O are expressed in δ-notation, where δ represents the parts per thousand difference of $^{13}C/^{12}C$ and $^{18}O/^{16}O$ in a sample with respect to the Vienna Pee-Dee Belemnite standard (VPDB). Analytical precision (2σ) is +/- 0.1‰ for both isotopes.

3.2.2. High-resolution geochemistry (trace elements & stable isotopes)

Two transects running parallel to the growth axis of BC1-3 (*Figure 3.1*) were selected for analysis as it was found to display clear laminations and distinct crystallographic variations. *Transect A* consists of 12 laminations isolated within the harder/darker calcite, 105-112 mm from the base of BC1-3, and *Transect B* includes 10 laminations within the lighter/softer calcite, 65-71 mm from the base of BC1-3. More specifically, *Transect A* consists of a tightly-packed *Elongate Columnar* microfabric, whereas *Transect B* consists of a more porous fabric of loosely-packed columnar crystals with a branching fabric in-filling the intercrystalline boundaries (*Columnar-with-Branched*), as identified from the crystallographic study. The latter fabric was chosen as it is suspected to be the result of recrystallization or kinetic effects (observed from isotopic variations), whereas the former is believed to be representative of initial deposition (see *Section 4.2.2*).

Trace elemental concentrations of each lamination were obtained by ICP-AES in the Department of Earth Sciences at the University of Ottawa. A total of 10 elements were targeted for ICP-AES analysis, those most commonly analyzed in speleothem: Sr, Mg, Ca, Ba, Fe, Mn, Na, K, Al and S. Because of the robust nature of ICP-AES, the techniques utilized for this procedure were customized to maximize optimization and precision of the results, which is well suited for the high resolution approach to this study; the methods pertaining to ICP-AES are provided in *Appendix II*. Stable isotopes $\delta^{18}O$ and $\delta^{13}C$ from identical samples were also analyzed from the same samples using the isotope mass spectrometer in the G.G. Hatch Isotope Laboratory at the University of Ottawa, using the same procedure outlined in *Section 3.2.1*. Greyscale values were also measured to clearly delineate the laminations using rectangular sampling grids of the area running parallel to the growth axis from high resolution scans in *Image J®*.

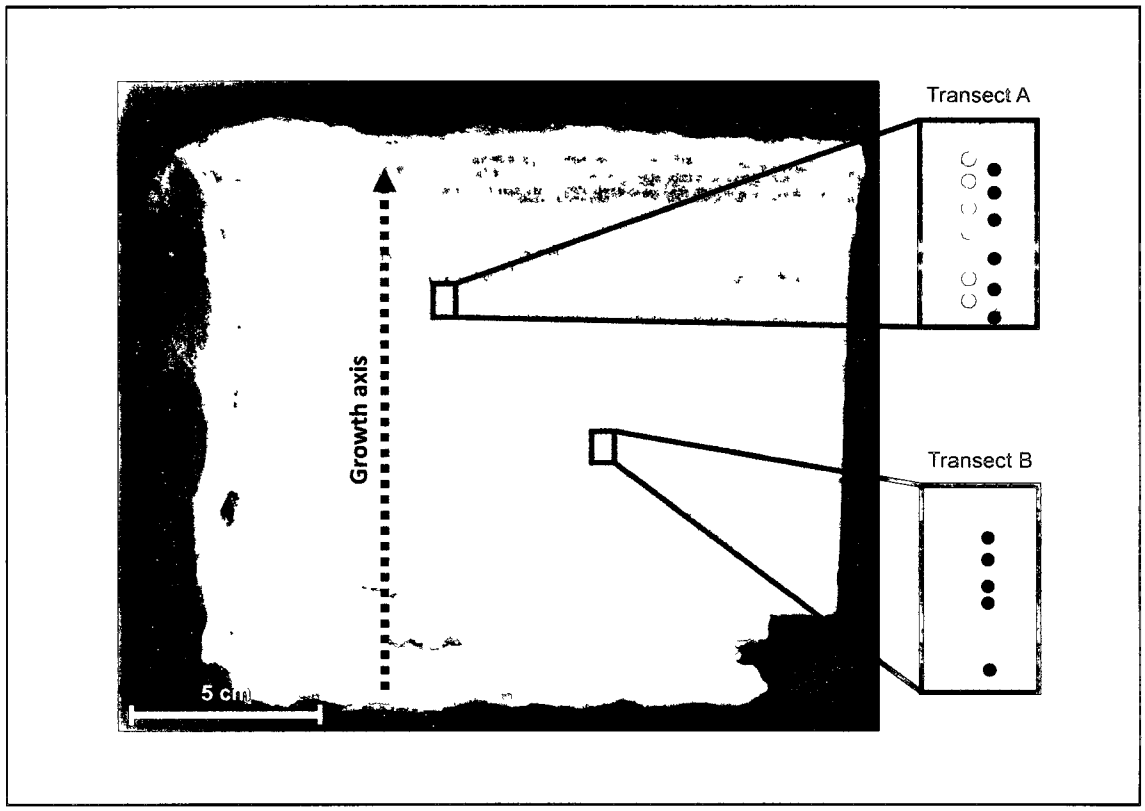

Figure 3.1. BC1-3 sampling *Transects A* (hard/dark calcite) & *B* (soft/light calcite) for trace elemental and stable isotope analysis. Points shown on transects indicate sampling locations for light (white) and dark (black) laminations.

3.3. Chronology building

Several methods were employed in attempts to improve the chronology for the BC1 flowstone. These include exploring epi-fluorescence spectroscopy to uncover any invisible laminations caused by yearly fluctuations in organic material incorporated in the speleothem at the time of deposition, the use of an existing paleomagnetic record completed on the flowstone to compare against known geomagnetic variations, and radiogenic He-dating to improve the age resolution.

3.3.1. Epi-fluorescent spectroscopy

The fluorescent properties of the BC1 flowstone were studied in the Department of Biology at the University of Ottawa using an Olympus BX-60 epifluorescent microscope and camera, using a blue-violet fluorescent UV filter with an excitation wavelength between 330-385 nm, and a peak emission wavelength at 470 ±20 nm. Attempts were made to acquire images using the petrographic thin sections as well as thicker sections (~1mm thick): the best results were produced from the traditional thin sections. Many sequential images of BC1 in thin section were acquired to produce a transect running parallel to the growth axis.

3.3.2. Paleomagnetism

A paleomagnetic study had been conducted previously on the BC1 flowstone, and thus are included in this thesis as magnetostratigraphic comparisons can be made. Analysis was completed in 2 studies; a first study by William Morris at McMaster University in 1987 focused on the lower part of the flowstone, and second by Jean-Pierre Pozzi at L'École Normale Supérieure in Paris, France in 2005-2006 was completed on the upper portion of BC1. Cored samples (measuring 23 mm in diameter) along the profile of BC1 were obtained for laboratory analysis. The base of the sample, block BC1-1, was excluded from this study due to its friable nature. Prior to analysis, the cores were cleaned ultrasonically in order to remove any possible contamination that was a result of the coring process. Small magnetic particles, likely hematite,

incorporated in the speleothem, either in the crystal lattice, inter-crystalline boundaries, or fluid inclusions, were the principle mineral targeted for analysis. Paleomagnetic measurements were obtained using a 2G Horizontal Cryogenic Magnetometer, and X, Y and Z values were simultaneously measured along the core at each cm to obtain the inclination and declination of the rock sample. The demagnetisation process in the magnetometer did not perturb the results of polarity observed when Natural Remnant Magnetism (NRM) measurements were made.

3.3.3. Radiogenic He-dating

Radiogenic He dating has been completed on the BC1 flowstone by Tobias Kluge at the University of Heidelberg in Germany in January of 2008, and this revealed an age of 3.23 +/- 0.65 Ma (2σ) near the top of the flowstone (*Figure 3.2*). This was accomplished using an extrapolation method and inverse modelling of thermally extracted radiogenic He, and a comparison with stalagmites bearing similar isotopic ratios. He-dating was continued at the MAPL Noble Gas Laboratory in the Department of Earth Sciences at the University of Ottawa in the spring of 2010 using the methods outlined in the subsections below. Initially, seven samples were chosen for dating in order to establish a dating chronology. All samples were chosen within the harder more compact calcite, targeting areas above and below the major discontinuities in order to gauge the duration of the hiatuses, including several sample duplicates; however time and instrumental failure limited the number of samples to be analysed. Two samples were analysed at the MAPL Noble Gas Laboratory. Sampling locations are indicated in *Figure 3.5*. BC1-3_{Base}, a 30 mm long core, 5 mm in diameter weighing 2.34g, was extracted first for analysis using a drill corer. It was later determined that separated crystals would provide more accurate results as it would eliminate matrix contamination, therefore BC1-4_{Base} was analysed using of 1.77g of separated crystals (*Figure 3.3)*. These crystals were washed in 0.2 M HCl for 10 minutes, and subsequently cleaned ultrasonically in acetone.

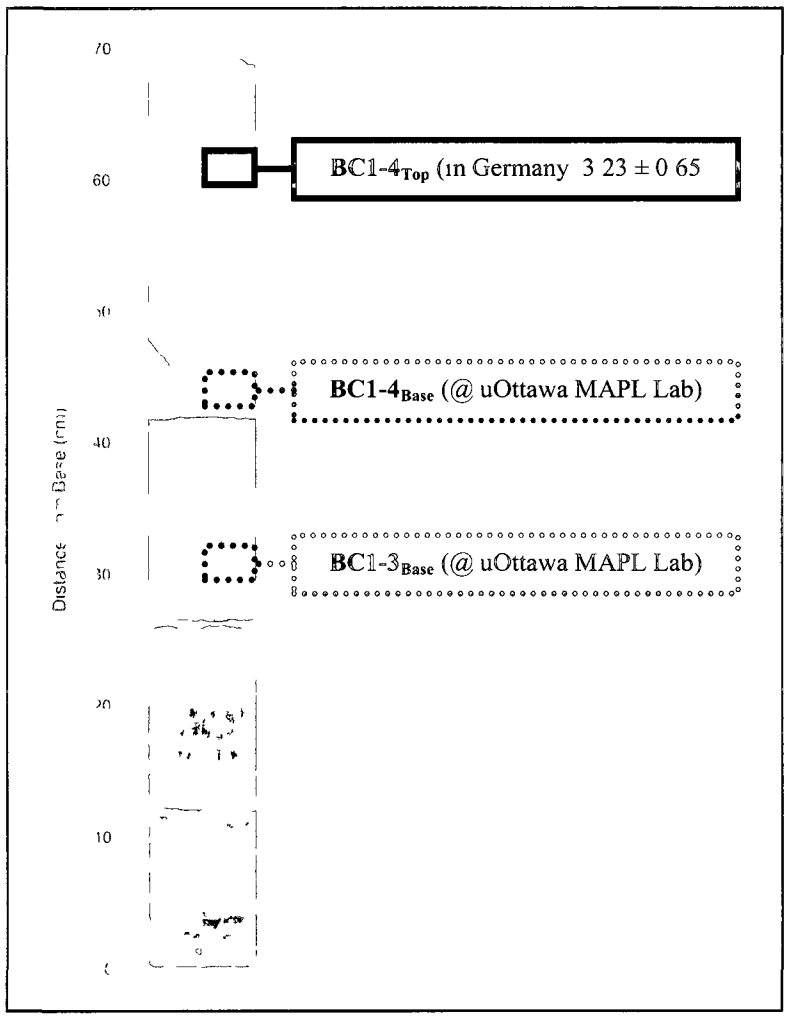

Figure 3.2. BC1 sample locations targeted for continued He-dating. Sampling locations denoted by dotted lines indicates samples dated at the uOttawa MAPL Lab, which are located within the harder/darker calcite microfabric group.

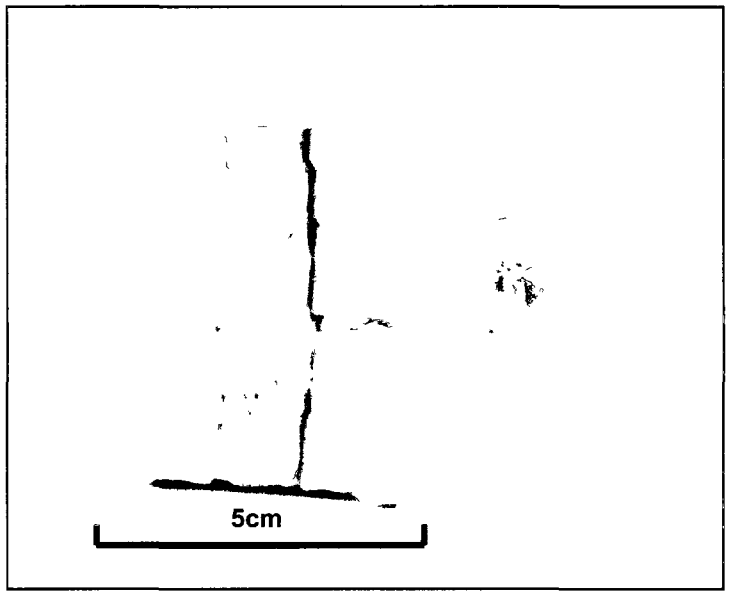

Figure 3.3. Crystal aggregates from BC1-4_{Base} used for He dating.

The experimental procedure for He isotopic analysis gas extraction is similar to that described in Mohapatra et al. (2009) and Greene et al. (2008). Gas extraction was carried out by heating the samples in an ultrahigh vacuum from 50 °C to 550 °C in steps. The extracted gas was cleaned of the reactive species- CH4, CO2, CO and O2 etc., by exposing it to a hot Ti sponge and SAES(r) getter pellets. He and Ne (standard tracer) were separated from the sample gas by exposing it to activated charcoal maintained at 76K. Mass spectrometric analysis was carried out on the separated He and Ne fraction on a MAP 215-50 noble gas mass spectrometer (MAPL). The experiment was calibrated by procedural blanks and air standard runs, periodically interspersed with the sample runs. *Figure 3.4* illustrates machine reproducibility (^{4}He sensitivity, ccSTP/volt) which shows no significant drift. Measured helium was further corrected for the atmospheric component by accompanying neon isotopic data using the *Equations 7* and *8*, where final age calculations were resolved using *Equations 5 & 6* (*see Section 1.5*).

$$^4He_{corr} = {}^4He_{meas} - {}^{20}Ne_{meas} * (^4He / {}^{20}Ne)_{air} \quad [7]$$

$$^3He_{corr} = {}^4He_{meas} - {}^{20}Ne^{meas} * (^3He / {}^{20}Ne)_{air} \quad [8]$$

The residual material for both samples used for He analysis was later analyzed for total U and Th concentrations at the University of Ottawa by ICP-MS, which included several duplicate runs. Samples were ground to a fine paste using a wet grinding method with acetone. Subsequently, 100 mg of dry sample was dissolved in concentrated HNO_3 (1 ml) and concentrated HCl (0.2 ml) at 150°C for 10 hours. A trace of HF was also added to destroy any micro-nano-sized particles of silicates left from the detrital component of the sample. Samples were analyzed after necessary further dilution (to reduce high Ca matrix effects) with distilled water.

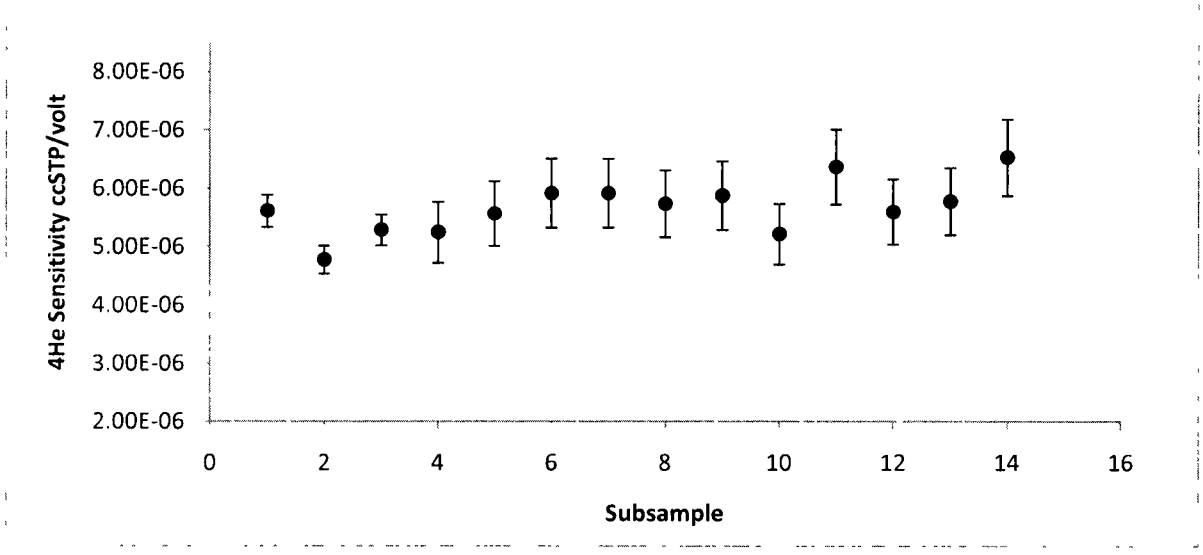

Figure 3.4. Machine reproducibility (^{4}He sensitivity) at 2σ.

4. RESULTS & ANALYSIS

The following chapter presents the results of this study in three sections. A first section summarizes the results from the petrographic study, including the crystallography and scanning electron micrography. A second section highlights the results from the geochemistry study, including a comprehensive stable isotope record incorporating the crystallographic record to analyze the isotopic signatures of each of the microfabrics of BC1, as well as a high-resolution geochemical study on two smaller transects within two individual microfabrics, one of which is suspected to be a recrystallization zone. A third section presents the results of the various methods which aimed to improve chronology of the BC1 flowstone.

4.1. Petrography

4.1.1. Crystallographic study

A detailed crystallographic study revealed a total of 8 distinctly different calcite microfabrics present throughout the flowstone from Bear Cave. No microscopic evidence of aragonite was observed from the petrographic study. Detailed descriptions of each of the calcite microfabrics are outlined in *Table 4.1*, with examples of each fabric in crossed-polarized light and simplified schematic diagrams provided in *Figure 4.1*. These microfabrics are categorized into 3 different subgroups. The first includes the softer, lighter, finer-textured and more porous calcite which includes *Micrite* (microcrystalline), *Sparite* (equant) and a *Branched* (dendritic) fabric. The second grouping encompasses transitional textures, consisting of stunted columnar crystals (*Short Columnar*), and pore-filling mosaics which include longer columnar crystals in-filled by sparite (*Columnar-with-Sparite*) or by branching crystallites (*Columnar-with-Branched*). The final grouping consists of the harder, darker, coarser-textured and denser calcite which includes *Elongate Columnar* and *Palisade* crystals. Complete documentation of crystallographic distribution along the profile of BC1 is illustrated together with the stable isotope profile in *Figures 4.6 - 4.9* (*see Section 4.2.1.*). Petrographic transects of BC1 in thin section are provided in *Appendix I.* It is important to note that actual growth layers along a single horizon are non-linear, particularly in the case of the BC1-1 block likely due to uneven

nucleation surfaces; however for the purpose of this study, calcite growth layers are represented using linear approximations.

In general, larger fabrics have their crystals oriented with their long direction parallel to the direction of growth, where smaller microfabrics have no preferred orientation. Growth banding is more prominent in the larger crystal fabrics, namely the *Elongate Columnar* and *Palisade* fabrics. Several depositional hiatuses were observed throughout the profile of BC1, also shown in *Figures 4.6. - 4.9.* Examples of both major and minor hiatuses are shown in crossed-polars in *Figure 4.3.* Major hiatuses are followed by an abrupt shift in calcite microfabric, either bridging between two separate fabrics or truncating the growth sequence. This includes the three major discontinuities that separate the four blocks. Several minor hiatuses were also documented, where no change in microfabric was observed. Major hiatuses are more prominent in the two lowermost blocks (BC1-1 & BC1-2), whereas minor hiatuses dominate the two uppermost blocks (BC1-3 & BC1-4).

The *Columnar-with-Sparite* crystals are the most frequently occurring microfabric along the profile of BC1, accounting for nearly 1/3 of all microfabrics, where *Short Columnar* is the most infrequent at only 2%. *Columnar-with-Branched* as well as the softer *Sparite* and *Branched* fabrics also had lower frequencies, at 7%, 5% and 9% respectively. *Micrite* was the most commonly occurring microfabric within the grouping of softer fabrics at 16%. Both microfabrics from the harder grouping, *Elongate Columnar* and *Palisade* calcite, were also recurrent throughout the BC1 profile, with frequencies of 13% and 16% respectively. It was noted that there was a clear recurring pattern of progressive crystal growth throughout the profile of BC1, meaning a gradual increase in crystal size following a hiatus in deposition. For instance, crystal growth would develop from a fine crystal fabric to progressively larger crystal fabrics. This was particularly evident following a hiatus, which would generally be followed by layer of 'length-slow' *Micrite*, *Sparite* or *Branched* fabrics, followed by a competitive growth phase, which would develop into the 'length-fast' *Elongate Columnar* or *Palisade* calcite (Folk & Assereto, 1976). The *Short Columnar* microfabric was often observed to precede or follow a hiatus in deposition or softer fabrics. In addition, calcite surrounding the major discontinuities were dominated by the softer fabrics, namely by microcrystalline calcite.

Table 4.1. Description of calcite microfabrics present in BC1.

Group	Microfabric	Structure	Frequency	Description
(I) Softer, lighter, finer, more porous microfabrics	*Micrite (microcrystalline)*	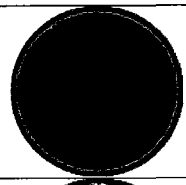	16 %	-Crystals are so small they are nearly unresolvable using a petrographic microscope. -Generally less than 4 microns in size. -Commonly precedes or follows a hiatus in deposition.
	Sparite (Equant)	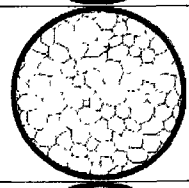	5 %	-Having nearly the same length in all directions. -Ranging from several millimetres to only several micrometers in width. -Random orientation of crystals.
	Branched (dendritic)	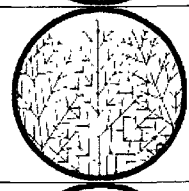	9 %	-Crystallites take on a multi-branching tree-like form. -Generally only several hundred microns long.
(II) Transitional microfabrics	*Short Columnar*	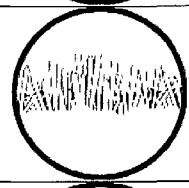	2 %	-Short columnar-shaped crystals <3 mm in length. -Usually follows a hiatus in deposition or softer calcite. -Length:width ratios >3:1
	Columnar-with-Sparite	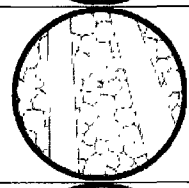	32 %	-An assemblage of elongate, roughly parallel loosely packed calcite crystals (>3mm in length), with sparite filling in the inter-crystalline boundaries.
	Columnar-with-Branched	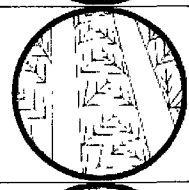	7 %	-An assemblage of elongate, roughly parallel loosely packed calcite crystals (>3 mm in length), with branching poly-crystallites (slightly larger than the dendritic microfabric) between inter-crystalline boundaries, where secondary branching is observed.
(III) Harder, darker, coarser, more dense microfabrics	*Elongate Columnar*	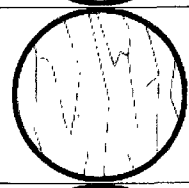	13 %	-An assemblage of elongate and tightly packed calcite crystals (>3mm in length), with jagged crystal boundaries. -Length:width ratios >4:1
	Palisade	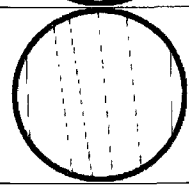	16 %	-An assemblage of elongate, tightly packed calcite crystals (3-50+ mm in length), with straight parallel sides. -Length:width ratios >4:1

Note: Field of view of microfabric structure is approx. 5 mm in diameter.

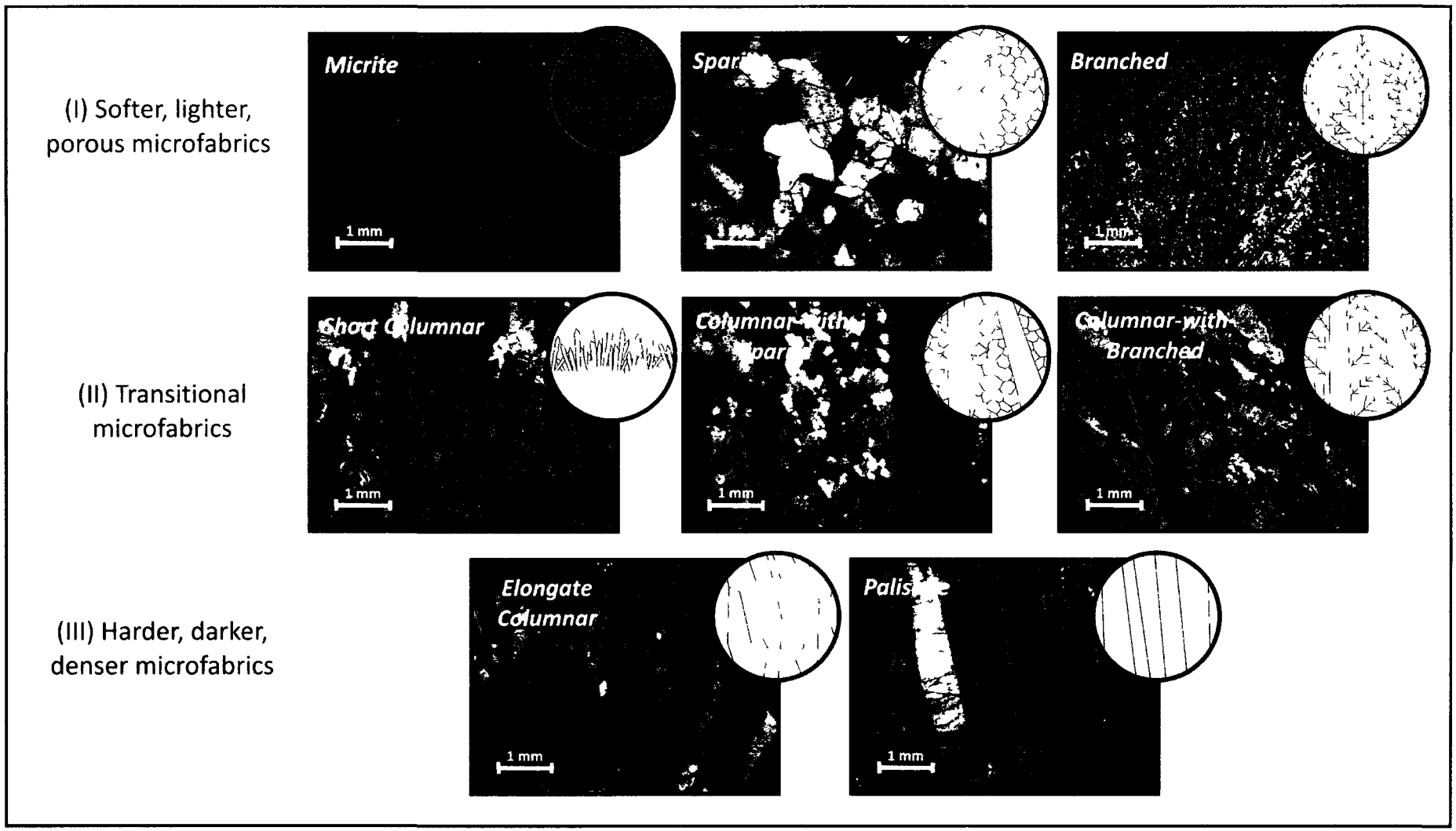

Figure 4.1. Calcite microfabrics of BC1 in crossed-polars with simplified schematic diagrams. Images are oriented with growth direction facing upwards

BC1-1, the oldest block corresponding to the base of the flowstone, is 140 mm thick. This block is characterized by a dark reddish-brown colour and its friable nature. Frequent shifts in calcite microfabric type were observed from the crystallographic study, as well as several major hiatuses (*Figure 4.6*). Progressive crystal growth was particularly evident in this block, with repeated cyclical growth of smaller crystal fabrics developing into the transitional pore-filling mosaics and finally to the harder calcite fabrics. *Short Columnar* fabrics were often found to precede or follow a hiatus in deposition, often a precursor to the development of larger crystal fabrics. Slightly radiating acicular *Elongate Columnar* and *Palisade* crystals in some cases greater than 30 mm long are present near the base, exclusive to this block. Visible laminae were observed in greatest detail in the harder fabrics.

The second block in this stratigraphic sequence, BC1-2, is 135 mm thick and marked by an initial phase of rapid progressive crystal growth followed by more consistent deposition which includes a thick layer of *Columnar-with-Sparite* and terminated by more prominent layers of finely crystalline fabrics (*Figure 4.7*). A distinctly darker layer is evident roughly 8 mm from the base, likely rich in iron or detritus; however its composition remains uncertain as no chemical analyses were performed on this layer. The subtle white line on the scan of BC1-2 in *Figure 4.7*, ~32 mm from the base, is the result of uneven polishing on the surface and not a distinct layer. Within the uppermost segment (approximately 7 cm from the base), an exceptionally thick layer of *Sparite* was observed (~1.8 cm thick), positioned below a major depositional hiatus, comprising tightly-packed interlocking grains with a random orientation and multiple hiatuses (*Figure 4.2.a*). Some minor hiatuses are visible within this fabric giving evidence of euhedral crystal terminations which appear to be relict of an *Elongate Columnar* or *Palisade fabric*. A more lightly coloured *Branched* and *Micrite* fabric are found towards the pinnacle of this block, which are distinctly more porous than neighbouring crystals. These layers of softer and more porous calcite are characterized by a whitish-beige colour, which is the product of the optical structure of the numerous micron-sized calcite crystallites which cause a reflection of incident light (White, 2007, p.162). Many instances of post-depositional in-filling can be observed in the porous layers of the *Micrite* microfabric (*Figure 4.3.*), implying infiltration of secondary waters causing secondary precipitation.

BC1-3 is 153 mm in thickness, and consists of a thick layer of finely textured *Micrite* and *Branched* fabrics near the base that sharply evolves into thicker layers of alternating hard and transitional pore-filling fabrics with softer layers interspersed in between (*Figure 4.8*). This block has distinct colour banding at both the macroscopic level, with prominent growth laminae at the microscopic level. Harder crystal fabrics are generally observed to be darker in colour; interestingly, some layers of harder calcite were observed to be lighter in colour. The top of the block is marked by a layer of *Micrite* punctuated by multiple depositional hiatuses, followed by a fine layer of *Short Columnar* crystals.

The uppermost block, the youngest section of the flowstone, is the thickest at 270 cm thick. The base of the block corresponds with another occurrence of clear progressive crystal growth, where several changes in crystal fabric are observed over a short distance, which is then followed by thick, well-developed layers of the harder and transitional variety, indicative of more consistent deposition (*Figure 4.9*). White and brownish bands are clearly visible along the length of the block, with multiple minor hiatuses found within the *Palisade* and transitional layers. Numerous stalactite fragments were found roughly 17 mm from the base of this block (not seen on scans) which corresponds with a whitish layer and a minor hiatus. This could possibly be indicative of a major earthquake in the region, causing the stalactites to fall from the cave ceiling and become incorporated in the flowstone as calcite growth continues.

4.1.2. Scanning Electron Micrography

Scanning Electron Micrograph (SEM) images of several of the microfabrics observed in BC1 are shown in *Figure 4.4*. Dark material between crystal boundaries had high concentrations of C, suggests that it is most likely organic material. Several rare earth elements were also discovered in the intercrystalline boundaries, such as Au and W, which are most likely deposited by seepage waters. SEM analysis also allowed us to observe a framboidal pyrite in perfect condition present in the intercrystalline boundaries of a harder *Palisade* layer at the base of BC1-4 (*Figure 4.4, J*-K).

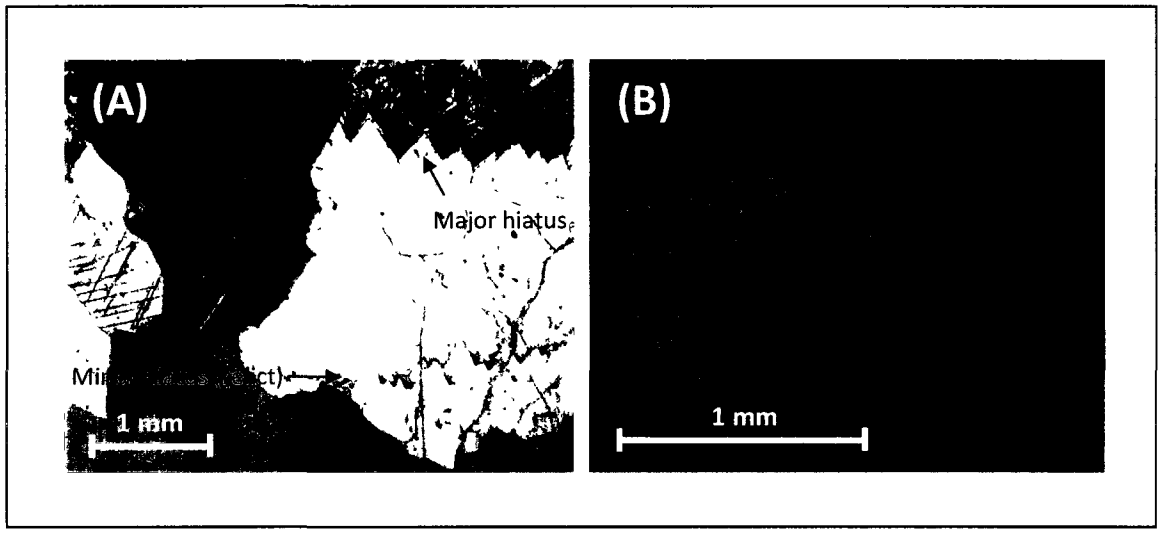

Figure 4.2. Depositional hiatuses: (A) A minor hiatus followed by a major hiatus in an anomalous patch of *Sparite* in BC1-2; and (B) a major hiatus accompanied by an abrupt shift in microfabric within BC1-1. Note different scales on A & B.

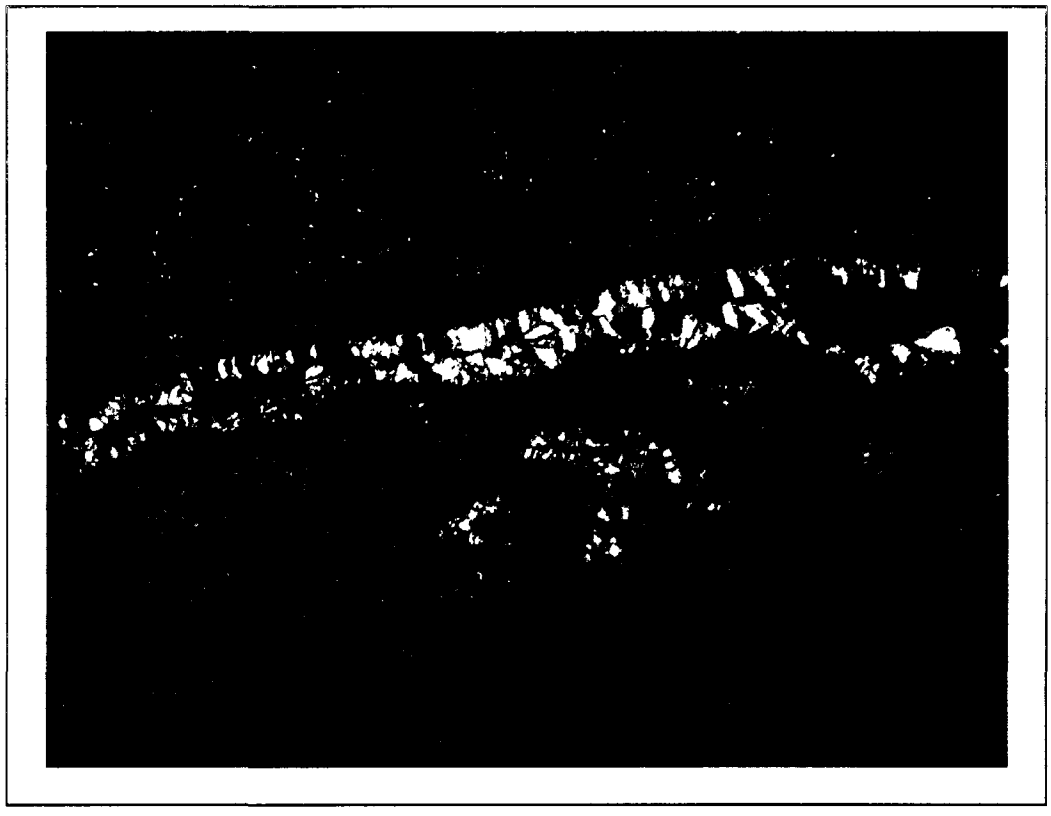

Figure 4.3. Post-depositional in-filling observed in the porous microcrystalline layers of BC1-2.

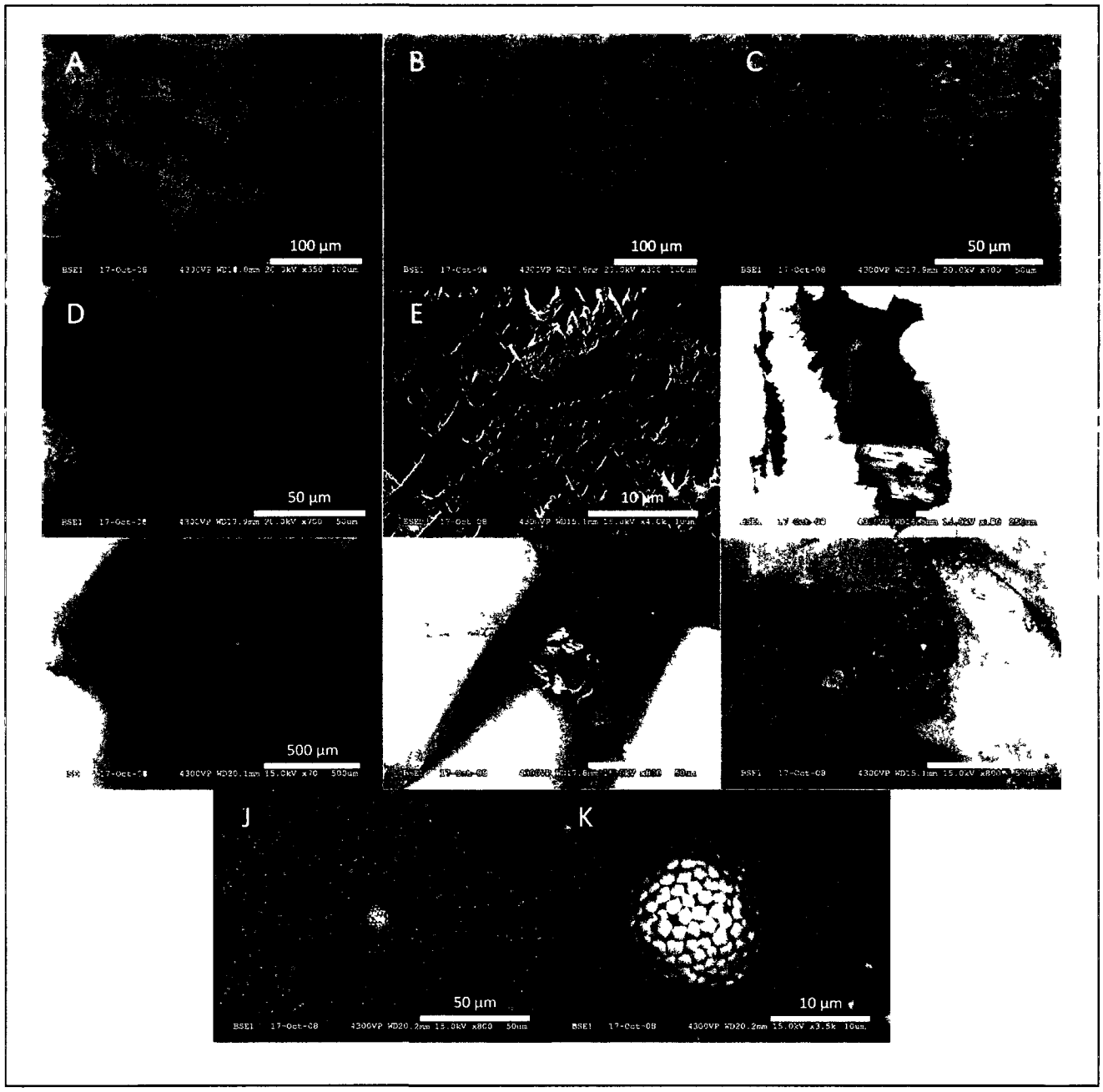

Figure 4.4. Scanning electron micrograph images of the BC1 flowstone: (A) Columnar crystals and euhedral crystal terminations, (B-C) Columnar crystals with clearly defined euhedral crystal terminations, with micrite and sparite in-filling the intercrystalline boundaries, (D) Columnar crystals, (E) Dendritic microfabric, (F) Parallel crystal boundaries coated with dark material, (G-I) Various organic and inorganic material between crystal boundaries, (J-K) Framboidal pyrite found within dark organic material on intercrystalline boundaries.
Note differing scales on images.

4.1.3. Summary

- A total of eight distinctly different microfabrics were present throughout the profile of the BC1 flowstone, which can be categorized into 3 different groupings:
    - (I) Softer, lighter, finer-textured and more porous calcite which includes *Micrite*, *Sparite* and a *Branched* crystallites;
    - (II) Transitional textures, consisting of stunted columnar crystals (*Short Columnar*) and pore-filling mosaics which include longer columnar crystals in-filled by sparite (*Columnar-with-Sparite*) or by branching crystallites (*Columnar-with-Branched*);
    - (III) Harder, darker, coarser-textured and denser calcite represented by *Elongate Columnar* and *Palisade crystals*.
- Recurring progressive crystal growth phases were particularly evident following hiatuses in deposition, where crystal growth develops from the finer crystal fabric to progressively coarser crystal fabrics.
- Growth banding is more clearly observed in the coarser and harder crystal fabrics.
- Major hiatuses (bridging shifts in microfabric type or breaks in the growth sequence, discontinuities) were more frequent in the lower portion of the flowstone whereas minor hiatuses (occurring within one single microfabric layer) dominated the uppermost segment of BC1.
- Post-depositional in-filling was observed in some of the porous microcrystalline layers.
- A framboidal pyrite was found with its delicate structure perfectly intact in the intercrystalline boundaries of one of the denser *Palisade* layers.

4.2. Geochemistry

4.2.1. Stable isotope profile ($\delta^{13}C$ & $\delta^{18}O$)

A continuous record of $\delta^{18}O$ and $\delta^{13}C$ (VPDB) along the growth axis of the BC1 flowstone is presented in *Figure 4.5*. Larger-scale transitions between crystallographic sub-groupings are also illustrated. The two isotopic profiles are also presented in greater detail to compliment the crystallographic study in *Figures 4.6 to 4.9*. These profiles are presented relative to the untouched archival scans of each block; therefore sampling locations cannot be seen on these figures. Significant variability was observed in both isotope records ($\delta^{18}O$ and $\delta^{13}C$), with the strongest variations observed at both ends of the flowstone, and abrupt shifts located at major discontinuities. Several horizons experienced simultaneous shifts in both $\delta^{13}C$ and $\delta^{18}O$ in tandem with abrupt shifts in calcite microfabric. Simultaneous shifts are periodically observed in both isotopes when transitioning between the harder calcite fabrics and the softer and transitional groupings; however these shifts are comparable to the variability within the record. In addition, considerable variability is observed within uniform microfabric layers. $\delta^{13}C$ values range from -3.83‰ to -8.32‰, where $\delta^{18}O$ has extreme values around -16.07‰ and -18.52‰.

Mean $\delta^{18}O$ values from the BC1 flowstone are consistent with other interglacial cave calcite deposits in the Rocky Mountains of British Columbia and Alberta. The speleothem deposits from Castleguard Cave in the Columbia Ice fields of Alberta (51° 10 'N, 115° 33' W) are estimated to be approximately 0.7 to 1.0 Ma in age (Gascoyne *et al.*, 1983), deposited some time during the Yarmouthian Pleistocene interglacial. The mean $\delta^{18}O$ value from the BC1 flowstone was found to be -17.21‰, very similar to that of the speleothem from Castleguard Cave, which center around 17.0‰ (Harmon *et al.*, 1983). The mean $\delta^{13}C$ value from the BC1 flowstone was found to be -6.0‰, far more depleted than the speleothem from Castleguard Cave, which fall around -0.5‰ (Harmon *et al.*, 1983), suggesting a marked increase in organic activity in the Bear Cave region.

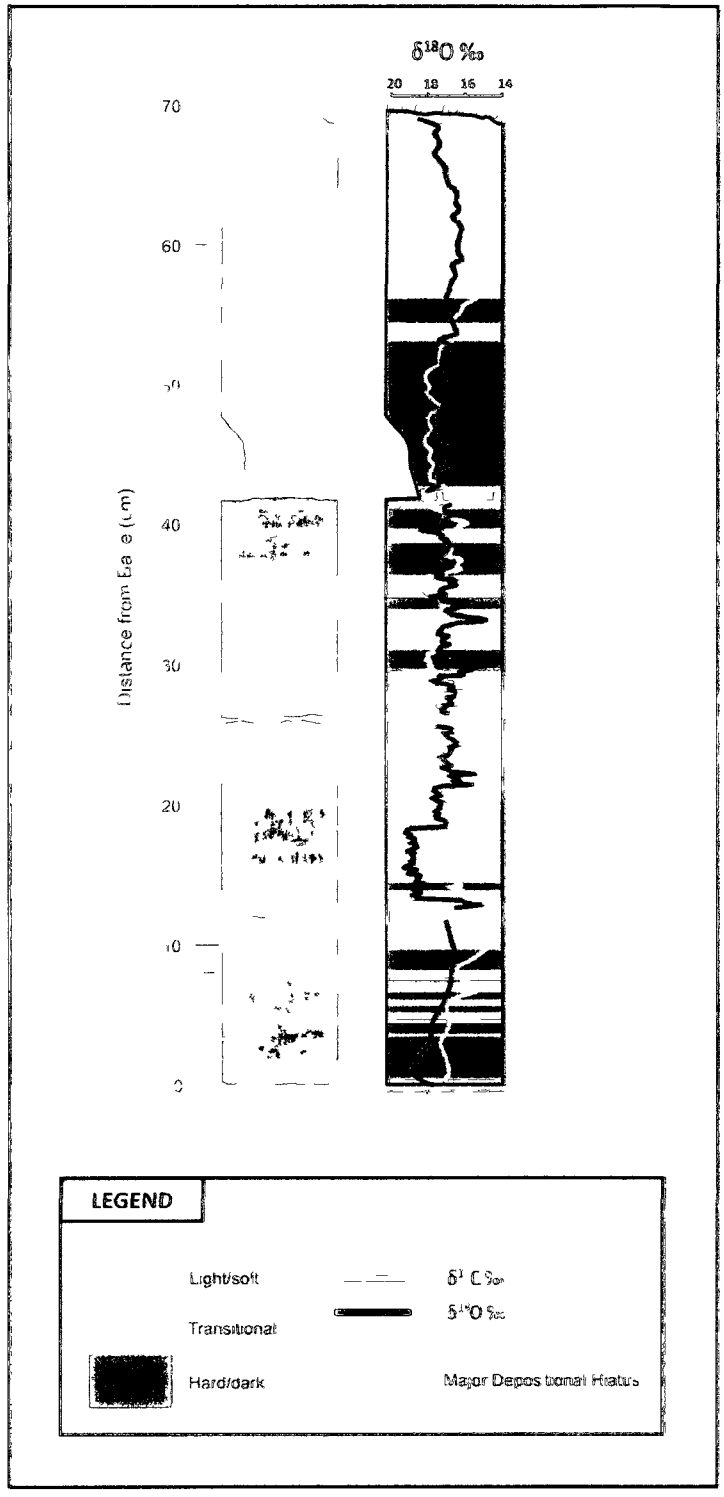

Figure 4.5. Stable Isotope (^{13}C & ^{18}O) profile for the BC1 flowstone. Sampling resolution is at 1.5 mm, excluding BC1-1 & BC-4 which were sampled at 1.5-10 mm intervals. Note breaks in curve located at major discontinuities.

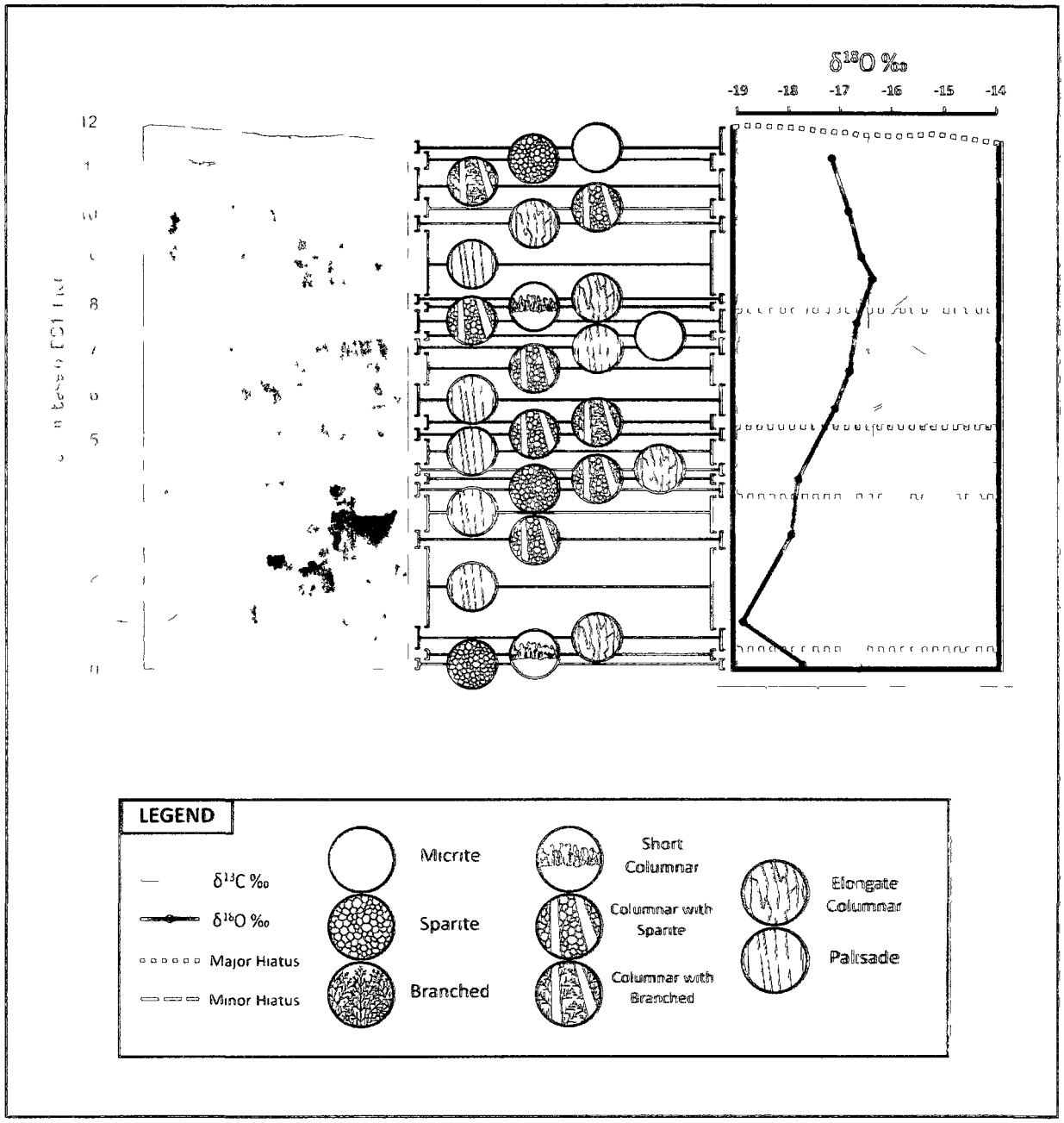

Figure 4.6. Stable Isotope (^{13}C & ^{18}O) and crystallographic variations within BC1-1.

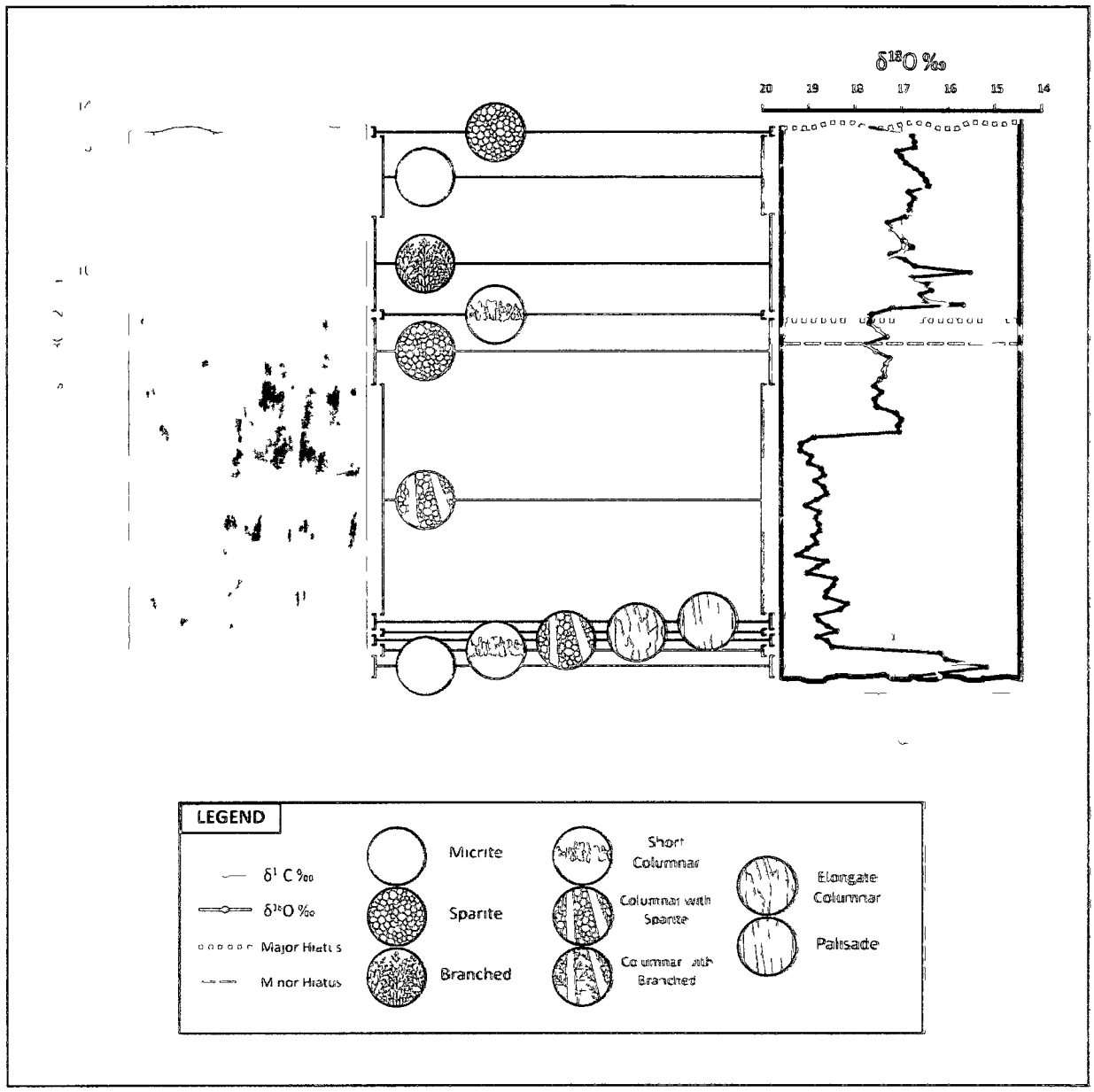

Figure 4 7 Stable Isotope (^{13}C & ^{18}O) and crystallographic variations within BC1-2

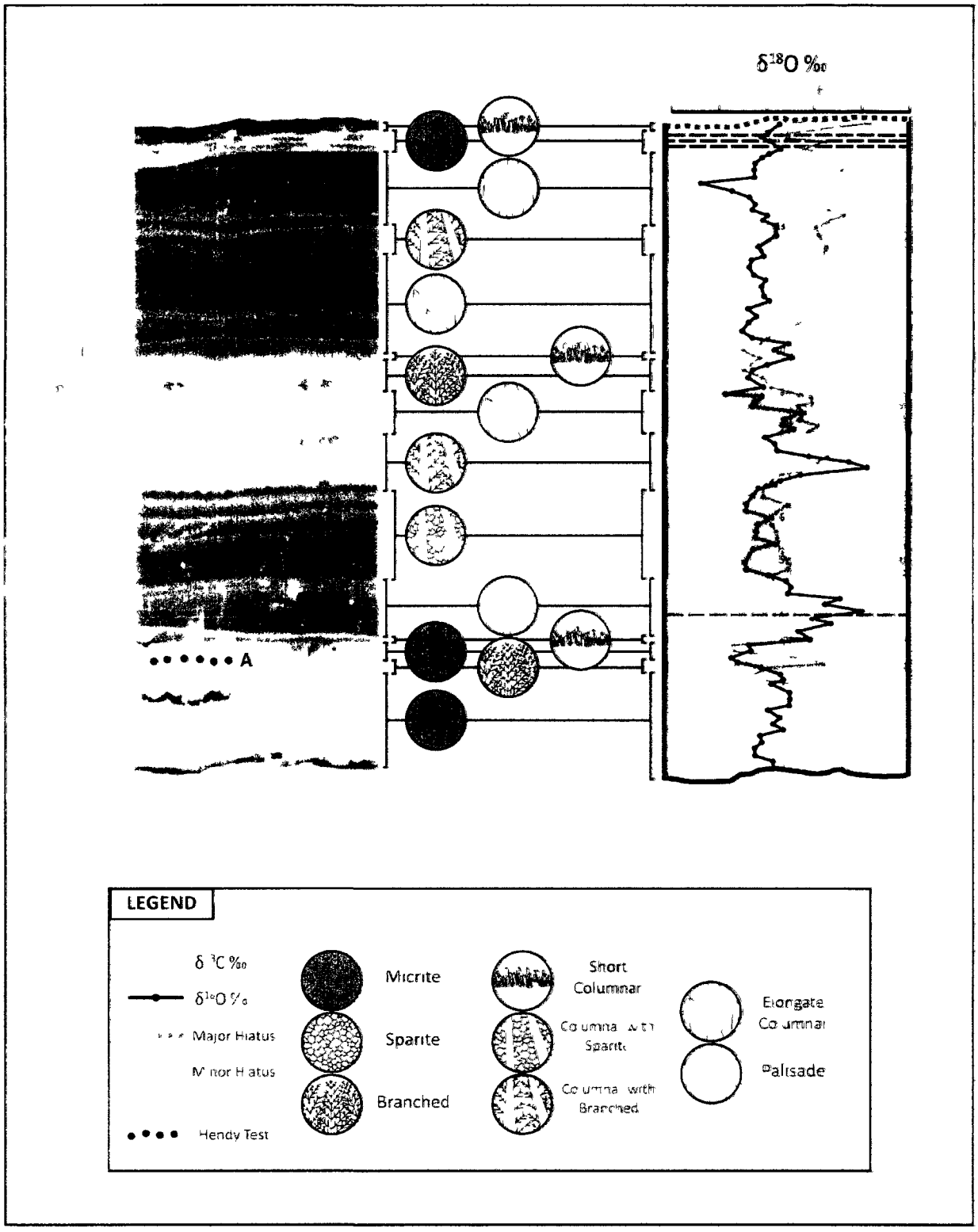

Figure 4.8. Stable Isotope (^{13}C & ^{18}O) and crystallographic variations within BC1-3

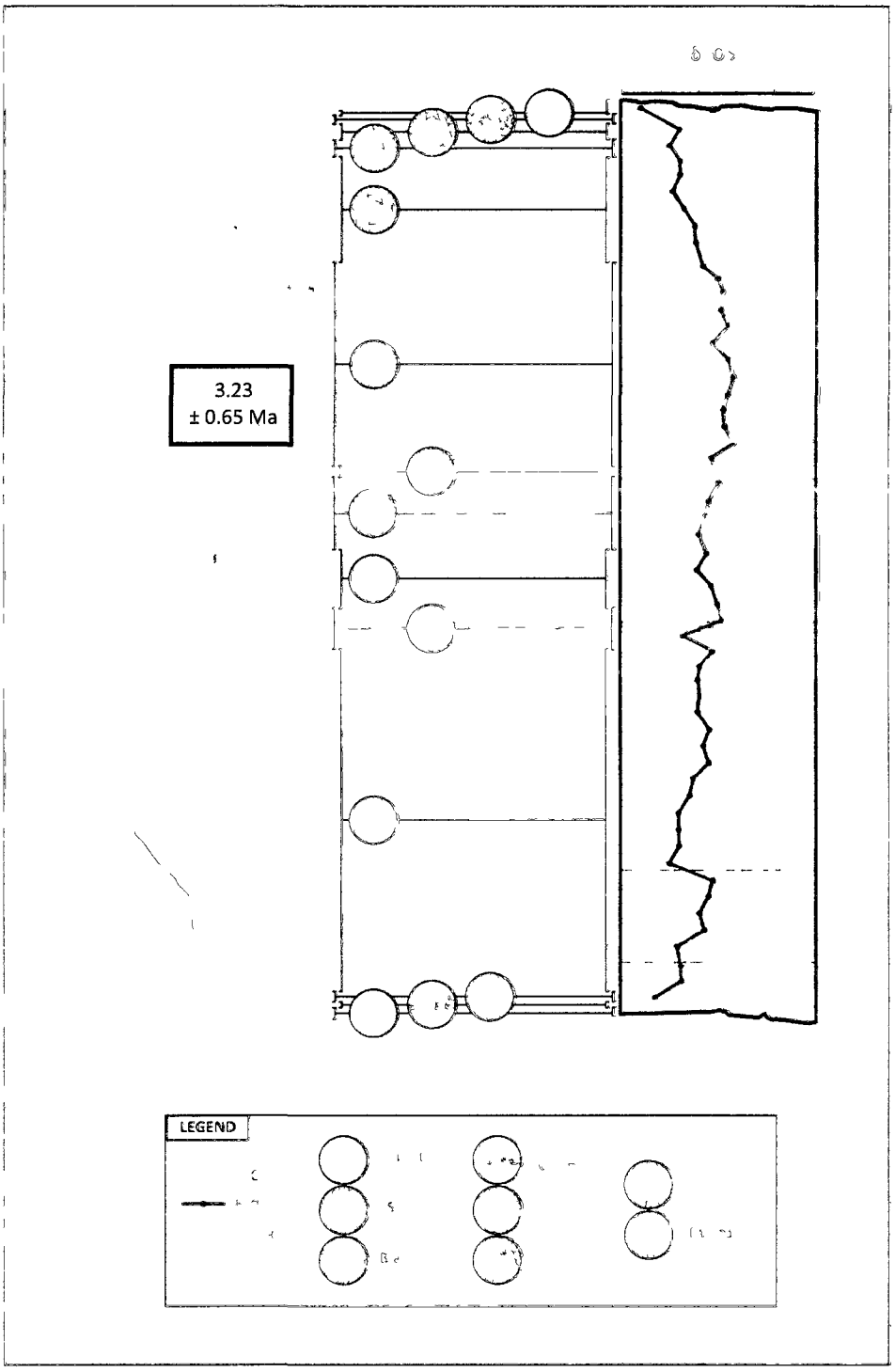

Figure 4.9. Stable Isotope (^{13}C & ^{18}O) and crystallographic variations within BC1-4. Preliminary He-date obtained from Germany denoted by solid black line.

Hendy tests were performed on two growth layers chosen within BC1-3 due to its clear visible banding. These tests were completed prior to the crystallographic study during the initial sampling of isotopes. Sampling locations for both layers are indicated on *Figure 4.8*; these include (A) a lighter layer within a *Branched* microfabric zone, ~25 mm from the base, and (B) a darker layer within a *Columnar-with-Branched* microfabric zone, ~65 mm from the base. Results from the Hendy Tests are illustrated in *Figure 4.10*. The left panels show the absence of a simultaneous enrichment of $\delta^{18}O$ & $\delta^{13}C$ with distance from drip source along either layer. However, correlations between $\delta^{18}O$ & $\delta^{13}C$ for both layers (right panels) reveal somewhat inconclusive results as there is some suggestion of a progressive co-linear relationship between $\delta^{18}O$ & $\delta^{13}C$, yet not definitive.

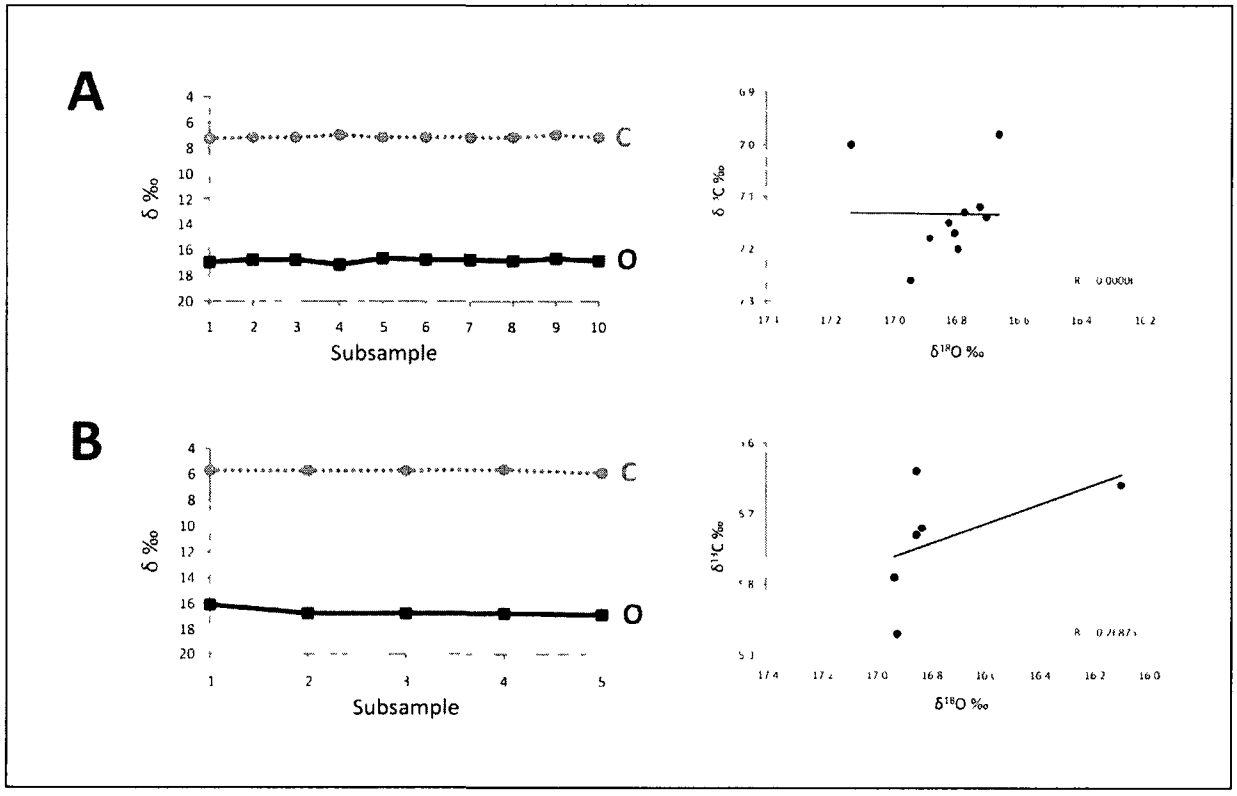

Figure 4.10. Hendy Test results for a light (A) and dark (B) layer within BC1-3.

4.2.2. Isotopic signatures of BC1 microfabrics

There are several instances in the record when both isotopes co-vary, and this may be problematic for paleoenvironmental/paleoclimatic interpretation as the covariation of isotopes along a crystallographic profile may be symptomatic of kinetic fractionation effects prior to or during calcite precipitation, such as evaporative conditions in the cave or CO_2 degassing in the epikarst, or the result of post-depositional diagenesis in the form of recrystallization (Hendy, 1971). To investigate this further, the $\delta^{13}C$ & $\delta^{18}O$ profiles were examined relative to the crystallographic record to try to make sense of some of these occurrences. All $\delta^{13}C$ & $\delta^{18}O$ isotope points along the BC1 profile (n = 256) were used together with corresponding crystal microfabric type in order to examine the isotopic signatures of each of the microfabrics of BC1; these data are summarized in *Appendix III.*

Figure 4.11 illustrates the isotopic ranges for each microfabric. Due to the low frequency of the *Short Columnar* microfabric and the particularly short range at which these layers occur, this microfabric was omitted from this part of the study, as it would have been difficult to state with confidence that these fabric layers were sampled with precision. When applying the stable isotope record to the crystallographic study, it was found that each of the microfabrics fell over slightly overlapping, yet different isotopic ranges. Most of the microfabrics have a relatively wide isotopic range, including *Micrite*, *Columnar-with-Sparite*, *Columnar-with-Branched*, *Elongate Columnar* and the *Palisade* calcite. *Sparite*, *Branched* and *Columnar-with-Branched* all have narrower isotopic ranges, most notably for the $\delta^{18}O$ range of the *Sparite* fabric. The average $\delta^{13}C$ values for these three microfabrics, *Sparite*, *Branched* and *Columnar-with-Branched*, all deviate most from the overall average for BC1. This also includes the average $\delta^{18}O$ values for *Sparite* and *Columnar-with-Sparite*. Interestingly, *Sparite* and its transitional counterpart, *Columnar-with-Sparite* both possessed similar averages and ranges. This relationship is analogous for the *Branched* fabric and its transitional relative, *Columnar-with-Branched.*

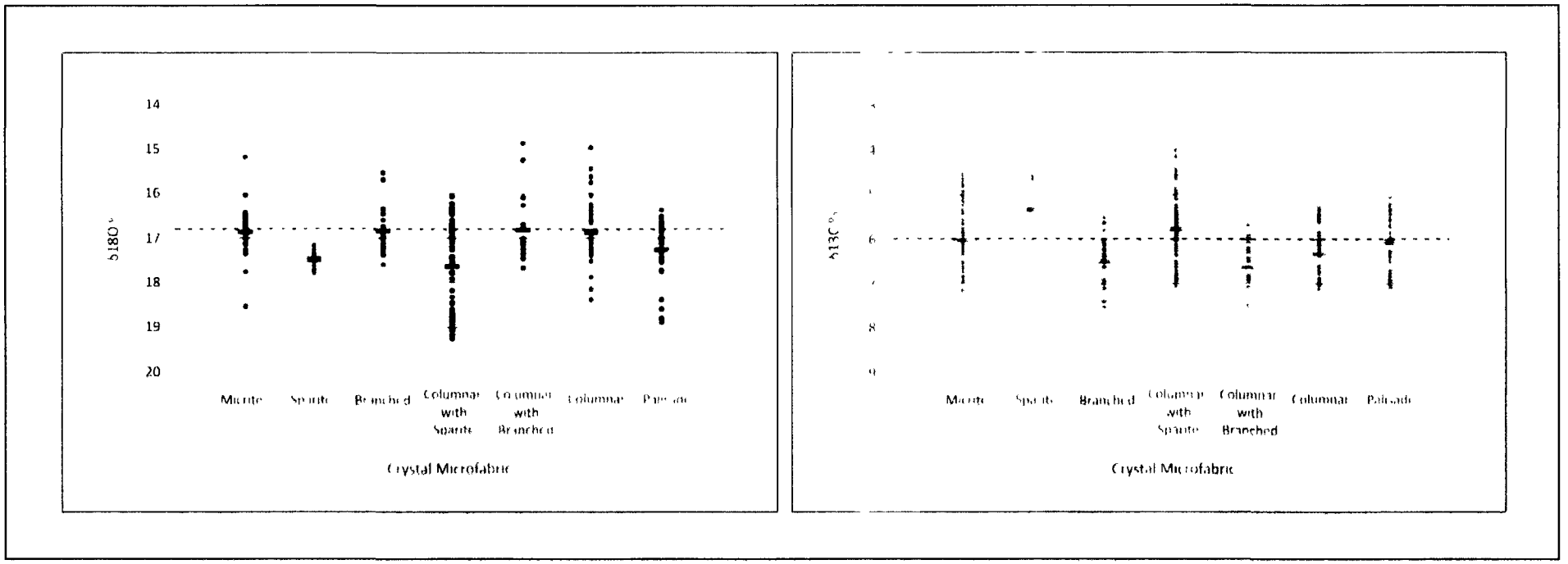

Figure 4.11. $\delta^{13}C$ and $\delta^{18}O$ isotopic ranges for each microfabric. Mean $\delta^{13}C$ and $\delta^{18}O$ values for the BC1 flowstone is denoted by the dashed line, with individual mean values for each of the microfabric denoted by the blue ($\delta^{18}O$) and orange ($\delta^{13}C$) tick marks.

A plot of $\delta^{13}C$ against $\delta^{18}O$ for all sampling points along the profile of BC1 reveals a cloud of points (*Figure 4.12-A*) with no correlation between $\delta^{13}C$ & $\delta^{18}O$, which is ideal for paleoclimatic interpretation (Hendy, 1971); however this is not entirely the case when each microfabric is plotted individually(*Figure 4.12-B*). The relationships between $\delta^{13}C$ & $\delta^{18}O$ for each individual microfabric are illustrated in greater detail in *Figure 4.13*. In general, there is no significant correlation between $\delta^{13}C$ & $\delta^{18}O$ ($p = 0.01$) for the harder microfabrics (*Elongate Columnar* and *Palisade*), which display a scattered cloud of points. Two of the microfabrics exhibit weak but significant ($p \leq 0.01$) positive linear correlations between $\delta^{13}C$ & $\delta^{18}O$, including *Micrite* ($R^2 = 0.25$) and *Columnar-with-Branched* ($R^2 = 0.45$), which appears to display a logarithmic-like curve.

The *Columnar-with-Sparite* microfabric is also suspicious as it appears to have two populations from the $\delta^{13}C/\delta^{18}O$ plot. These two populations may be spotted on the isotopic profile of BC1-2, where an abrupt shift in both isotopes occurs roughly 6cm from the base of the block (*Figure 4.7*). Observations from the crystallographic study regarded the upper portion of this layer as having less-compact sparite filling in the boundaries between the columnar crystals. Curiously, the anomalously thick layer of *Sparite* sits atop this layer in question (~7 cm from base of BC1-2), which is truncated by a major depositional hiatus (~9cm from base of BC1-2).

Questions may also be raised about the *Branched* microfabric, as its $\delta^{13}C/\delta^{18}O$ plot exhibits a slight mushroom-like tendency, however this trend disappears with the removal of one or two data points, and may not be significant due to the low sample number ($n = 22$).

Table 4.2 shows the slopes of the $\delta^{13}C/\delta^{18}O$ lines for each microfabric. The *Sparite* microfabric plot revealed an exaggerated slope ($m = 1.85$) in comparison to the other microfabrics, where little change was observed in $\delta^{18}O$ with respect to $\delta^{13}C$, which may be a consequence of recrystallization. *Micrite* also displays clustering at fixed $\delta^{18}O$ values; however the data have a wider spread compared to samples taken within the *Sparite* microfabric. All other softer and transitional microfabrics possessed relatively positive slopes, whereas both harder microfabrics exclusively displayed negative slopes. It is important to note that although the relationship between $\delta^{13}C$ & $\delta^{18}O$ for the *Elongate Columnar* fabric is close to significance ($p = 0.03$), it does not show relative enrichment.

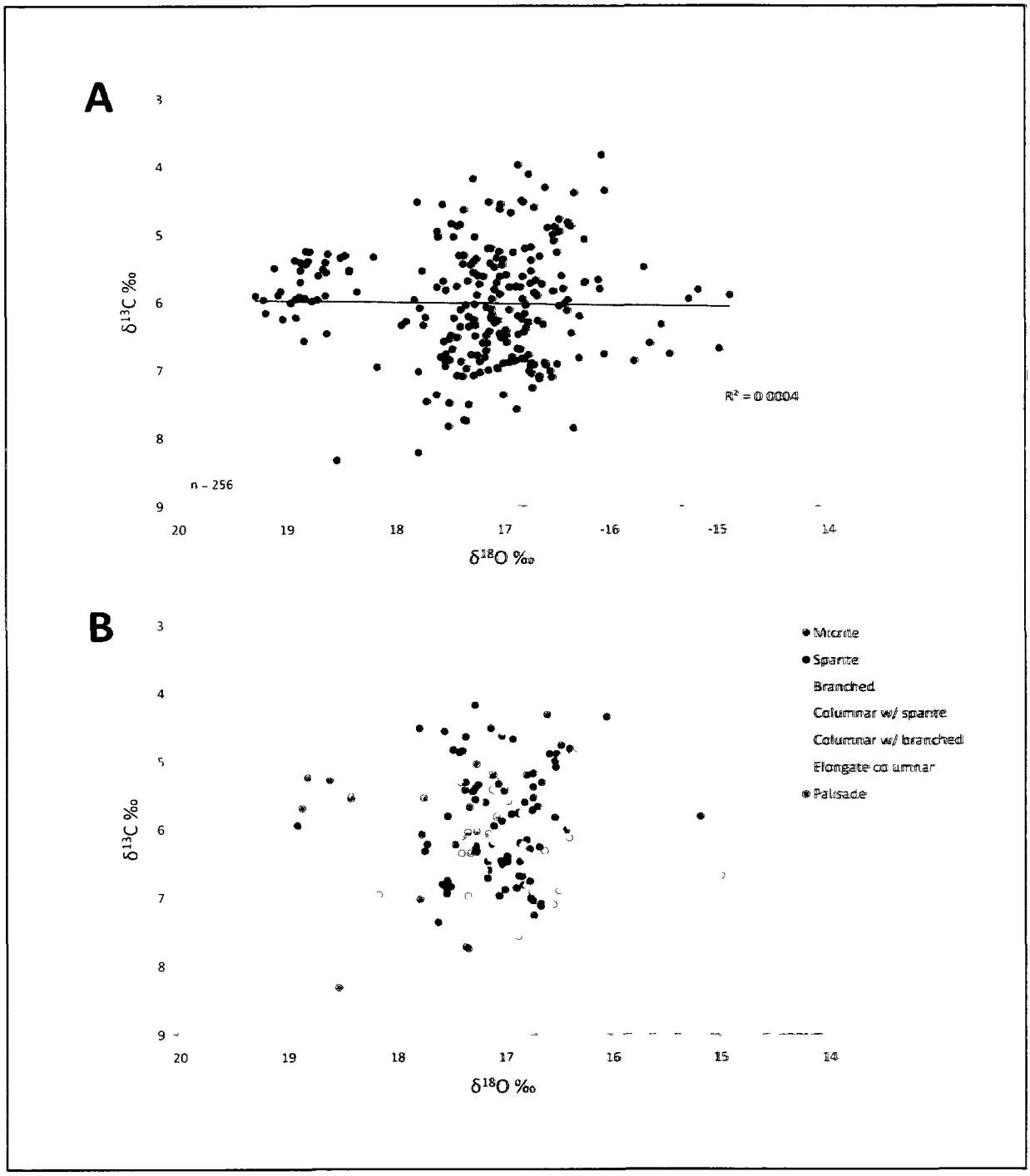

Figure 4.12. Relationship between $\delta^{13}C$ & $\delta^{18}O$ for (A) all data points, and (B) for each individual microfabric.

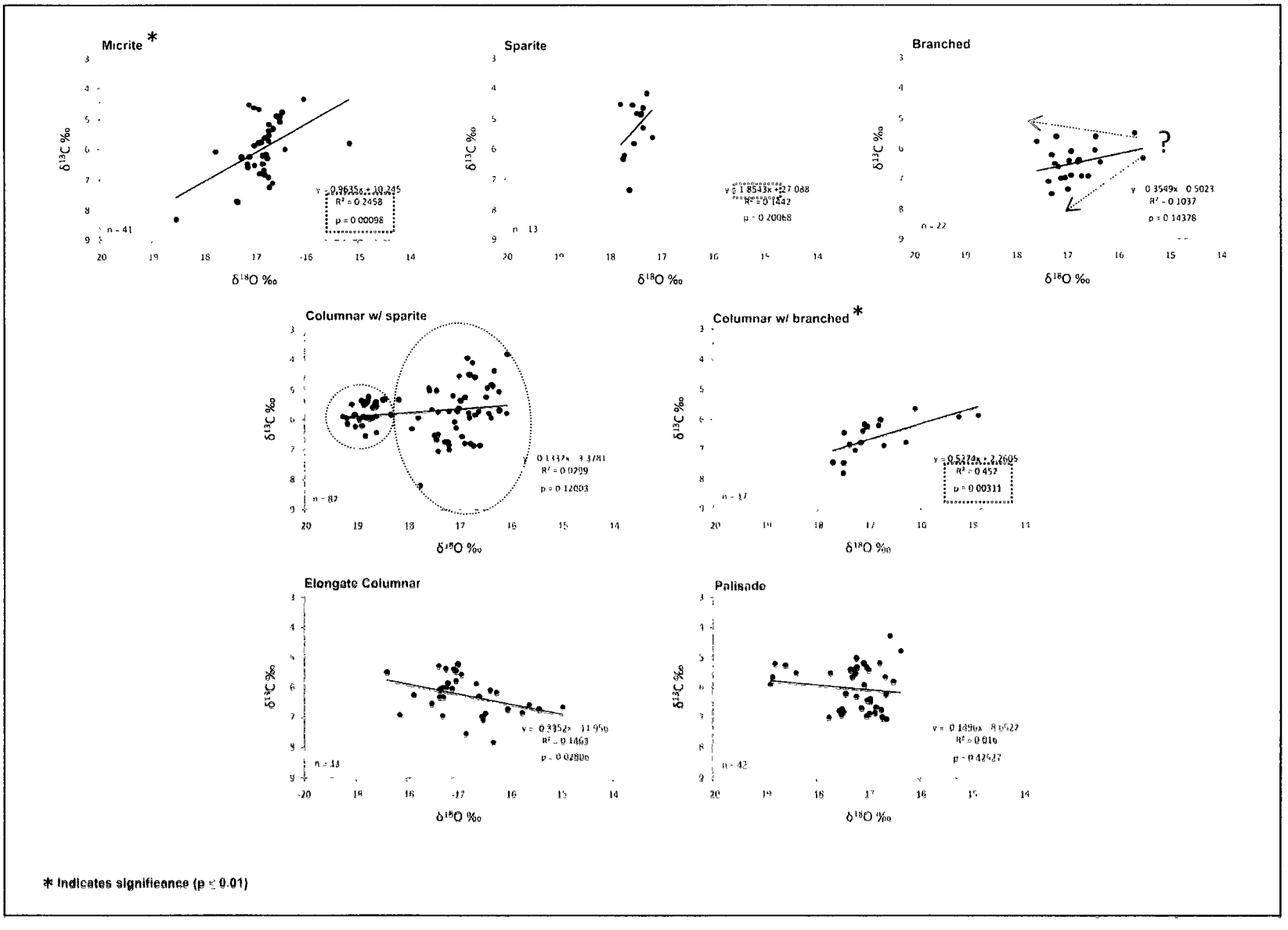

Figure 4.13. $\delta^{13}C$ & $\delta^{18}O$ relationships for each microfabric. Problematic fabrics are flagged by the dotted red lines.

Table 4.2. Slopes of $\delta^{13}C/\delta^{18}O$ for each microfabric

Microfabric	*Slope* $\delta^{13}C/\delta^{18}O$
Micrite	0.96
Sparite	1.85
Branched	0.35
Columnar-with-Sparite	0.13
Columnar-with-Branched	0.53
Elongate Columnar	-0.34
Palisade	-0 15

4.2.3. High-resolution geochemistry

As discussed previously, two different microfabrics were chosen for high-resolution geochemical analysis: the harder *Elongate Columnar* fabric (*Transect A*) and the *Columnar-with-Branched* microfabric (*Transect B*), shown in *Figure 3.1*. The latter was one of the microfabrics that were shown to be problematic from the isotopic study. Sampling was conducted along transects running parallel to the growth axis of BC1-3; both transects consist of a series of laminations that may be annual. *Transect A* consists of a series of 12 laminations, or 6 couplets (*BC1-3-A1* thorough *A12*), sampled within the *Elongate Columnar* fabric found 105-112 mm from the base of BC1-3. *Transect B* consists of a series of 10 laminations, or 5 couplets (*BC1-3-B1* through *B10*), isolated within the *Columnar-with-Branched* microfabric, 65-71 mm from the base of BC1-3. Grey-scale analysis was performed on both transects using *Image J*© to clearly delineate the laminations.

Geochemical concentrations (ppm – by weight) obtained from ICP-AES analysis as well as stable isotope concentrations ($\delta^{13}C$ & $\delta^{18}O$) obtained from the same lamina, are presented in *Table 4.4*. Within *Transect A*, lamina *A12* displayed significantly higher concentrations of Mg and Na (1096.8 ppm & 469.5 ppm respectively) than the other laminae in that transect. This could be attributable to a salt grain or detrital fragment present in the intercrystalline boundaries of the flowstone, and was therefore labelled as an outlier and omitted from analysis. Average analyte concentrations and limits of detection (LOD) at the 95% confidence level are summarized in *Table 4.3*. For determination of best lines and LOD see *Appendix II*. Three of the 10 elements selected for analysis fell below the limits of detection or were not calibrated; sulphur and manganese concentrations in the flowstone were found to be below the limit of detection (<63.8 ppm and <0.8 ppm respectively), and potassium concentrations were

uncalibrated. S, Mn and K all fell below the LOD or were uncalibrated. Al, Ba, Fe, Mg, Na, Sr and Ca were all present in the sample in concentrations well above the limits of detection. Ca concentrations are consistent with concentrations obtained from previous exploratory studies (~36%), which corroborates the accuracy of the results. Checks for machine drift were completed every 10 measurements, and are plotted in *Figure 4.14*. No significant machine drift was observed, where the maximum drift reported was 0.3 ppm, falling within the associated error. Trace elemental profiles for both transects are presented in *Figure 4.15*

Table 4.3. Average analyte concentrations and limits of detection

Analyte	Average LOD of Best lines (ppm)	Average concentration of Best lines (ppm)
Al	11 0	117 6
Ba	0 7	12 7
Fe	3 6	48 7
Mg	1 1	179 3
Na	8 7	73 2
Sr	0 5	29 0
Ca	6 1	361230 7
S	63 8	(< 63 8)
Mn	0 8	(< 0 8)
K	*uncal*	---

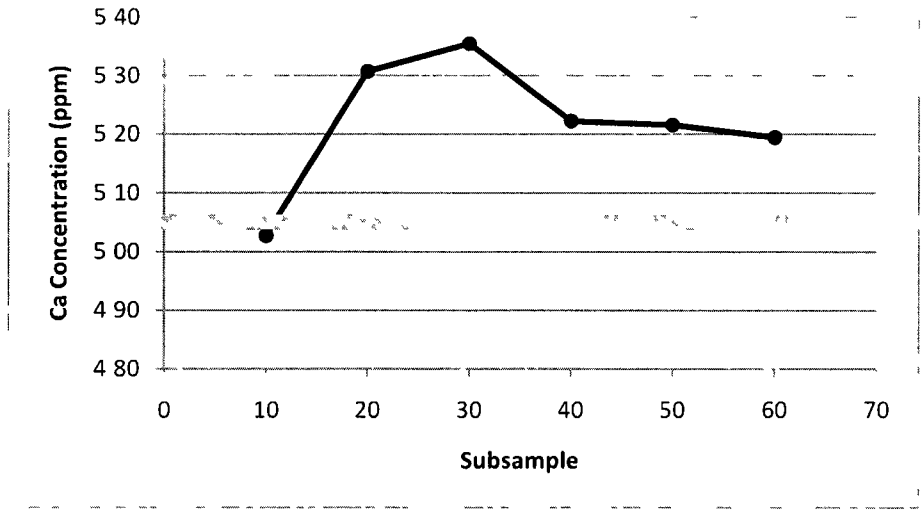

Figure 4.14. Drift check and machine reproducibility. Thick grey line represents expected (actual) concentrations, and black line represents measured values.

Table 4.4. High-resolution geochemistry results for *Transects A & B* within BC1-3

Sample ID	mm from base of BC1-3	$\delta^{13}C$ (‰)	$\delta^{18}O$ (‰)	Al (ppm)	Ba (ppm)	Fe (ppm)	Mg (ppm)	Na (ppm)	Sr (ppm)	Ca (ppm)	Mg/Ca	Sr/Ca
BC1-3-A1	105.6	-5.51	-17.59	97.1	11.8	41.1	131.7	50.5	30.5	361072	0.000365	0.000084
BC1-3-A2	106.2	-6.16	-17.41	105.2	12.8	88.5	143.5	93.5	32.5	368293	0.000390	0.000088
BC1-3-A3	106.7	-5.66	-17.07	89.4	10.2	35.5	103.7	43.6	25.5	309382	0.000335	0.000082
BC1-3-A4	107.0	-5.78	-17.19	100.9	12.3	38.2	122.0	52.1	29.5	365850	0.000333	0.000081
BC1-3-A5	107.7	-5.84	-17.43	88.1	13.8	23.9	128.0	55.4	28.2	335267	0.000382	0.000084
BC1-3-A6	108.5	-6.09	-17.38	90.2	12.0	22.2	119.5	51.6	29.8	356554	0.000335	0.000084
BC1-3-A7	109.0	-5.52	-17.38	116.5	12.8	39.1	137.5	35.5	30.3	368495	0.000373	0.000082
BC1-3-A8	109.3	-5.89	-17.26	108.9	10.1	26.5	122.7	48.4	26.5	354059	0.000347	0.000075
BC1-3-A9	109.9	-5.65	-17.13	121.1	11.9	37.8	144.6	50.9	30.1	371383	0.000389	0.000081
BC1-3-A10	110.3	-6.68	-17.22	93.4	11.9	52.1	128.3	59.8	28.8	365889	0.000351	0.000079
BC1-3-A11	110.9	-5.75	-17.07	101.5	12.5	25.7	124.9	43.5	30.2	370601	0.000337	0.000081
BC1-3-A12	111.3	-5.63	-17.07	122.5	12.2	58.0	*1096.8*	*469.5*	30.8	367872	*0.002981*	0.000084
BC1-3-B1	45.2	-5.99	-17.10	131.3	16.1	69.8	196.1	70.7	29.1	373466	0.000525	0.000078
BC1-3-B2	46.7	-5.84	-16.86	144.4	13.0	62.4	161.3	56.8	26.8	368811	0.000437	0.000073
BC1-3-B3	47.2	-5.95	-17.25	133.2	12.1	54.3	142.2	49.6	24.8	355716	0.000400	0.000070
BC1-3-B4	47.5	-5.98	-17.28	105.5	12.5	32.5	131.7	60.4	28.0	364678	0.000361	0.000077
BC1-3-B5	48.1	-6.12	-17.29	115.3	11.9	42.5	140.5	73.4	26.6	350293	0.000401	0.000076
BC1-3-B6	48.5	-5.86	-17.34	174.8	13.0	89.5	125.8	37.5	27.5	367214	0.000343	0.000075
BC1-3-B7	49.0	-5.49	-17.48	163.5	12.8	80.1	127.3	80.9	26.7	361116	0.000352	0.000074
BC1-3-B8	49.7	-6.48	-18.42	184.8	14.1	90.7	116.3	33.4	31.1	372645	0.000312	0.000083
BC1-3-B9	50.2	-6.19	-17.58	99.9	17.1	32.3	146.7	43.2	34.5	373446	0.000393	0.000092
BC1-3-B10	50.6	-6.51	-17.04	115.0	13.8	37.0	125.3	34.3	29.9	368311	0.000340	0.000081

Note: Dark (light) laminae are indicated by shaded (unshaded) cells.

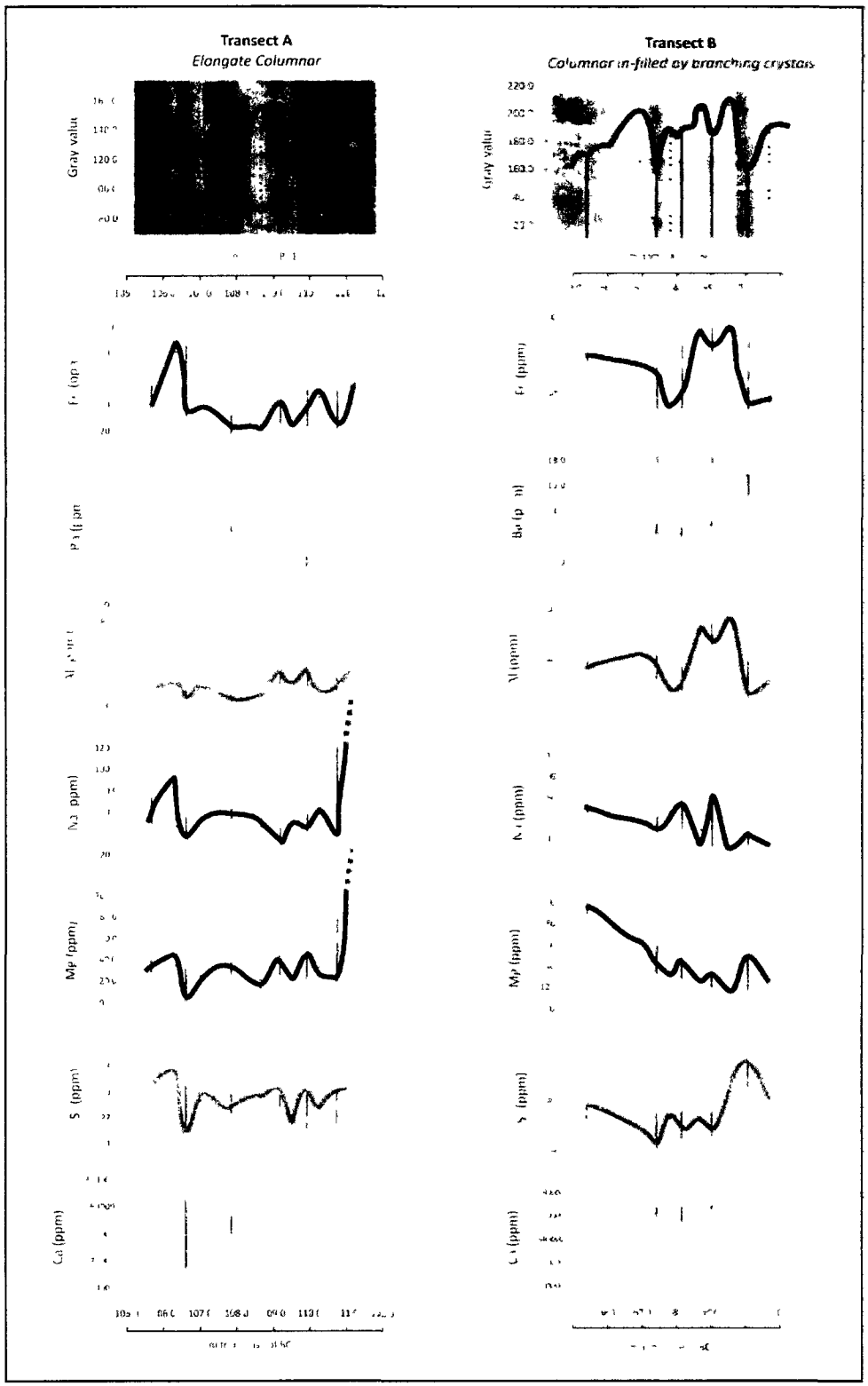

Figure 4.15. Trace elemental profiles for *Transects A* (left) and *B* (right). Dark (light) dashed lines correspond to darker (lighter) laminae. Lamina *A12* is suspect, and falls off the chart for Mg & Na.

One trend that is instantly apparent in the data is the irregularities/variability in the concentration of the elements across both transects. Some elements appear to follow a similar pattern. Fe & Al and Na & Mg all seem to have similar profiles that seem to co-vary, particularly for *Transect B*. Of the darker laminations in *Transect A*, Na concentrations appear to be reduced, and Mg concentrations appear to be increased; however the opposite trend dominates in *Transect B*. Increased Fe concentrations are generally synchronous with lighter laminae (observable in both *Transects A & B*). No clear division exists in Ba concentrations between the light and dark layers. Ca concentrations appear to have less variability within *Transect B*.

Although some elements appear to follow certain patterns, no overall definitive trend exists among the elements that illustrates increases or decreases in concentrations between lighter or darker laminae. Variations in elemental concentrations within laminations appear to be inconsistent from one profile to another. While one transect may show increases in concentrations of a certain element within darker laminations, the other transect may display an opposite tendency for the lighter laminations. Certain elements appear to be present in slightly higher concentrations within *Transect B*, namely Fe, Ba & Al, which may be attributed to the fact that lighter and more porous calcite has more fluid inclusions, which may house higher trace element concentrations.

Stable isotope $\delta^{18}O$ & $\delta^{13}C$ profiles for *Transects A & B* are shown in *Figure 4.16*. *Transect A* shows some minor variability in isotope values between laminae, most notable for $\delta^{13}C$, which may be caused by seasonal or yearly variations in the isotopic composition of meteoric waters. In general, lighter laminations show more depleted $\delta^{13}C$ values within *Transect A* suggesting a higher concentration of organic material incorporated into the crystals, likely reflective of higher organic activity in the soil above the cave while that layer was being deposited. The $\delta^{18}O$ profile in *Transect B* within the transitional calcite shows a slight decreasing trend ($m = -0.12$), with simultaneous depletion of both isotope near the white lamination at 70.0 cm from the base. Both isotopic profiles within the transitional calcite show less minor variability, where there is no clear trend of $\delta^{13}C$ depletions near lighter laminations. There was no significant relationship between $\delta^{18}O$ & $\delta^{13}C$ for *Transect A* ($R^2 = 0.0006$) however a very weak sympathetic relationship was found between $\delta^{18}O$ & $\delta^{13}C$ in *Transect B* ($R^2 = 0.1231$), presumably forced largely by one point.

Figure 4.17 looks more closely at the relationships between colour and geochemistry across both transects. Although some synchronicity between colour (grey-scale intensity) and iron concentration can be seen for both transects, the relationship is stronger between colour and organic activity ($\delta^{13}C$). In general, lighter laminations are associated with more depleted $\delta^{13}C$ (higher organic content), and in some cases higher iron concentration. Colour variations could be a combination of both iron and organic content, but is more closely linked to the latter. This relationship is not as clearly defined within the transitional calcite of *Transect B*, but is more synchronous in the harder calcite of *Transect A*.

Similar associations are found with respect to Mg/Ca & Sr/Ca ratios (*Figure 4.18*). In general, lighter laminae have lower Mg/Ca and Sr/Ca ratios (most commonly used as an indication of shorter groundwater residence times), and darker laminae have higher Mg/Ca & Sr/Ca ratios (suggestive of longer groundwater residence times; Roberts *et al.*, 1998). Again, this relationship is more ambiguous for *Transect B*, the more porous transitional calcite. The correlation between Mg/Ca ratios and grey-scale intensity as well as Sr/Ca and grey-scale intensity is stronger for *Transect A* (R^2 = 0.297 and 0.359 respectively) than it is for *Transect B* (R^2 = 0.188 and 0.016 respectively). In general, *Transect B* experiences higher Mg/Ca ratios compared to *Transect A*, which may be associated with evaporation (Hopley *et al.*, 2009).

The covariation of Mg/Ca and $\delta^{13}C$ in speleothem may be an indication of prior calcite deposition in the epikarst due to the preferential release of ^{12}C into degassed CO_2 during prior deposition (Johnson, 2006). This relationship is very weak for both transects (R^2 = 0.01 and 0.06 for *Transects A & B* respectively; not shown), which suggests that neither fabric was subject to prior precipitation.

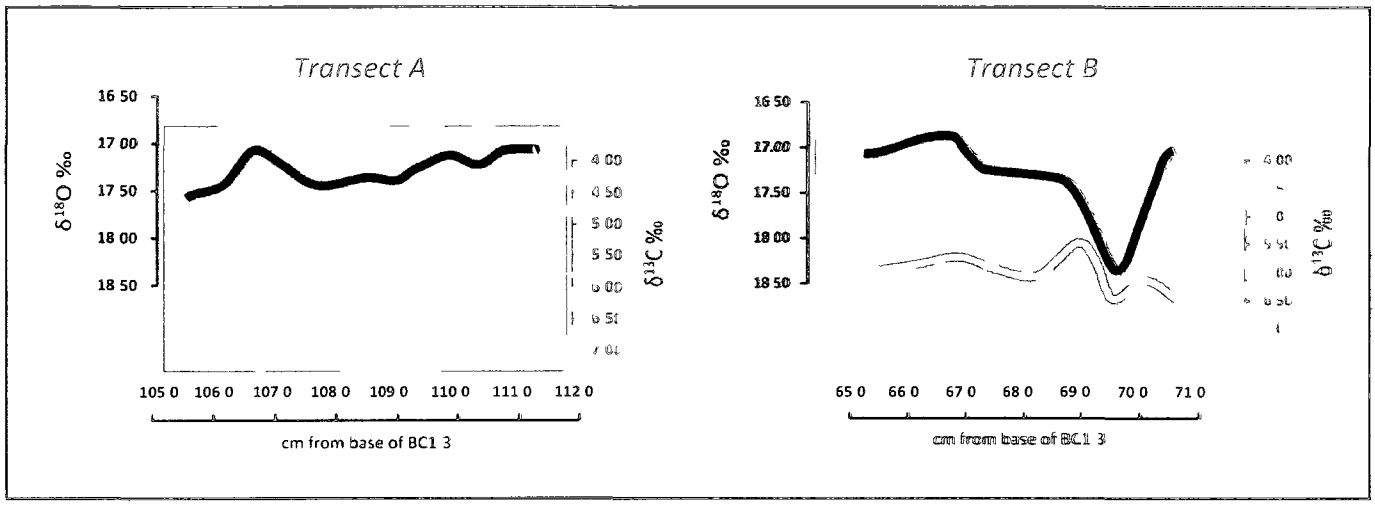

Figure 4.16 $\delta^{18}O$ (black) & $\delta^{13}C$ (grey) profiles along *Transects A* (left) and *B* (right)

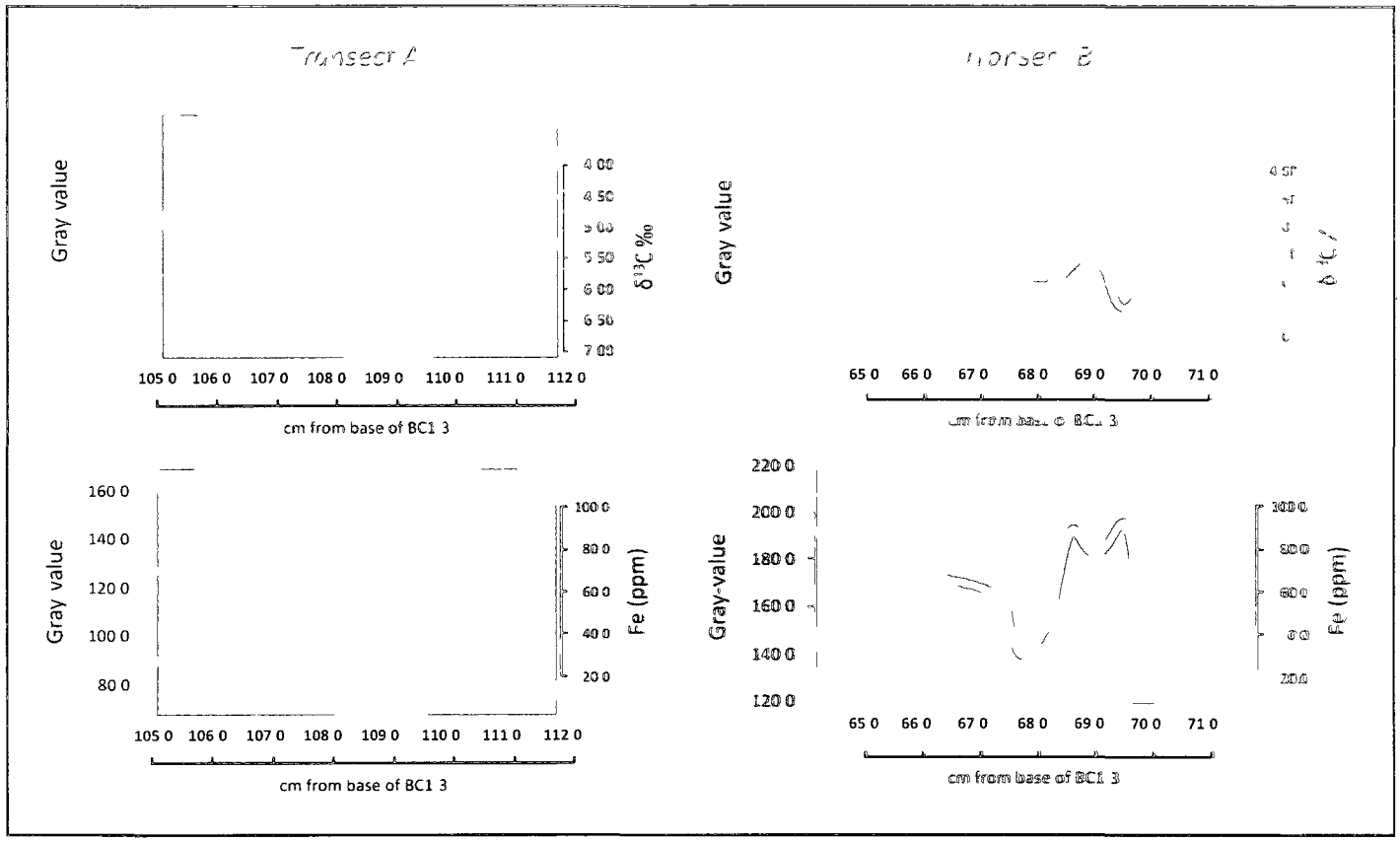

Figure 4.17 Variations in colour/grey-scale intensity (light grey), $\delta^{13}C$ (dark grey) and iron content (red) for *Transects A* (left) and *B* (right)

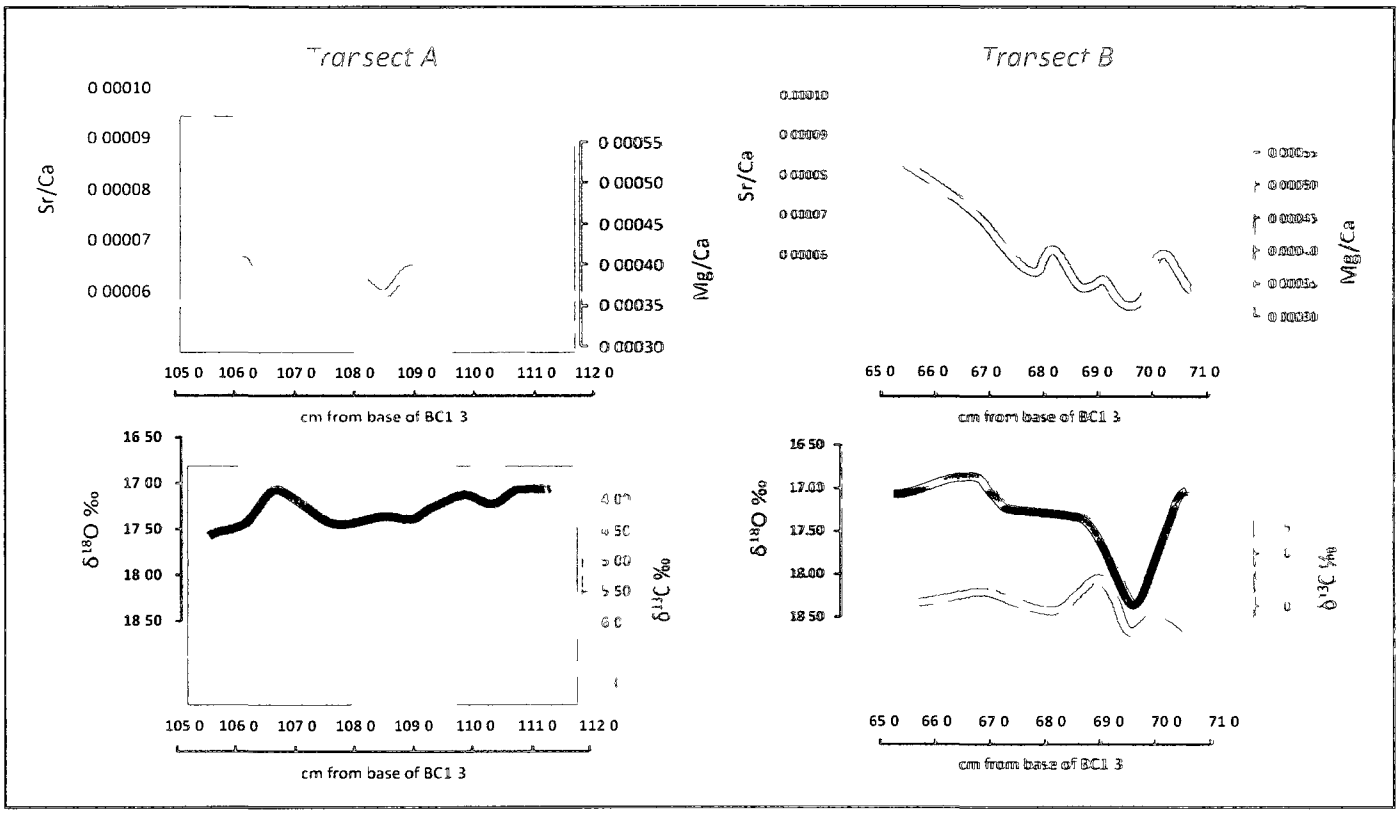

Figure 4 18 Variations in Sr/Ca (orange) and Mg/Ca (blue) for *Transects A* (left) and *B* (right)

4.2.4. Summary

- Each microfabric was found to possess slightly overlapping, yet different isotopic ranges. Fabrics within the softer grouping shared similar ranges with their transitional counterparts, where some displayed relatively short isotopic ranges.

- All of the fabrics within the softer and transitional groups displayed either weak but significant linear correlations between $\delta^{13}C$ & $\delta^{18}O$, or exhibited suspicious associations between the two isotopes, which suggests they may have been deposited under disequilibrium conditions, or subject to recrystallization.

- Results from the high-resolution geochemistry study suggest that the pore-filling mosaics may not be reliable for paleo-interpretation as they display atypical tendencies:

  (a) Concerning co-variations in $\delta^{18}O$ & $\delta^{13}C$, no significant relationship was observed in the harder calcite fabric; however a weak sympathetic relationship was discovered within the transitional calcite fabric, which may be the result of recrystallization.

  (b) Colour variations among laminations can be more closely linked to organic content ($\delta^{13}C$) than iron concentration, where lighter laminations are associated with higher organic content and in some cases higher iron concentration; however this relationship is not as clearly defined for the laminations within the transitional calcite.

  (c) The relationship of Mg/Ca to Sr/Ca to laminae couplets is more closely aligned for the harder calcite than the transitional calcite. A lack of a relationship between Mg/Ca to $\delta^{13}C$ for both profiles suggests that diagenic alteration did not take place; however higher Mg/Ca ratios may be indicative of evaporation.

4.3. Chronology building

4.3.1. Epi-fluorescence

Epi-fluorescence was explored to reveal any invisible lamination caused by varying intensities of organic material incorporated into the flowstone at the time of deposition. These annual laminations, or couplets, consisting of one light and one dark band representing one year, can be used to establish a chronology. The results from the fluorescence spectroscopy proved to be problematic as many of the acquired images possess slightly stronger fluorescent intensities towards the right of the image. This inconsistency is particularly evident when plotting the variations in fluorescence intensity along a given transect of several sequential images stitched together. It was concluded that the light source was off-center with the camera, producing a bias in the resulting fluorescent images, thus rendering a complete record of variations in fluorescent intensities along the profile of BC1 to be ineffective. Visual inspection revealed that there was a lack of continuous fluorescent banding throughout the profile of BC1. Also, there was no distinct difference between the fluorescent and visible banding; however banding was more clearly defined in the fluorescent images (*Figure 4.19*).

One factor which may have influenced the accuracy of the results is the effect of bleaching. The longer a sample is exposed to the fluorescent source, the more the sample becomes 'bleached', which effectively decreases the fluorescence intensity of the organic material in the sample. Efforts were made to reduce exposure times by leaving the shutter closed between acquiring images; however this was hard to monitor on a consistent basis to ensure uniform exposure times across the entire sample; therefore sample bleaching may be an additional source of error for the epi-fluorescence results.

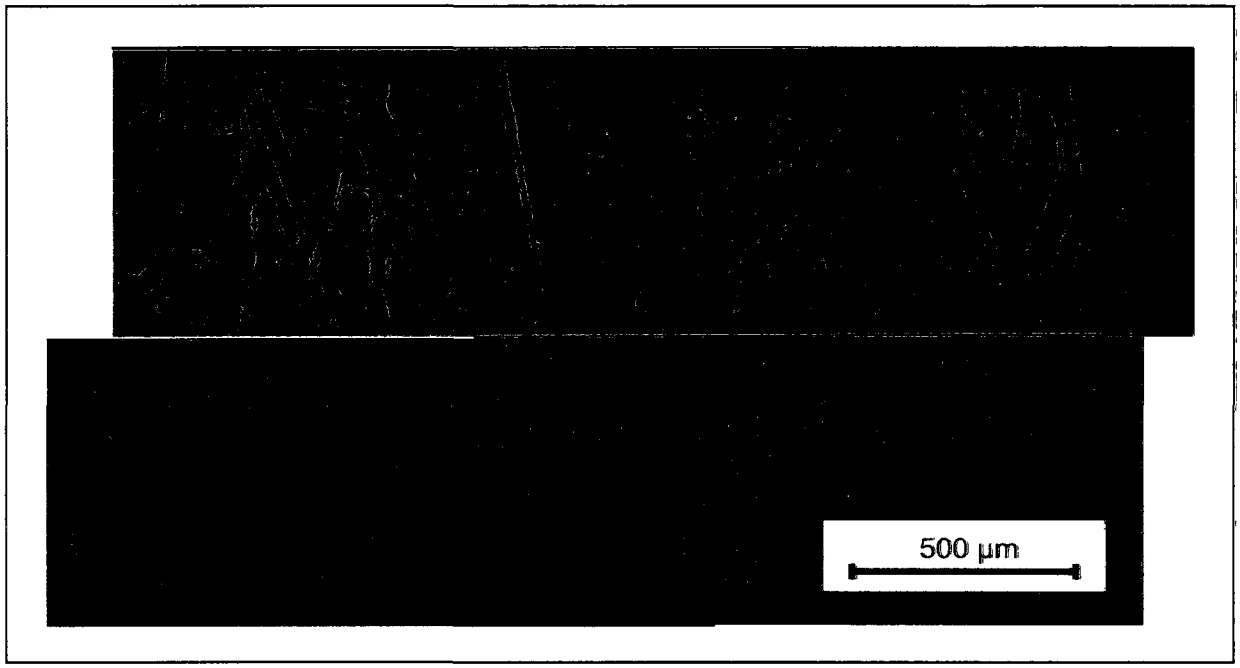

Figure 4.19. Transmitted (top) and fluorescent (bottom) light images from top portion of BC1-3.

Some small sections within BC1-3 displayed the most prominent fluorescent banding; these laminations, presumed to be annual, were used to establish a rough idea of the growth rate (*Figure 4.20*). Three rectangular sampling areas were selected, and greyscale intensities were measured in transects running parallel to the growth axis using *Image J*©. Peak intensity values were detrended by removing the slope to eliminate any bias from the light source. Laminae thickness was then determined by measuring the distance between peak intensities, representing one year of growth. The results yielded an average accretion rate of ~24 µm/yr, which is consistent with other rates of deposition for flowstones in the United Kingdom (Baker & Smart, 1995; White, 2007, p.150). The increase in fluorescence caused by higher organic matter content in this section of BC1 is likely associated with warmer and wetter environments, therefore this is most likely an overestimation of the average rate of calcite deposition for the BC1 flowstone. In reality, this rate would vary in time in response to fluctuating climatic and environmental conditions.

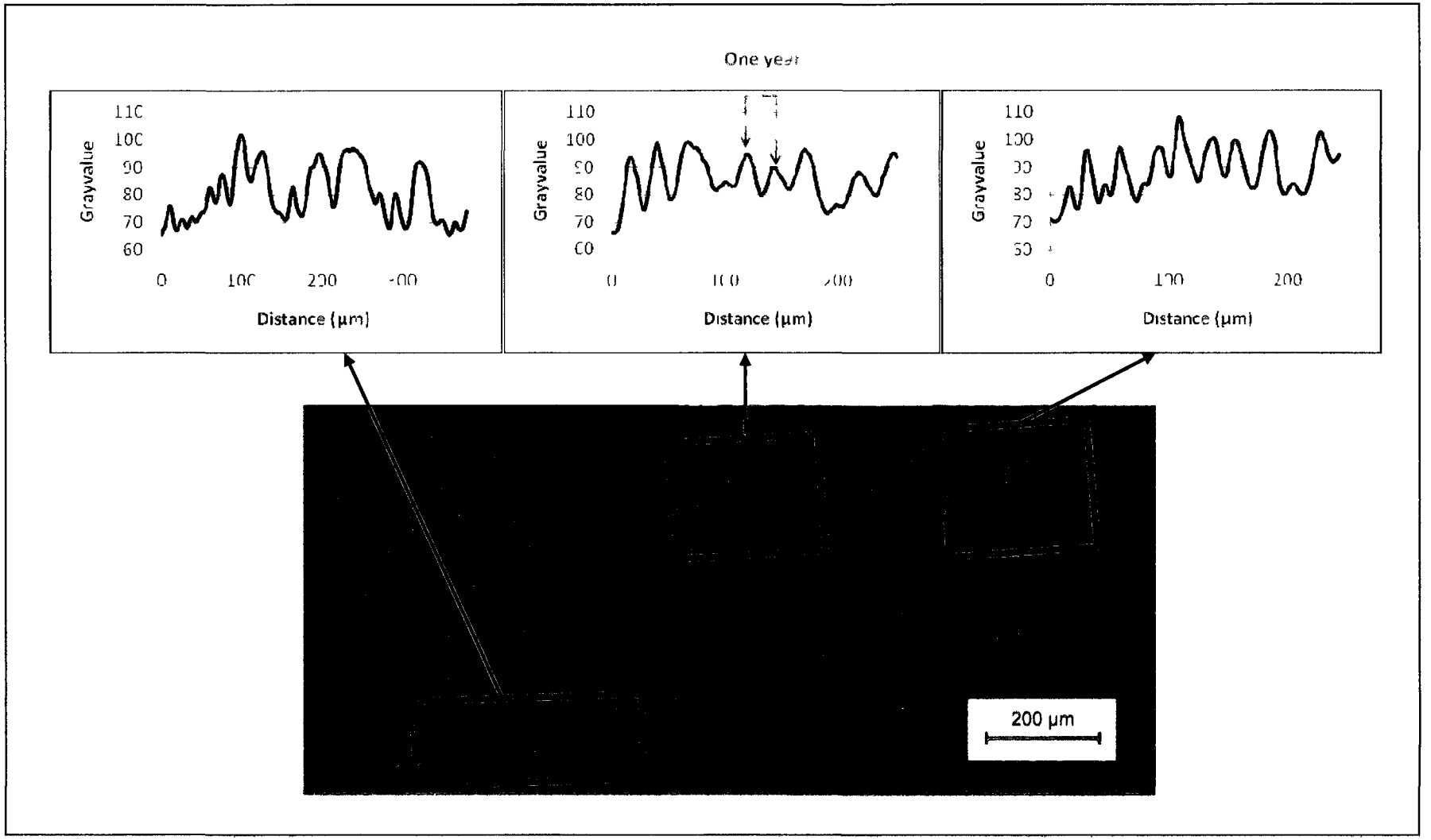

Figure 4.20. Determination of lamination thickness using *Image J*®.

4.3.2. Paleomagnetism

Paleomagnetic analysis completed by Morris & Pozzi (*see Section 3.3.2*) revealed that the BC1 flowstone was deposited over a time period that included at least two reversed polarity subchrons and up to three normal subchrons (*Figure 4.21*). This is significant as there are no other speleothems that have documented two reversed subchrons.

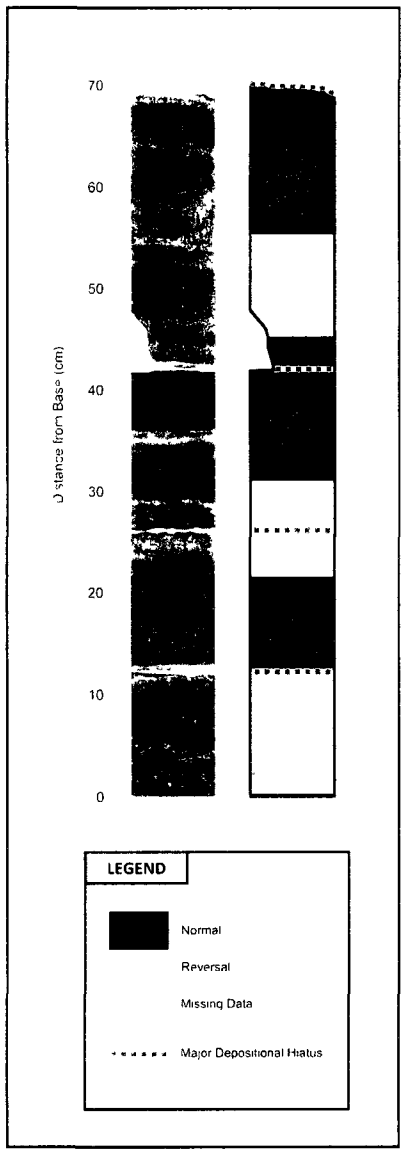

Figure 4.21. Paleomagnetic inversions of the BC1 flowstone.

4.3.3. Radiogenic He-dating

He^4 gas concentrations of the cored sample ($BC1\text{-}3_{Base}$) and individual crystal separates ($BC1\text{-}4_{Base}$) was successfully measured at the MAPL Noble Gas Laboratory in the Department of Earth Sciences at the University of Ottawa. He^4 concentrations are presented in *Tables 4.5 & 4.6* as ccSTP. It was observed from the experimental procedure that there was no significant loss of helium in ambient conditions (*Figure 4.22*). Release of He^4 gas was also insignificant at 300°C compared to that at 500°C. This suggests that the crystals are fairly retentive of radiogenic He^4, and experienced little to no diffusion of He, which is an ideal situation for radiogenic He-dating.

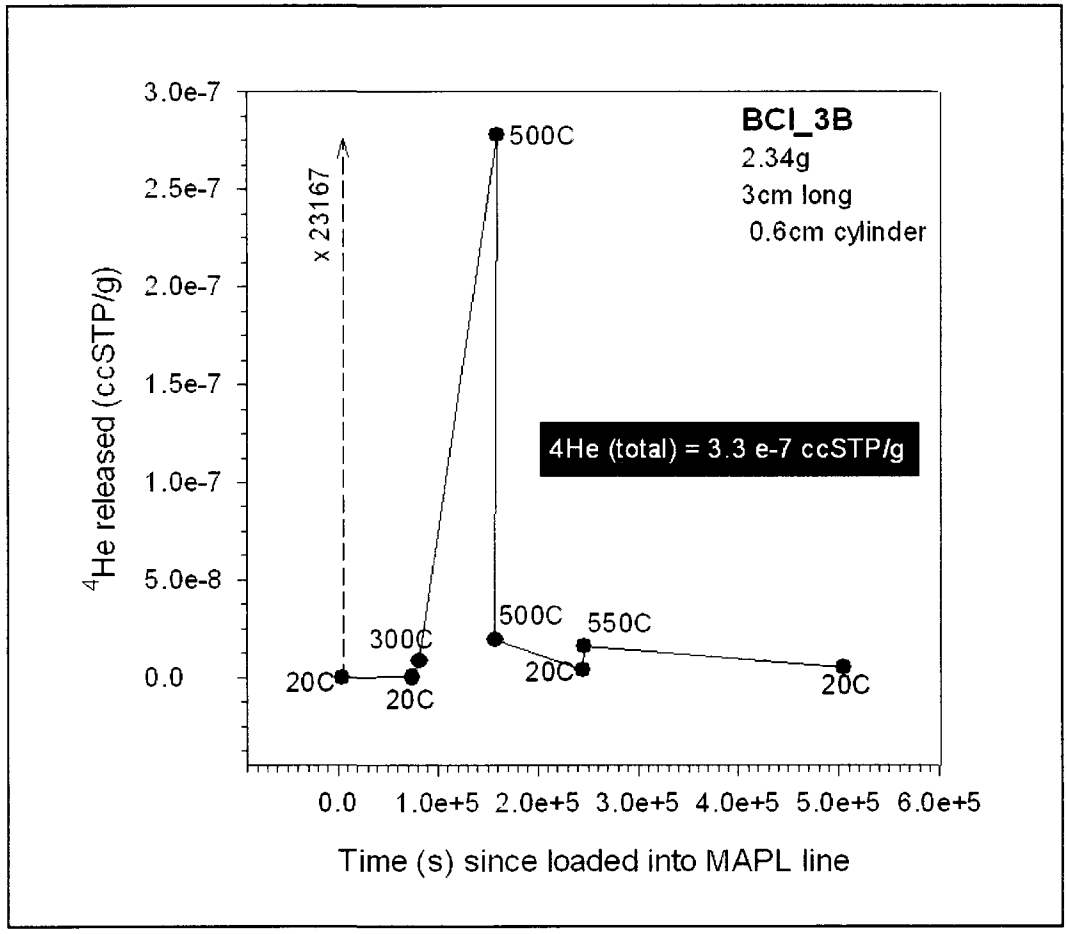

Figure 4.22. Step-wise heating extraction of He^4 gas from BC1-3B at the MAPL Noble Gas Laboratory, University of Ottawa showing minimal He loss at ambient temperatures.

Following He-extraction, U and Th concentrations were measured from the residual material on an HP 4500 ICP-MS at the University of Ottawa. U concentrations (*Tables 4.5 & 4 6*) were present well above the level of detection (LOD, 0.0036); unfortunately, Th concentrations were unable to be resolved as they fell below the LOD (0.0078 ppm). Samples were also run on a PE ELAN ICP-MS, returning similar U values; yet Th still fell below the LOD. Several attempts were made to lower the LOD, including pre-concentration procedures and crude chelating resins; however this proved to be unfeasible, related in part to the inherently high Ca concentrations. One thing we know for certain is that Th levels are either present in the sample at or below the LOD (0.0078 ppm), or not present at all (i.e. = Ø); therefore both scenarios can be employed to provide an age bracket estimate for each of the samples. *Table 4.5* summarizes the age calculations for both samples using the upper limits of Th (i e. LOD), where *Table 4 6* provides an age estimate using the lower limits of Th (i.e. = Ø) for both samples. He^4 concentrations were converted to He^4 atoms g^{-1} yr^{-1} using *Equation 5*, and ages were calculated using *Equation 6* for both Th scenarios. Ages were found to be in stratigraphic concordance with the BC1 profile, and late-Tertiary in age, falling between 9.66-9.73 ± 0.83 Ma (2σ) for $BC1\text{-}3_{Base}$, and 9.35-9.44 ± 0.52 Ma (2σ) for $BC1\text{-}4_{Base}$ (*Figure 4.23*).

A relative growth rate was estimated for block BC1-4 using the dates from $BC1\text{-}4_{Base}$ (using the LOD estimate) and $BC1\text{-}4_{Top}$ from Germany (*Figure 4.23*). Approximately 16 cm separates $BC1\text{-}4_{Top}$ and $BC1\text{-}4_{Base}$, which is distinguished by a ~6.12 Ma age gap. This translates to an abnormally slow growth rate of approximately 0.03 µm yr^{-1}, adding uncertainty to the younger date.

Table 4.5. Radiogenic He-dating results with minimum ages for BC1 using Th = LOD

Sample No	He^4 (ccSTP)	U (ppm)	Th (ppm)	He^4 atoms g^{-1} yr^{-1} [φ]	Minimum Age (Ma) [α]
$BC1\text{-}4_{Base}$	2 209 x 10^7 (± 1 1 x 10^8)	0 194 (± 0 0045)	0 0078	6 350 x 10^5 (± 1 58 x 10^4)	9 35 (± 0 52)
$BC1\text{-}3_{Base}$	3 181 x 10^7 (± 2 6 x 10^8)	0 271 (± 0 0073)	(0 0078)	8 847 x 10^5 (± 2 44 x 10^4)	9 66 (± 0 83)

[φ] Using *Equation 5* (*see Section 1 5*) with Th = LOD
[α] Using *Equation 6* (*see Section 1 5*)

Table 4.6. Radiogenic He-dating results with maximum ages for BC1 using Th = Ø

Sample No	He^4 (ccSTP)	U (ppm)	Th (ppm)	He^4 atoms g^{-1} yr^{-1} [φ]	Maximum Age (Ma) [β]
BC1 4_{Base}	2 209 x 10^7 (± 1 1 x 10^8)	0 194 (± 0 0045)	0	6 290 x 10^5 (± 1 58 x 10^4)	9 44 (± 0 52)
BC1 3_{Base}	3 181 x 10^7 (± 2 6 x 10^8)	0 271 (± 0 0073)	(+ 0 0078)	8 786 x 10^5 (± 2 44 x 10^4)	9 73 (± 0 83)

[φ] Using *Equation 5* (*see Section 1 5*) with Th = Ø
[β] Using *Equation 6* (*see Section 1 5*)

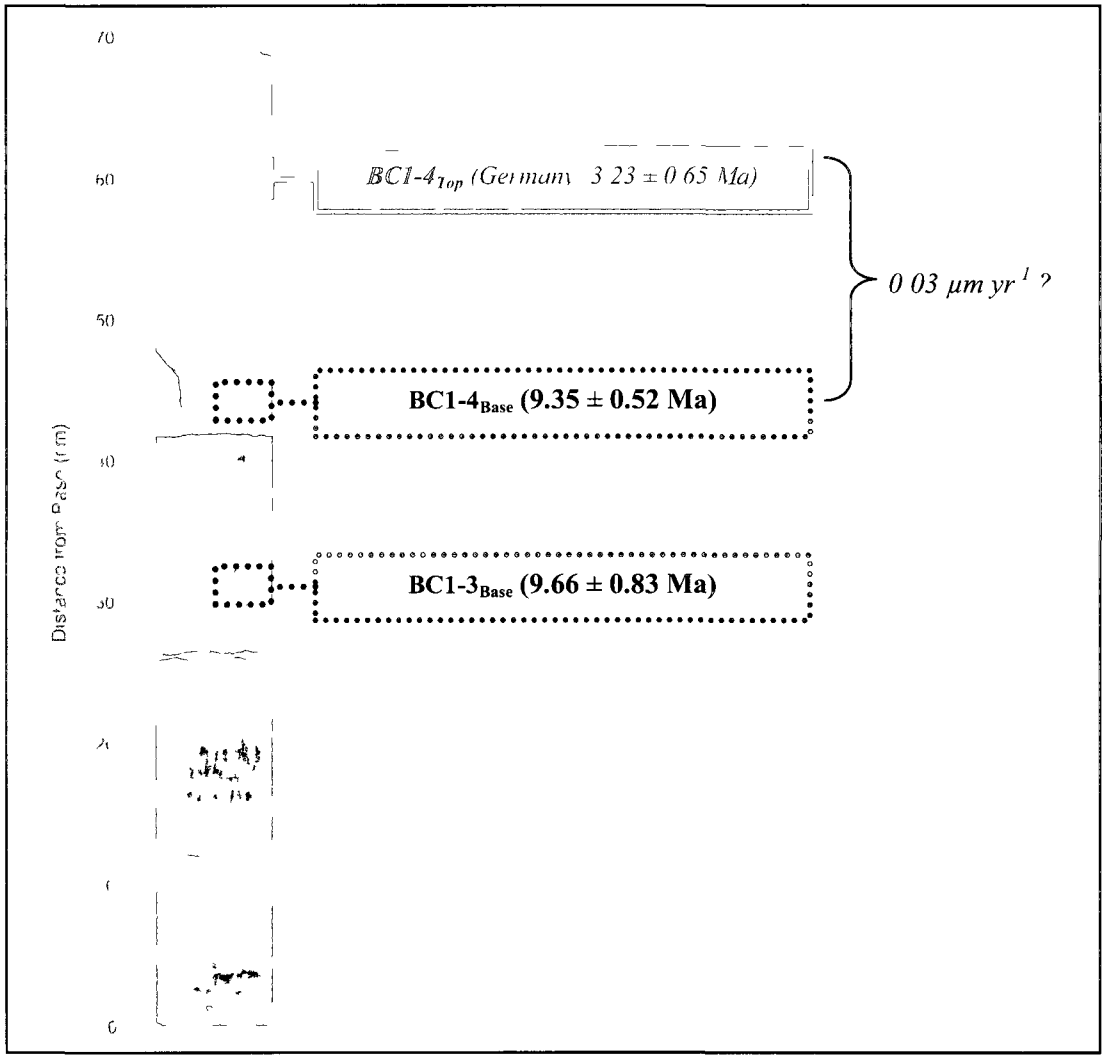

Figure 4.23. He-dating results for BC1 (2σ). Locations indicated by dashed lines were obtained at the uOttawa MAPL Noble Gas laboratory and indicate estimated ages using approximated Th values (i.e. = LOD).

4.3.4. Summary

- It was not only found that there was a lack of continuous fluorescent banding throughout BC1, but also that there was no distinct difference between the visible and invisible laminae. Small sections within BC1-3 that displayed the most prominent fluorescent banding were used to get an approximation about the growth rate, and this was estimated to be ~24 μm/yr, which is consistent with other flowstone accretion rates.

- Paleoclimatic analysis revealed at least two reversed subchrons in the BC1 flowstone, the most ever documented in a speleothem.

- He^4 gas and total U concentrations from two samples were successfully measured at the University of Ottawa, where minimal He loss at ambient temperatures suggests that the calcite grains within the harder fabrics are retentive of He. Th concentrations could not be measured on these samples as they fell below the LOD; however this information was used to obtain an age bracket for these two samples, and revealed concordant ages between 9.66-9.73 ± 0.83 Ma near the base of BC1-3, and between 9.35-9.44 ± 0.52 Ma near the base of BC1-4. Relative growth rates within block BC1-4 were estimated by comparing these values to the one obtained in Germany, disclosing an unusually slow growth rate of ~0.03 μm yr^{-1}, adding suspicion to the younger date from Germany.

5. DISCUSSION & INTERPRETATION

This chapter will assimilate the three main objectives of this thesis: to (1) assess the paleoclimatic suitability of the BC1 flowstone, providing evidence for disequilibrium conditions and/or modification by or resistance to post-depositional diagenesis; (2) retrace the depositional history at Bear Cave and environmental conditions of formation for each of the microfabrics found throughout the flowstone; and (3) refine the age estimates for the BC1 flowstone using geomorphological insight and paleomagnetic stratigraphic comparisons, as well as address the issues surrounding dating ancient speleothem.

5.1. Paleoclimatic suitability of the BC1 flowstone

In this study, the combination of previous literature, petrographic characteristics, and geochemical signatures of each individual microfabric is utilized to examine their paleoclimatic suitability. Microfabrics are rejected where they provide evidence for modification, either by recrystallization or post-depositional diagenesis, as well as indications of disequilibrium conditions; or they are accepted as reliable fabrics where they display resistance to post-depositional diagenesis, and do not exhibit disequilibrium tendencies. *Table 5.2.* summarizes the criteria for paleoclimatic suitability for each individual microfabric.

5.1.1. Evidence for disequilibrium conditions, recrystallization and diagenesis

The combined results from the crystallographic and geochemical studies indicate that some microfabrics may have been subject to modification (recrystallization and diagenesis) or disequilibrium conditions at the time of deposition. The relationships observed from the $\delta^{18}O$/ $\delta^{13}C$ plots of each microfabric (*Figure 4.12*) can provide valuable information about the conditions at the time of deposition. The fact that the $\delta^{18}O$/ $\delta^{13}C$ data are pulled from the entire profile of BC1 (i.e. multiple layers and not one single layer) rules out the possibility that covariations of the two isotopes are attributable to small scale seasonal shifts in climate. These small scale shifts are more likely to be detected along a single growth layer at a microscopic

scale, and not along groupings of horizons along an entire profile that share similar microfabric textures. A weak, but significant positive correlation between $\delta^{18}O$ & $\delta^{13}C$ was observed for two of the microfabrics of BC1, including *Micrite* and *Columnar-with-Branched.* As noted by Hendy (1971) and Gonzalez & Lohmann (1987), the positive covariance of oxygen and carbon isotopes may be indicative of prolonged CO_2 degassing accompanied by evaporation, and is therefore indicative of non-equilibrium deposition. A subtle logarithmic trend observed on the $\delta^{13}C/\delta^{18}O$ plot for the *Columnar-with-Branched* microfabric may be symptomatic of more influence from evaporation, and less from degassing (Fantidis and Ehhalt, 1970). The positive tendencies observed in the $\delta^{13}C/\delta^{18}O$ plot for these two fabrics is fitting as microcrystalline and dendritic fabrics are associated with this phenomenon. According to Frisia *et al.* (2000) and McDermott *et al.* (1999), microcrystalline and dendritic fabrics exhibit rougher crystal surfaces and are regarded as unlikely to exhibit equilibrium isotope and trace element fractionations, and are therefore regarded as unreliable proxies for past climate changes. Studies by the same authors have also found that dendritic fabrics are common in alpine caves where air current is present, similar to that of Bear Cave, and may have formed in response to evaporation at the site of deposition. Furthermore, dendritic fabrics have also been observed to be enriched in $\delta^{18}O$ & $\delta^{13}C$ due to rapid degassing of $CaCO_3$ and evaporation in the cave atmosphere (Gonzalez & Lohmann, 1987, p.93; Frisia, 2000). Although the $\delta^{13}C/\delta^{18}O$ plot for the *Branched* microfabric from the BC1 flowstone does not display a significant linear correlation between the two isotopes, or a striking enrichment in $\delta^{18}O$ or $\delta^{13}C$, it still displays a general positive tendency, reflective of the general processes which determine this trend. A slight mushrooming effect can be observed from this plot, which may suggest that other factors are at play. The results from the Hendy Test that was performed on the *Branched* and *Columnar-with-Branched* microfabrics are inconclusive, despite the fact that dendritic-type fabrics are widely known to be associated with non-equilibrium conditions. This reaffirms the uncertainties that surround the Hendy Test, and underlines the need for a more reliable approach to identifying rogue microfabrics.

Moreover, all of the softer (*Micrite, Sparite & Branched*) and transitional (*Columnar-with-Sparite & Columnar-with-Branched*) microfabrics displayed this positive slope tendency with respect to $\delta^{13}C/\delta^{18}O$, which may suggest that they were deposited under some form of a non-equilibrium regime. The $\delta^{13}C/\delta^{18}O$ plot for *Sparite* exhibited an exceptionally high positive slope in comparison to the other softer and transitional microfabrics ($m = 1.85$), meaning that

there was little change observed in $\delta^{18}O$ with respect to $\delta^{13}C$. This may be a consequence of recrystallization by the introduction of newer proportions oxygen from modern feedwaters. Recrystallized fabrics are likely due to the addition of water, where crystals present in the wetting front are exposed to new water thus introducing different proportions of isotopes (Frisia *et al.*, 2000). One possible explanation as to why $\delta^{13}C$ remained unchanged could be related to limited organic activity above the cave at the time this diagenic change took place, which is likely as vegetation in the region has experienced a gradual decline since the late Tertiary (Ritchie, 1987). Strengthening this assertion of recrystallization is the random orientation of the *Sparite* crystal observed from the crystallographic study, in other words, the crystals grow in all different directions. This is not the case for the primary deposition of calcite, where calcite crystals generally have only one growth direction: up. Furthermore, similar gradients from $\delta^{13}C$/ $\delta^{18}O$ correlations were observed by Hopley *et al.* (2009), where $\delta^{13}C = 1.7\delta^{18}O$, which is known to correspond to experimental and measured instances of rapid CO_2 degassing (Fantidis & Ehhalt, 1970), and may have been a consequence of the conditions of recrystallization.

The two populations that appear on the $\delta^{13}C/\delta^{18}O$ plot for the *Columnar-with-Sparite* microfabric also raise suspicion about diagenic alterations. An abrupt shift in isotope variations was observed within a thicker layer of *Columnar-with-Sparite* in BC1-2, where there is a sudden enrichment in $\delta^{18}O$, with $\delta^{13}C$ lagging not too far behind. Without an investigation of these geochemical signatures and petrographic characteristics, one may speculate that this shift may be attributable to a shift in regional climate, when in fact it is likely the result of post-depositional diagenesis. An anomalously thick layer of *Sparite*, identified to be caused by recrystallization, sits atop this layer in question, which is then truncated by a major depositional hiatus. The petrographic observations indicate that this shift in isotope ratios may be attributable to pooling dripwaters on the surface of the flowstone. This may be permitted due to the geometry of this type of speleothem, as flowstones, especially those that cover cave floors, are more likely to have pooling dripwaters. The presence of a thick layer of sparite below a major hiatus all directly above this layer in question is an indication that diagenesis was likely taking place. Because of the porous nature of *Columnar-with-Sparite*, pooling dripwaters may have infiltrated beyond the layer of *Sparite*, and between the porous crystals, possibly dissolving some of the in-filled sparite, which may explain why the upper portion of this layer in question was observed to have a lesser density of sparite in-filling between the columnar crystals. This abrupt shift in isotopes

may represent the wetting front (the extent to which the water infiltrated and dissolved pre-existing crystallites), and may not necessarily be linear across the horizontal boundary of BC1-2. Thus, the larger more enriched population is likely caused by this phenomenon.

In addition to the suspicious trends observed from the $\delta^{13}C/\delta^{18}O$ plots, post-depositional in-filling textures observed in some of the porous *Micrite* layers suggest that this fabric, as well as other porous microfabrics, were likely subject to secondary infiltration waters, resulting in secondary precipitation in previously void cavities. *Micrite* has differing inter-granular porosities (Lohmann, 1988, p.77), which may make it more susceptible to diagenic alteration. Therefore diagenesis may have manifested in the more porous microfabrics, namely the softer and transitional microfabrics, by way of secondary infiltration waters. These porous microfabrics are more sensitive to diagenic alterations, where secondary infiltration waters may have a hand in altering initial isotopic ratios and trace elemental concentrations, ultimately modifying the original climate signal. This would explain why the softer fabrics (sparite and branched) were found to in-fill the less dense columnar crystals, resulting in bi-textured microfabrics (*Columnar-with-Sparite* & *Columnar-with-Branched*). The harder columnar crystals were likely deposited first and later in-filled by the softer microfabrics. This is strengthened by the fact that both of these microfabrics have similar $\delta^{18}O$ and $\delta^{13}C$ averages and ranges to their softer counterparts, as they share similar lineage.

The geochemical signatures of the *Short Columnar* microfabric could not be studied due to the relatively low occurrence (~2%) and because of the intrinsically thin layer thickness at which it occurs, making it difficult for high-precision sampling. As a result, this microfabric would be unsuitable for paleoclimatic analysis. Also, this microfabric commonly followed growth hiatuses or softer calcite, which implies that it may be associated with non-equilibrium deposition.

The results from the high-resolution geochemistry study are slightly more ambiguous, yet still raise suspicion about the integrity of the more porous microfabrics. Typical relationships we would expect to see in speleothems are not as clear in the *Columnar-with-Branched* (more porous) microfabric as they are in the *Elongate Columnar* (more compact) microfabric. For example, the relationship between colour and Fe & organic content are not as clearly defined in the more porous transitional fabric as they are in the harder more compact microfabric.

Furthermore, sympathetic variations in Mg/Ca and Sr/Ca ratios between laminae couplets with respect to varying groundwater residence times (Roberts *et al.*, 1998) are clearly defined in the harder microfabric, and more ambiguous in the transitional microfabric. Indications about the conditions under which these microfabrics were deposited were gained from examining the Mg/Ca ratios and $\delta^{13}C$ values along both transects. A lack of synchronicity between Mg/Ca and $\delta^{13}C$ for both microfabrics suggests that neither were subject to diagenic alteration (Hopley *et al.*, 2009); however a marked increase in Mg/Ca ratios observed in the *Columnar-with-Branched* microfabric is symptomatic of evaporation and prior calcite precipitation (Hopley *et al.*, 2009), also associated with dendritic-type fabrics. This may suggest that in the case of the *Columnar-with-Branched* microfabric, the time during which it was in-filled was characterized by evaporative conditions. This would be correct as this microfabric displayed a positive covariance between $\delta^{18}O$ & $\delta^{13}C$, also indicative of evaporation.

It is for the above mentioned reasons that all the softer and transitional microfabrics should be regarded as unsuitable for paleoclimatic analysis. The criteria for dismissal are summarized in *Table 5.2.* To reiterate, *Micrite* and *Branched* microfabrics are indicative of non-equilibrium deposition, owing to kinetic fractionation effects (degassing and evaporation), where *Sparite*, *Columnar-with-Sparite* and *Columnar-with-Branched* are regarded as having been subject to post-depositional diagenesis, namely by secondary infiltration waters. Depositional conditions and processes behind the *Short Columnar* microfabric remain uncertain as they were unable to be sampled; however due to their close proximity to softer fabrics, they are likely associated with non-equilibrium deposition. Ambiguity in some of these interpretations may be explained by the possibility that not all point samples within the $\delta^{13}C/\delta^{18}O$ plots of a certain microfabric are attributable to non-equilibrium deposition, which may explain the lower r-squared values. For example, one specific layer of M*icrite* may have been deposited under equilibrium conditions. Regardless, the majority of these layers do exhibit non-equilibrium tendencies; therefore it is best to avoid them altogether. Additional uncertainty may be added on account of secondary waters infiltrating these porous textures, which may have a hand in blurring these relationships.

5.1.2. Reliable microfabrics for paleo-interpretation

Judging from the petrographic and geochemical studies, both of the harder microfabrics (*Elongate Columnar and Palisade* calcite) appear to be pristine, unaltered by diagenic modifications, and representative of equilibrium deposition. Neither of these microfabrics displayed a linear covariance between $\delta^{18}O$ & $\delta^{13}C$, suggesting that they were deposited in isotopic equilibrium with their parent drip waters (Hendy, 1971; Gonzalez & Lohmann, 1987, p.94). Additionally, of all the microfabrics, these were the only two which displayed negatively sloping trend lines from the $\delta^{13}C/\delta^{18}O$ plots, further strengthening the idea that they were not subject to disequilibrium conditions. Positively sloping associations between $\delta^{18}O$ & $\delta^{13}C$ are attributable to evaporation and degassing, therefore both of these processes can be ruled out. Hopley *et al.* (2009) have also reported negative correlations between $\delta^{18}O$ & $\delta^{13}C$ in primary calcite speleothems.

Columnar-type microfabrics are generally regarded as reliable proxies for paleoclimatic reconstruction, provided that diagenic alterations did not modify their physical and chemical parameters (Kendall & Broughton, 1978; Frisia *et al.*, 1996; Lohmann, 1987, p.77). Scanning electron micrograph images from the BC1 flowstone revealed a perfectly intact framboidal pyrite found within the intercrystalline boundaries of the *Palisade* microfabric. In petrology and mineralogy, perfectly intact framboidal pyrite is generally used to indicate either the absence of, or the very early stages of diagenesis (Park, 1967); therefore its existence implies that this microfabric may not have been subject to secondary infiltration waters which would have destroyed its structure. This resistance to post-depositional diagenesis is likely attributable to the fact that the calcite crystals of these two microfabrics are harder and more tightly-packed in comparison to the other microfabrics of BC1. As a result, secondary infiltration waters are unable to permeate the non-porous media, avoiding breaches and alteration to the crystals by later diagenesis.

Based on these distinctions, the harder calcite can be deemed representative of primary, unaltered equilibrium deposition whereas the softer and transitional calcite microfabrics are regarded as having been subject to diagenic alterations or disequilibrium deposition. *Table 5.1.* compares the average $\delta^{18}O$ & $\delta^{13}C$ values for the fabrics deposited under equilibrium (*Elongate Columnar & Palisade*) and non-equilibrium conditions (*Micrite & Branched*) as well as those subject to diagenesis (*Sparite, Columnar-with-Sparite and Columnar-with-Branched*). Compared to the reliable microfabrics, those deposited under non-equilibrium conditions have

slightly more depleted $\delta^{13}C$ and more enriched $\delta^{18}O$ values, whereas the opposite is true for the diagenic calcite. Martín-García *et al.* (2009) also reported diagenic calcite to be isotopically heavier, or more enriched in ^{13}C, than primary calcite. The overall enrichment of $\delta^{18}O$ observed from the non-equilibrium microfabrics strengthens the idea that evaporative processes were at play as evaporation tends to enrich ^{18}O due to the preferential removal of ^{16}O, with little change in $\delta^{13}C$ (Gonzalez & Lohmann, 1988, p.94).

Table 5.1. Average $\delta^{18}O$ & $\delta^{13}C$ values for reliable vs. unreliable microfabrics

Depositional Regime	***Average $\delta^{13}C$ (‰)***	***Average $\delta^{18}O$ (‰)***
Reliable microfabrics:		
Equilibrium		
-Elongate Columnar & Palisade	-6.18	-17 07
Unreliable microfabrics:		
Non-equilibrium		
-Micrite & Branched	-6 23	-16.84
Diagenic		
-Sparite, Columnar-with-Sparite & Columnar- with-Branched	-5.89	-17 31

These distinctions enable the identification of horizons that are suitable for paleoclimatic interpretations. *Figure 5.1* illustrates the extent of reliable versus unreliable calcite in terms of their paleoclimatic suitability. By eliminating all the softer and transitional microfabrics, almost 70% of the profile of BC1 is deemed unsuitable for detailed paleoclimatic analysis. All major discontinuities are bound by the diagenic or disequilibrium calcite, which has its greatest extent between BC1-2 & BC1-3. Blocks such as BC1-1 would not be practical to study as there are frequent shifts in microfabric type, which would ultimately translate into too many disruptions in the record to make any discernable interpretations. Blocks such as BC1-4 would be more practical to use for paleo-research, as it boasts thick, developed layers of harder calcite near the base. However, an increase in the sampling intervals for geochemical analysis would be necessary for any inferences to be made about climatic variability as they were only performed at 5 mm intervals in this block (compared to every 1.5 mm for BC1-2 & BC1-3). There is something to be said however about the intrinsic bias of basing an entire paleoclimatic record using only one type of microfabric, as it may have only deposited under certain conditions. This is why it is important not to disregard other fabrics altogether as they can still reveal general information about the depositional history at Bear Cave.

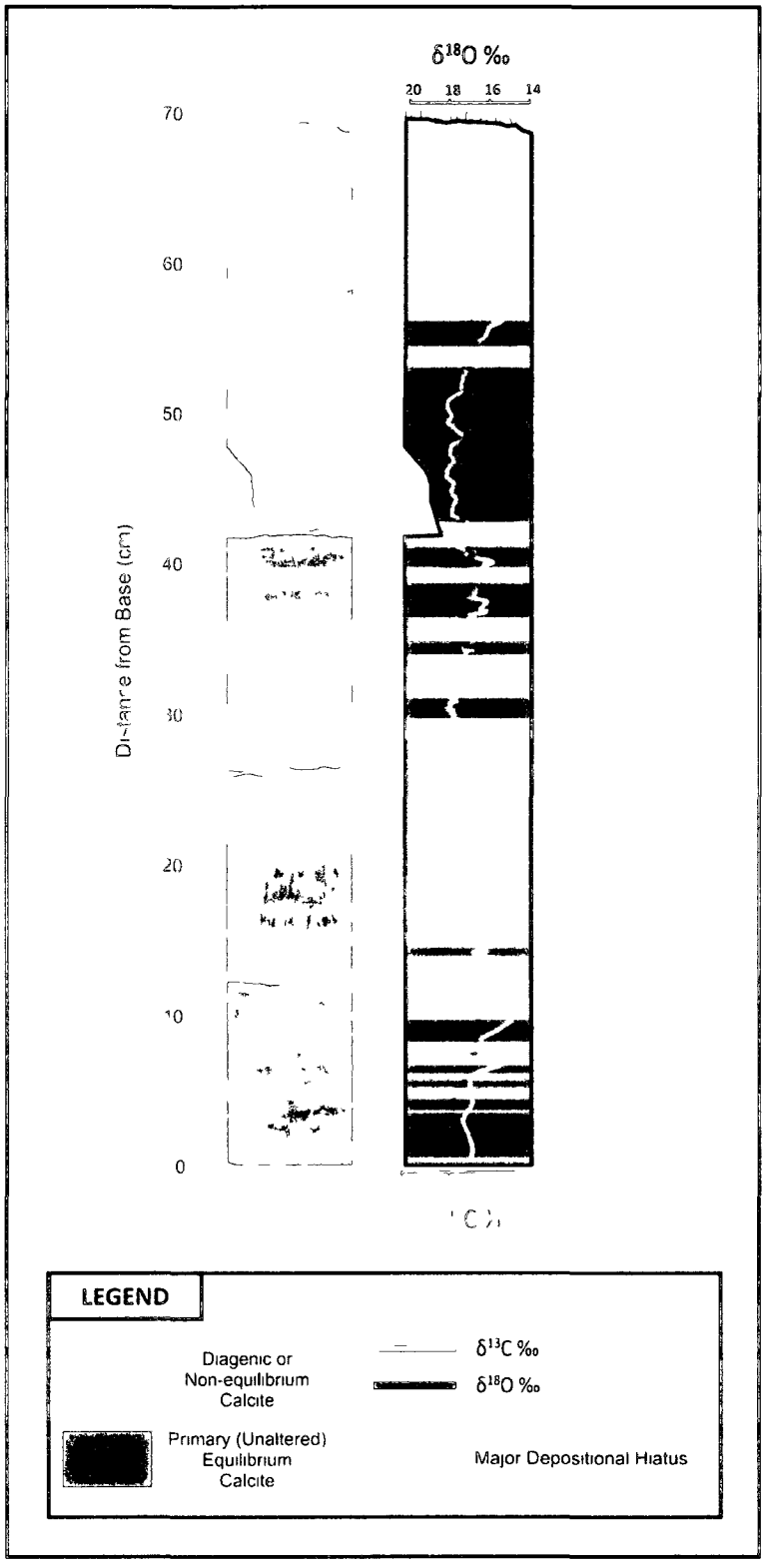

Figure 5.1. Primary/equilibrium and diagenic/non-equilibrium calcite of BC1.

Table 5.2. Paleoclimatic suitability of BC1 flowstone microfabrics

Group	Microfabric	Structure	Accept/Reject	Criteria
(I) Softer, lighter, finer, more porous microfabrics	*Micrite (microcrystalline)*		X	-Weak sympathetic relationship between $\delta^{13}C/\delta^{18}O$. -Post-depositional infilling observed in porous layers. -Typically represent growth further from equilibrium deposition (Frisia *et al.*, 2000). ***Indicative of: Non-Equilibrium Deposition***
	Sparite (Equant)	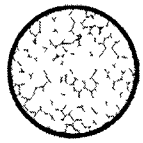	X	-Crystals have random growth orientations. - $\delta^{13}C/\delta^{18}O$ slope close to zero suggests inputs of newer proportions of O from more recent feedwaters. -large layer sits directly below major growth hiatus suggesting pooling waters and recrystallization. ***Indicative of: Diagenesis; recrystallization***
	Branched (dendritic)	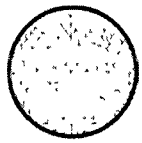	X	-Typically represent growth further from equilibrium deposition; indicative of evaporative conditions (Frisia *et al.*, 2000). -Slight mushrooming effect observed on $\delta^{13}C$ vs. $\delta^{18}O$ plot. ***Indicative of: Non-Equilibrium Deposition***
(II) Transitional microfabrics	*Short Columnar*		X	-Omitted from geochemical analysis due to relatively low occurrence. -Not ideal for analysis due to sampling difficulty because of short layer thickness. -Typically follows major growth hiatus or softer textures. ***Depositional conditions remain uncertain***
	Columnar-with-Sparite		X	-Two populations observed from $\delta^{13}C/\delta^{18}O$ plot. -Similar $\delta^{13}C$ & $\delta^{18}O$ ranges and averages to their softer counterparts. -In-filled sparite texture is likely secondary. ***Indicative of: Diagenesis (secondary in-filling)***
	Columnar-with-Branched		X	-Weak sympathetic relationship between $\delta^{13}C/\delta^{18}O$. -Similar $\delta^{13}C$ & $\delta^{18}O$ ranges and averages to their softer counterparts. -Higher Mg/Ca ratios, symptomatic of evaporation. -In-filled branching texture is likely secondary. ***Indicative of: Diagenesis (secondary in-filling of non-equilibrium crystallites)***
(III) Harder, darker, coarser, more dense microfabrics	*Elongate Columnar*	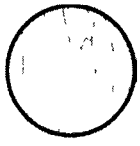	✓	-Crystals are tightly-packed. -Non-linear covariance of $\delta^{13}C/\delta^{18}O$. -Negative $\delta^{13}C/\delta^{18}O$ slope. ***Indicative of: Equilibrium deposition***
	Palisade	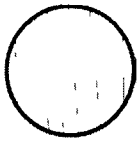	✓	-Intact framboidal pyrite found on intercrystalline boundaries. -Crystals are tightly-packed. -Non-linear covariance of $\delta^{13}C/\delta^{18}O$. -Negative $\delta^{13}C/\delta^{18}O$ slope. ***Indicative of: Equilibrium deposition***

Note: Field of view of microfabric structure is approx. 5 mm in diameter.

5.2. Interpretation of the depositional history of the BC1 flowstone

In this section, an interpretation of the depositional mechanisms and environmental conditions during the time of formation is offered for each of the eight microfabrics present throughout the BC1 flowstone, including a discussion of the paleoclimatic and paleoenvironmental history of this concretion, realized by the crystallographic and geochemical studies.

5.2.1. Crystal growth mechanisms and environmental conditions of formation

The BC1 flowstone is impressive in that it consists of several different calcite microfabrics, indicative of variable depositional conditions. A closer look at each of these microfabrics can provide evidence about the environment at the time of deposition, and the specific conditions of formation. Calcite textures in speleothems are governed by variations in drip rates and departures from equilibrium, or supersaturation levels of seepage waters (Frisia *et al.*, 2000). Therefore variations in the crystal morphology of speleothems have the potential to provide a record of supersaturation and changes in water availability (Fairchild & McMillan, 2007; Frisia *et al.*, 2000, Genty, 1992).

Microcrystalline fabrics have been observed to form at near-equilibrium conditions (low supersaturations) and less commonly at disequilibrium conditions (high supersaturations), and are associated with variable drip rates, CO_2 degassing, turbulence, and periodic inputs of calcite growth inhibitors, such as P or Mg (Frisia, 1996; Frisia *et al.*, 2000; McDermott *et al.*, 1999). These conditions lead to nucleation of calcite crystals within the feeding solution, rather than directly on the substrate surface; as a result, microcrystalline and dendritic fabrics exhibit rougher crystal surfaces with more variation in orientation which represent growth further from equilibrium isotope and trace element fractionations (Frisia *et al.*, 2000). Dendritic microfabrics also develop in disequilibrium conditions (high supersaturation) under periodic low-flow-regimes that result in prolonged CO_2 degassing and evaporation (Frisia *et al.*, 2000). In this study, both *Micrite* (microcrystalline texture) and *Branched* (dendritic texture) microfabrics displayed non-equilibrium tendencies, which are commonly linked by low and variable drip rates likely related to a reduction in the availability of drip water at the time of deposition. Therefore

the softer calcite sequences observed in the BC1 flowstone are likely indicative of slower and irregular growth brought on by colder and dryer conditions (Jo *et al.*, 2010; Frisia *et al.*, 2000).

Sparite (equant textures) typically display random orientation of grains, and are most often associated with recrystallization, as observed from the petrographic and geochemical studies in this thesis. This texture has also been observed in porous flowstones as secondary in-filling textures, where crystals may enlarge by ripening over time (Frisia *et al.*, 1996). This provides a mechanism for the formation of the in-filled transitional microfabrics, or pore-filling mosaics that are recurrent throughout the profile of the BC1 flowstone. *Columnar-with-Sparite* and *Columnar-with-Branched* microfabrics present in the BC1 flowstone are characterized by an assemblage of loosely packed roughly parallel elongate columnar calcite crystals in-filled by softer textures. These elongate columnar crystals within this microfabric can be characterized as 'acicular calcite', where there is no coalescence of crystallites (Kendall & Broughton, 1978). Kendall & Broughton (1978) suggest that changes in water flow rates can cause variations in the degree of perfection of crystallite lateral overgrowth (causing coalescence), ultimately governed by water film thickness. The shear length of these crystals implies that they were originally deposited under relatively stable hydrodynamic regimes (Turgeon & Lundberg, 2001); however the in-filling textures strongly suggests that this fabric was likely subject to later diagenic alteration by secondary infiltration waters. Therefore these textures represent a two-stage depositional process: the softer in-filling textures represent secondary changes to the flowstone by various cementation effects, and were likely deposited between the dislocated crystal boundaries after the accretion of the acicular calcite crystals, representing the original framework. Curiously, these acicular calcite crystals were only observed to be in-filled by either a sparite or branched microfabric, and not micrite, which may suggest that secondary in-filling did not occur at low supersaturations, typical of microcrystalline calcite. Rather this stage of deposition likely occurred over a period typified by infiltrating waters with higher supersaturations and evaporation (typical of dendritic fabrics) or by post-depositional in-filling by pooling dripwaters (inferred from sparitic textures).

The harder columnar-type calcite microfabrics observed from the BC1 flowstone (*Elongate Columnar* and *Palisade* calcite) have partial or complete coalescence of syntaxially overgrown crystallites, caused by slow but continuously circulating feedwater, allowing for the overgrowth on the previously formed calcite surface (Kendall & Broughton, 1978). This type of growth causes competition between growing calcite crystals, which may explain the differences

in jagged versus parallel crystal boundaries observed from the two columnar-type fabrics (Frisia *et al.*, 2000). In any case, this near-complete coalescence results in low-porosity textures that are more resistant to later diagenesis (Meyer, 2009), as observed in this thesis. Columnar fabrics also form at near-equilibrium conditions (low and consistent supersaturations) from constant drip waters that lack impurities, and generally grow when speleothems are continuously wet; therefore the harder sequences observed in the BC1 flowstone are likely characteristic of warmer and wetter periods.

Many depositional hiatuses were widespread throughout the flowstone. Hiatuses can be caused by either i) extreme low moisture conditions, unfavourable for speleothem growth, causing a drying of the surface of the speleothem, or ii) by a change in flow direction or intensity where the hiatus is often associated with dissolution of pre-existing calcite crystals (Fairchild & McMillan, 2007). The minor hiatuses observed within the softer sequences are likely credited the former, whereas hiatuses observed within the transitional and harder sequences are probably attributed to the latter, likely representative of smaller-scale fluctuations, such as increased seasonality or shifts in groundwater routing and drip source. Major hiatuses were those that bridged shifts in microfabric type or represented breaks in the growth sequence by discontinuities, and were often observed between the boundaries of the harder and softer calcite sequences, where these facies represent a significant shift in water supply induced by larger-scale (spatial and temporal) shifts in environmental or climatic conditions in the area which influence speleothem deposition. These major breaks in deposition, notably the four major discontinuities are likely associated with interruptions in the water supply related to increased aridity, or in the case of Bear Cave, frozen ground (White, 2007, pg. 142).

Short-Columnar fabrics were often observed to follow hiatuses, which is likely representative of a return to near-equilibrium conditions, and the re-establishment of nucleation surfaces by a competitive growth phase. These 'length-slow' calcite fabrics, which typically appear after growth hiatuses, are gradually overridden by 'length-fast' calcite (i.e. *Palisade*) as the calcite grows out (Folk & Assereto, 1976; Turgeon & Lundberg, 2001), commonly observed throughout BC1. The progressive crystal growth phases, or finer fabrics evolving into progressively coarser crystal fabrics, likely represent shifts from high supersaturations and variable drip rates to more stable depositional conditions, characterized by lower supersaturations and constant drip rates.

5.2.2. Paleoclimatic and paleoenvironmental significance

The petrography and geochemical composition of flowstones are generally more variable than those of stalagmites due to the spatial variability of the supply of drip water, therefore any changes in flows paths or water-film thickness (internal processes) may mask climate-related controls (external processes) on flowstone geochemical proxies (Meyer *et al.*, 2009). Close inspection of the petrography and geochemistry of the BC1 flowstone confirms this, where simultaneous shifts in stable isotopes and calcite textures (mainly within softer and transitional sequences) may be associated with alternating flow paths, ultimately spoiling the geochemical climate proxy data. As previously noted, these studies have also shown that the softer and transitional groupings within BC1 are generally associated with disequilibrium conditions or diagenic modification, where initial depositional conditions can influence isotope fractionation, or post-depositional modification can results in the loss of primary textures and geochemistry, further obscure the original signal. Although it may be prudent to eliminate these softer fabrics as geochemical proxies as they are unreliable for detailed paleoclimatic study (*Table 5.2, Figure 5.1*), they do not necessarily need to be disregarded altogether as they can still reveal general information about the time of deposition, where minor inferences can be made about climatic conditions. Textural changes, or sequences of alternating fabrics are reflective of the climate and environment at the time of deposition, ultimately indicative of hydrologic changes (White, 2007, p.168). As formerly discussed, the softer facies within the BC1 flowstone can generally be linked to periods of low and variable flow, and are associated with slow and irregular growth; hence these zones are likely linked to colder and dryer climatic conditions. Harder facies are representative of constant and continuous flow; thus these fabrics were likely deposited under relatively warmer and wetter climatic conditions. Transitional facies can also be linked to warm and wet conditions during the initial depositional phases because of the presence of long columnar-type crystals, which must have been deposited first, and have since been modified (in-filled) resulting in bi-textural facies. With this knowledge, growth zones can be identified from the BC1 profile by examining alternating textural sequences, to offer an indication of the relative climatic and environmental conditions at the time of deposition.

Figure 5.2 illustrates the variations in softer, transitional, and harder microfabrics identified from the crystallographic study, and the relative growth phases of the BC1 flowstone. The crystallographic study has shown that the flow of water from which BC1 originated has been

considerably variable over the course the accretion of this flowstone, where some blocks exhibit frequent shifts in microfabric groupings, and others display a more consistent depositional regime. All four blocks are capped by softer microfabrics and a major depositional hiatus. A total of 8 growth phases can be identified from the BC1 flowstone displaying either warm/wet, cool/dry, or variable depositional conditions. *Growth phase I* represents the initial stages of speleothem development in Bear Cave following desiccation (*see Section 5.3.1*). This encompasses nearly all of block BC1-1, which is typified by frequent shifts in microfabric, dominated by harder columnar fabrics (warm/wet), interrupted by lesser episodes of softer layers (cool/dry) indicating variable depositional conditions. *Growth phase II* bridges between BC1-1 and BC1-2, representing a period of slow deposition under cooler and dryer prevailing conditions, abridged by a major discontinuity. *Growth phase III* is found at the lower portion of BC1-2 which sees a return to warmer and wetter conditions, until an abrupt shift to softer microfabrics implies cool and dry conditions during *Growth phase IV*, located at the top of BC1-2 and base of BC1-3. This extended period of cooler and dryer conditions was also truncated by a major discontinuity, implying such low flow that speleothem deposition halted. The upper segment of BC1-3 is characterized by variable depositional conditions, suggesting a period of irregular flow (*Growth phase V*), with a softer sequence disrupting several harder series. This is followed by a brief phase of relatively cooler and dryer conditions between blocks BC1-3 and BC1-4 (*Growth phase VI*), which again is marked by a temporary cessation in deposition. For the most part, BC1-4 is typified by a period of sustained regular flow (*Growth phase VII*), implying warmer and wetter conditions. The final phase of speleothem deposition for the BC1 flowstone (*Growth phase VIII*, top of BC1-4) is marked by a short period of cooler and dryer conditions, which may mark the initiation of permafrost in the region.

Deciphering exactly how cool/dry or warm/wet the conditions were at the time of deposition is difficult to infer from this flowstone. Detailed paleoclimatic analysis is limited due to the unreliability of the softer (representative of disequilibrium conditions) and transitional fabrics (subject to diagenic modification), which leaves the harder microfabrics as the only reliable calcite from which to interpret the geochemical data (*Figure 5.1*). The harder layers within BC1-1 are unsuitable because of low sampling resolution, and those within BC1-4 were deposited during a growth phase of variable depositional conditions and are interrupted by softer sequences, which may complicate interpretation and comparison. There is a relatively large

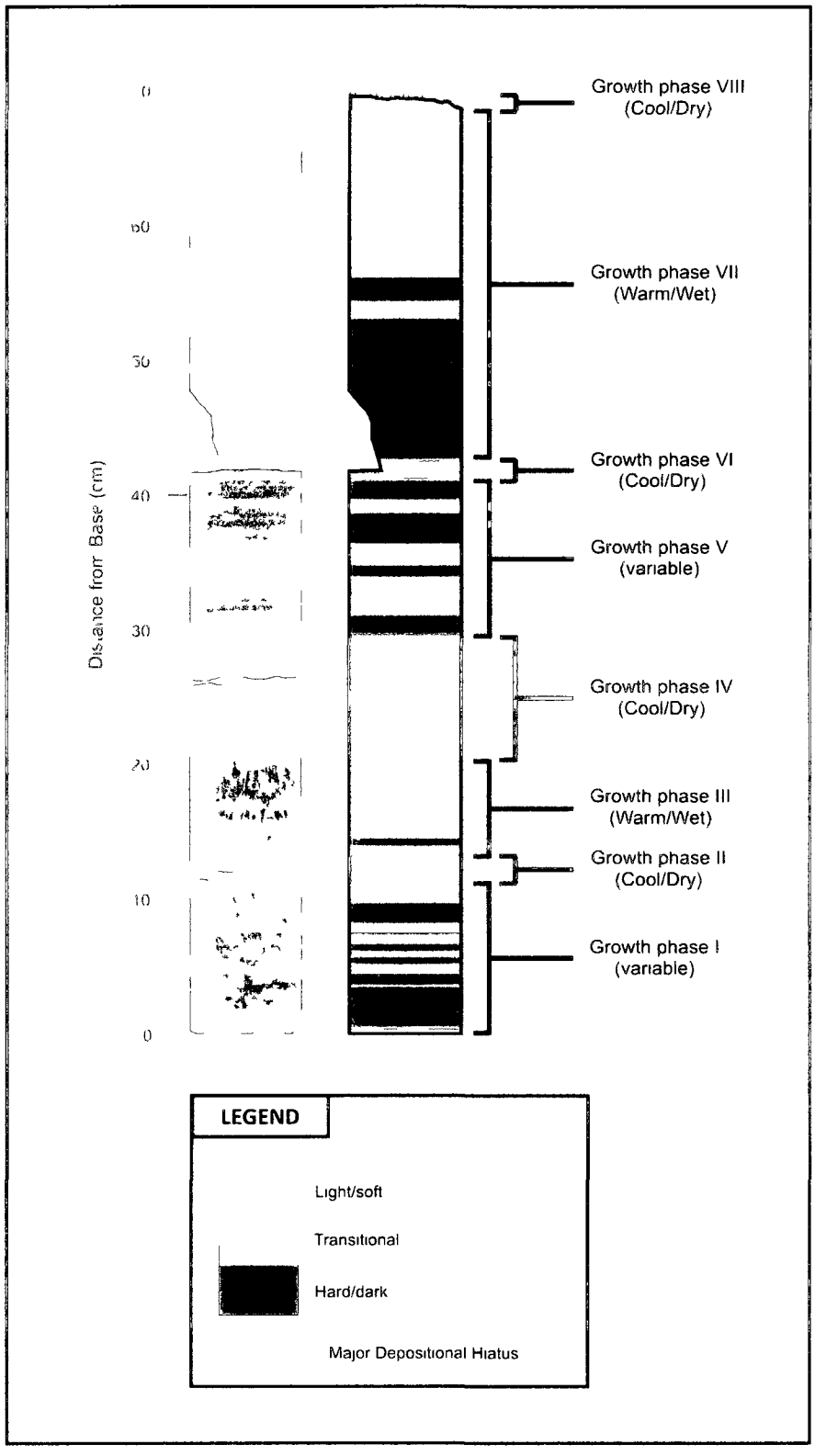

Figure 5.2. Growth phases of the BC1 flowstone.

(~10 cm) layer of palisade calcite at the base of BC1-4 (*Growth phase VII*), which would be ideal to use for detailed paleoclimatic analysis. There are currently no established proxy records for the northern Yukon during the late-Tertiary, therefore BC1 has great potential to serve as a powerful paleo-proxy for this region. Developing a detailed geochemical record of deposition for Bear Cave based solely on the hard palisade calcite may introduce an inherent bias, as these crystals are generally deposited under warmer and wetter conditions by constant flow, giving a false impression of the variation in depositional conditions. Nevertheless, exploiting these harder sequences can provide a detailed snapshot of the conditions at one point or another during deposition.

The patterns of $\delta^{18}O$ & $\delta^{13}C$ isotopes within the harder palisade layers are relatively consistent and experience no significant or abrupt variation, especially within the thick palisade layer (*Figure 5.1*), which is indicative of the thickness of water film under which they deposited (Meyer *et al.*, 2009), and suggests that these calcite crystals were deposited from one drip source. A lot of the variability that was observed over the entire BC1 profile (*Figure 4.5*) can be explained by changes in flow paths, disequilibrium conditions or post-depositional diagenesis, as the strongest variations were observed within the unreliable layers.

The mean $\delta^{18}O$ value within the harder more reliable calcite is -17.1‰ (*Table 5.1*), ranging between -18.9‰ and -15.1‰. In comparison to other geochemical studies completed on flowstones (Lauritzen, 1995; Spötl *et al.,* 2002; Holzkämper *et al.,* 2005; Drysdale *et al.*, 2006; Meyer *et al.*, 2008 and Meyer *et al.*, 2009), the relative depletion of these values leaves little doubt that BC1 was deposited under relatively cool climatic conditions (Lauriol *et al.*, 1997), but warmer than the prevailing conditions in the region today. Climate in the Northern Yukon in the late-Tertiary would have been warmer on account of a greater influence from the Pacific as the St. Elias mountain range in Alaska had not completely formed at this time. This would have permitted the circulation of warm and humid air from the Pacific towards central Yukon, resulting in a warmer climate conducive to speleothem deposition.

Similar $\delta^{18}O$ values were observed from interglacial deposits at Castleguard Cave (52° 06' N, 117° 15' W), located near the south-east margin of the Columbia ice fields in the Rocky Mountains of Alberta, approximately 2000 km south-east of Bear Cave. Harmon *et al.* (1983) reported $\delta^{18}O$ values ranging between -19.6‰ and -17.2‰ from a calcite flowstone (155-93 ka)

in Castleguard Cave, which they interpreted to reflect temperatures of approximately 0.5°C to 6°C during the time of deposition (Harmon *et al.*, 1983). The depositional conditions experienced at Castleguard Cave are likely comparable to those at Bear Cave, where the flowstone from Bear Cave likely developed under relatively warmer depositional conditions as climatic conditions in the late-Tertiary were generally warmer than during the Pleistocene interglacials.

$\delta^{13}C$ values within the harder calcite of the BC1 flowstone range between -7.9‰ and -5.3‰, which are more depleted than those of the flowstone at Castleguard Cave (-1.1‰ and +0.7‰, Harmon *et al.*, 1983), suggesting a greater organic presence at Bear Cave. However Castleguard Cave is a unique circumstance as these $\delta^{13}C$ values are not typical of $\delta^{13}C$ observed in speleothems, and is a result of bedrock dissolution, as soil CO_2 did not play a major role in the speleothem carbon content. Interpretation of speleothem $\delta^{13}C$ fluctuations can be more difficult to interpret than $\delta^{18}O$ because of the complexity associated with the controls on fractionation of carbon isotopes; therefore one can only speculate on potential associations of the $\delta^{13}C$ values from Bear Cave. The variations in $\delta^{13}C$ observed within the reliable calcite from the BC1 profile (*Figure 5.1*) may be indicative of changing proportions of C_3 (-15 to -6‰ in speleothem carbonates) and C_4 (-6‰ to +2‰) type vegetation (McDermott, 2004). Atmospheric P_{CO_2} concentrations would have been higher in the late-Tertiary, resulting in an increased photosynthetic yield amongst the C_3 plants, which have a competitive advantage over C_4 plants (Hopley *et al.*, 2007). Additionally, this increased atmospheric P_{CO_2} may have had an enriching effect in the $\delta^{13}C$ content of the BC1 flowstone as this would have introduced a greater proportion of CO_2 into the soil. One would expect $\delta^{13}C$ values in speleothem calcite to tend towards a 1:1 mixture of the host rock carbon and soil CO_2 carbon, therefore enrichment in soil CO_2 would result in a relative enrichment of $\delta^{13}C$ in calcite precipitated in caves. The gradual enrichment of $\delta^{13}C$ towards the top of BC1 may be indicative of declining organic activity in response to gradual cooling in the region.

Links between climate and paleomagnetic variations were also investigated in the BC1 flowstone, displaying no significant correlations; however interpretations were hindered by sampling uncertainties (*Appendix IV*).

5.3. Age estimates for the BC1 flowstone

Improving the chronology of the BC1 flowstones has great implications for paleoclimatic research as there are currently no established paleo-proxies in the northern Yukon during the Tertiary. The following sub-sections will include several discussion points leading to a more conclusive age estimate for the BC1 flowstone, including geomorphic and paleomagnetic interpretations to constrain the relative timeframe of deposition, and concludes with a discussion of the difficulties that are associated with dating ancient speleothems by absolute dating methods.

5.3.1. Bear Cave in relation to regional geomorphic evolution

Geomorphologists commonly call upon geomorphic interpretations to provide useful insight into the depositional history of a certain region (Sancho *et al.*, 2004); therefore with specific knowledge of the geomorphic history of the Bear Cave region, certain assumptions can be made about the relative time of deposition of the BC1 flowstone.

The limestone deposits that make up much of the region were deposited sometime during the Devonian period. Mountain building transpired over the Laramide Orogeny, which started in the late-Cretaceous and lasted approximately until the Cretaceous-Tertiary boundary (English & Johnson, 2004). After this point in time, a relatively long period of planation, or gradual levelling, would have been the dominant erosion regime during this climatically warm period in geological history.

A hydrographic network was established in the region in the early Tertiary, sometime during the mid-Eocene and pursued until the end of the Pleistocene (Duk-Rodkin & Hughes, 1994). Evidence of these paleo-waters running through the region are scarce, however paleo-terraces described by Duk-Rodkin & Hughes (1994) suggest that these ancient waters probably originated from the south, following the earliest conduits of the Porcupine River and its tributaries, eventually draining into the Beaufort Sea via McDougall Pass (Duk-Rodkin & Hughes, 1994). In addition, Lauriol *et al.* (1997) observed a number of sub-rounded sandstone and quartzite pebbles on the slopes of Bear Cave Mountain. These clasts are not glacial erratics as the furthest glacial extent is located more than 100 km to the southeast (Duk-Rodkin &

Hughes, 1994); rather, they were most likely deposited by the paleo-Fishing Branch River during a period when it traversed sandstone outcrops to the south prior to reaching the Bear Cave massif. These waters allowed for the development of a series of caves in the mountain. Bear Cave is the largest among these caves, opening at 867 m above sea level. In addition of the sandstone and quartzite pebbles, quartz, carbonate and chert pebbles were also discovered inside Bear Cave, notably in the inner chambers and at the base of BC1. These grains are usually well rounded, which implies that frost action was insignificant at the time they were deposited. SEM analysis of the BC1 flowstone revealed the presence of trace amounts of gold grains that were most likely also transported by waters originating south of the Ogilvie Mountains. Also, these waters must have been sufficient to transport pebble-sized particles in its stream load, at a then altitude of at least 867 m.

The lowest cave in altitude among this network of caves sits approximately 100 m below Bear Cave, suggesting that the karst of Bear Cave developed in a process of landscape desiccation by fluvial erosion. Thus, cave passages higher in altitude are older; as the paleo-Fishing Branch River incised into the limestone bedrock, it created newer passages and permitted the desiccation of older caves and the development of speleothems like that studied in this thesis. Down-cutting of the Porcupine River through the Richardson and Ogilvie Mountains likely occurred sometime during the late-Miocene or early-Pliocene (Duk-Rodkin & Hughes, 1994), isolating the caves above the hydrographic network, at which time it is likely that speleothems deposition began (Lauriol *et al.*, 1997). At this point, the erosional system of the Bear Cave region would have transitioned to that of a fluvial regime, giving rise to more mature relief forms. This transition came in response to cooling climatic conditions (Büdel, 1982, p.37), at the cusp of the Tertiary-Quaternary boundary, which was followed by the establishment of permafrost in the region.

As a general rule, speleothem development would have stopped before the onset of permafrost in the area. It is possible that there may have been several small episodes of speleothem growth subsequent to the appearance of permafrost (Lauriol *et al.*, 1997), but nothing comparable to what had taken place prior. According to Tarnocai & Schweger (1991) & Froese *et al.* (2008), permafrost had not been established in north-western Canada until the late-Tertiary or early Pleistocene glacial period; therefore we know the BC1 flowstone cannot be any younger than the first appearance of permafrost in the region, roughly 2-3 Ma BP. Furthermore,

speleothem formation could only have started once phreatic cave development had ceased and a vadose zone had been established, which for the case of Bear Cave likely coincided with the entrenchment of the Porcupine and Fishing Branch River valleys. Down-cutting rates for streams on bedrock channels can be estimated from the difference in elevation between the stream channel and dated terraces or caves on the valley walls (White, 2009). By adopting a bottom-up approach, we can begin with the existing landscape and use contemporary down-cutting rates (assuming the rates of these processes today are similar to those that operated in the past) to work backward to get an idea of when Bear Cave became sufficiently drained to permit speleothem deposition.

Figure 5.3. illustrates the Bear Cave massif in cross section illustrating the entrenchment of the western limb of the Fishing Branch River valley into the surrounding limestone bedrock. The summit of Bear Cave Mountain stands approximately 990m a.s.l, roughly 500m above the present day bed of the western limb of the Fishing Branch River; Bear Cave opens at 867 m a.s.l. Limestone bedrock eroded by karstic streams can see lowering rates around 10 to 800 m/Ma (Dreybrodt, 2004; White, 2009); however this depends largely on local climate, stream load, soil cover, etc, as well as regional uplift and general denudation. Tectonic uplift in the Bear Cave region since the late-Tertiary is negligible as the Laramide Orogeny ceased near the K-T boundary. Studies on the evolution of Appalachian fluviokarst estimate fluvial down-cutting rates to center around 30 m/Ma in limestone features that are also late-Tertiary in age (White, 2009). These studies also indicate that the down-cutting rate of surface streams is similar to the denudation rate of limestone uplands, ranging from 5 to 50 m/Ma. Assuming speleothems deposition followed the entrenchment of the Porcupine River, and a constant down-cutting rate of 30m/Ma, we can extrapolate to obtain an estimate of the time elapsed since speleothem deposition inside Bear Cave. This yields a date of approximately 12.6 Ma, or mid-Miocene, for the time when Bear Cave would have been isolated above the hydrographic network (*Figure 5.3*), which is in line with the estimates provided by Duk-Rodkin & Hughes (1994), as well as the ages obtained from the BC1 flowstone by radiogenic He-dating (*Figure 4.23*).

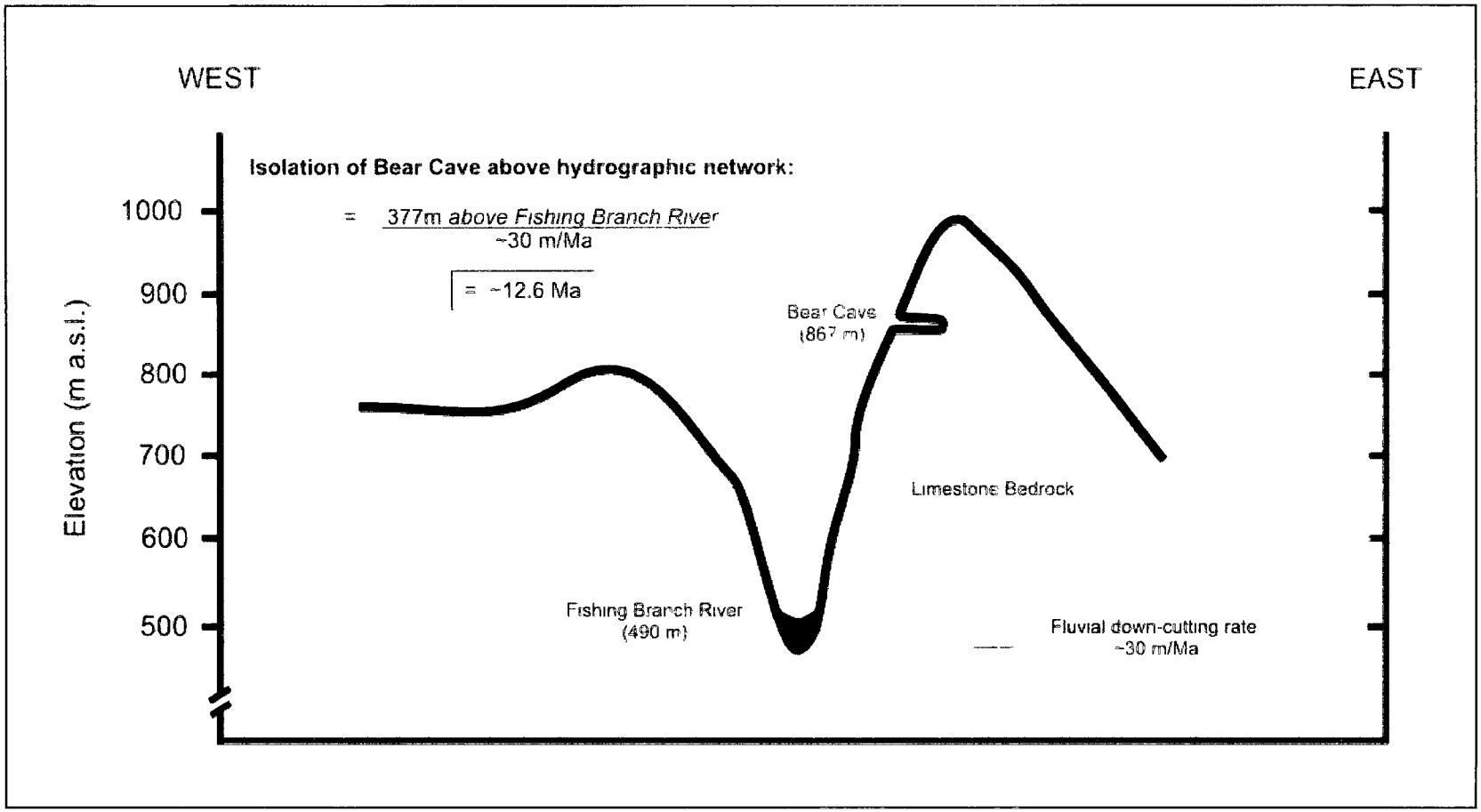

Figure 5.3. Sketch of Bear Cave Mountain in cross section depicting the incision of the western limb of the Fishing Branch River into the limestone bedrock (after Lauriol *et al.* 1997).

5.3.2. Paleomagnetic stratigraphy

Magnetostratigraphic comparisons can also be a useful tool as a form of relative dating for ancient speleothems; however it is difficult to relate this data to the known geomagnetic polarity timescale. The BC1 flowstone is a unique specimen as it contains at least two reversed polarity subchrons. With this knowledge, we can say that the base of the BC1 flowstone must be older than 1.19 Ma (Cobb Mountain normal sub-chron), as two reversed subchrons had been observed in the global geomagnetic timescale from this point history to the present day (*Figure 5.4*). However, the Cobb Mountain normal was a short lived polarity interval, and may not have been detected in the paleomagnetic record of BC1, especially with 1 cm sampling intervals. Therefore it may be more prudent to place the first reversal at the base of BC1 to 1.78 Ma, which marks the transition between the Matuyama reversal and Olduvai normal. Supporting this hypothesis is the major hiatus that intersects the second reversed interval in the BC1 flowstone, approximately 26 cm from the base of BC1, between blocks BC1-2 and BC1-3. The duration of this hiatus is unknown, and could have been long enough to exclude the Cobb Mountain normal. Conversely, the duration of any of the major hiatuses remains unknown, and may have extended long enough to exclude several polarity interval sub-chrons; however this remains unlikely due to the relatively long time span of polarity intervals in relation to speleothem deposition. Nevertheless, a conservative estimate would be to place the base of the BC1 flowstone to *at least* 1.78 Ma by magnetostratigraphic comparisons.

This comparisons raise suspicion as speleothem deposition at this point in time in Northern Yukon would have been hindered by the prevailing cold environment as it was suspected that permafrost invaded the area somewhere between 2-3 Ma. Furthermore, this time chronology leaves little room for a significant erosional phase which followed speleothem deposition, as noted by Lauriol *et al.* (1997). Therefore if we take this into account, along with the rate of entrenchment of the Fishing Branch River, it is more likely these subchrons fit somewhere beyond the Gauss or Gilbert chrons (older than 2.59 Ma); however uncertainty remains as to exactly which sub-chrons on account of variable rates of accretion and the major discontinuities, each of which represents major depositional hiatuses of an unknown duration. Pulling from the initial radiogenic He-dating results which dated the top of the flowstone to be ~3.23 Ma, the top-most normal polarity interval of BC1 is not in direct agreement with the known geomagnetic polarity timescale, which specifies a reversed interval (*Figure 5.4).* Although this adds uncertainty to this date, this disparity may however be accounted for by the relatively large error range associated with that date (~650 ka).

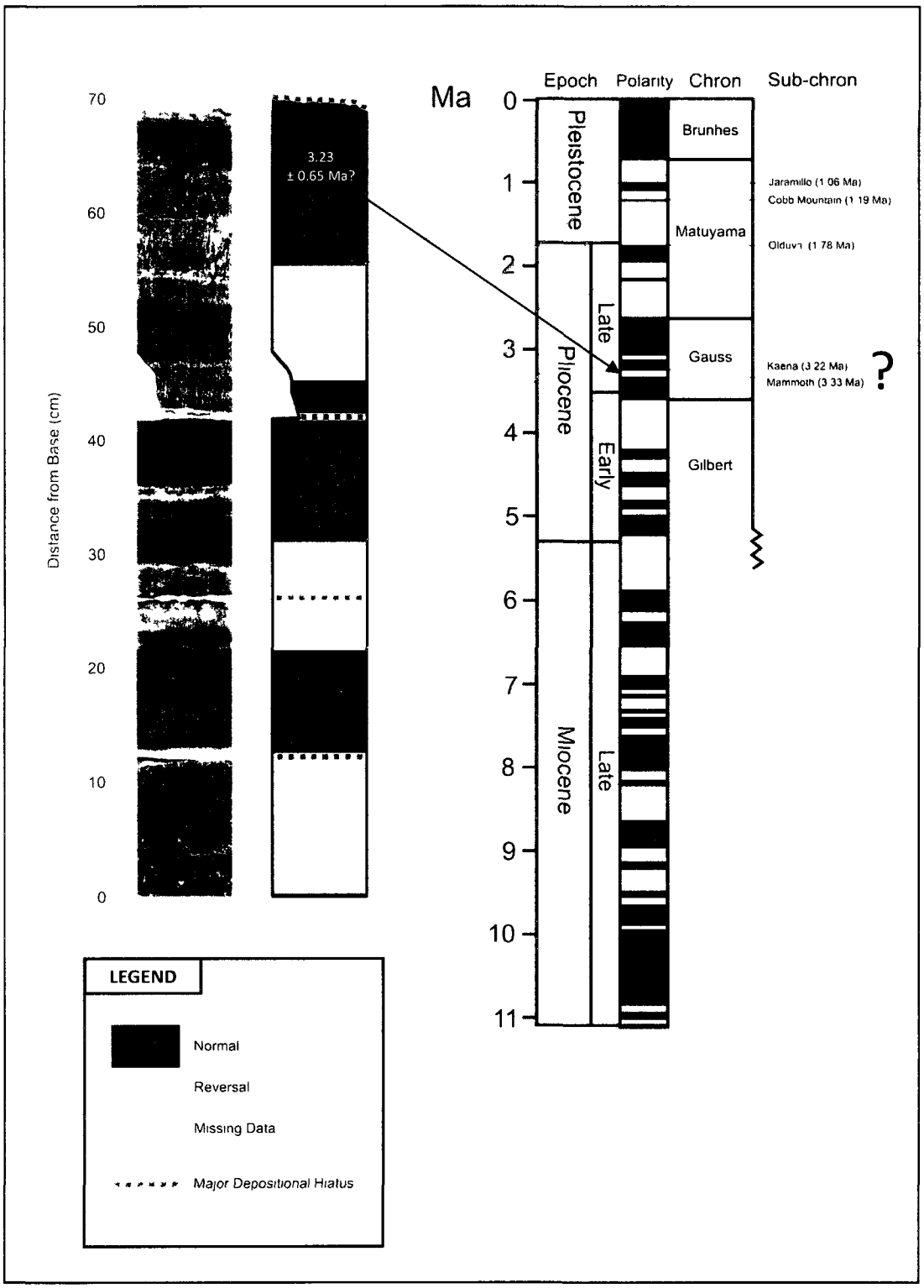

Figure 5.4. Paleomagnetic inversions of the BC1 flowstone (left) with conservative comparisons to the global geomagnetic timescale (right), revised from Mankinen & Dalrymple (1979) and Cooper *et al.* (2004).

5.3.3. Challenges of dating ancient speleothems

Obtaining a viable date from the BC1 flowstone proved to be the biggest challenge of this project, largely due to its antiquity. Relative dating methods, such as the two previously discussed in this chapter, are often associated with many uncertainties as certain assumptions must be made; regardless, they can still provide a glimpse into what the conditions were like at the time of deposition. A study on the pollen content of the BC1 flowstone, along with four other speleothems in Bear Cave, was completed by Lauriol *et al.* (1997); as the pollen spectra obtained from these speleothems may be reflective of the vegetation and climate that prevailed at the time of deposition. Although pollen counts were low, several arboreal taxa had been identified, including *Betula*, Alnus, *Picea*, along with 17 non-arboreal taxa, which are characteristic of the regional Holocene flora (Ritchie, 1984). These taxa are also found in late-Tertiary palynological records in the region (*see Section 2.1.2*), but the near absence of *Pinus* is difficult to explain as it too is dominant in late-Tertiary flora (Ritchie, 1984). The authors attribute its absence to its large grain size, which may have been filtered out of feedwaters. Nevertheless, these results indicate that the speleothems were deposited in a cool climate; however it is difficult to constrain the exact time of deposition from these data alone.

Absolute dating methods can provide a more detailed view at the time frame of deposition, but they too come with severe limitations, especially when dating older material. Previous dating attempts have confirmed that BC1 fell outside of the range of U-Th dating, which can only lead to one conclusion: the flowstone is older than 600 Ka (Lauriol *et al.*, 1997). U-Pb dating can extend this dating window, and was attempted by Anton Vaks at the University of Oxford in 2008; however the layers that were analysed were unsuitable for U-Pb dating due to inherently low uranium concentrations (Anton Vaks, personal communication). Electron spin resonance (ESR) dating was attempted at McMaster University in 1997 on the flowstone calcite, and also proved to be unsuccessful as the samples contain too much organic material.

After exhausting other dating options, He-dating was the next best method for dating the BC1 flowstone. The ages obtained from the MAPL Noble Gas laboratory indicate that the flowstone is late-Tertiary in age, which is in line with other age interpretations previously discussed in this chapter, and are congruent in the profile of the flowstone (*Figure 4.23*): 9.66-9.73 ± 0.83 Ma near the base of BC1-3, and 9.35-9.44 ± 0.52 Ma near the base of BC1-4. This

fitting as we would expect to see higher concentrations of ^{4}He in older samples as more alpha particles (α, or ^{4}He) are released over time. Overall, the inability to resolve the inherently low Th concentrations did not have a significant impact on the resulting age when using either the LOD of Th = Ø (a difference of ~0.11 Ma for BC1-3_{Base} and ~0.07 Ma for BC1-4_{Base}), as these discrepancies fall within the associated error for these dates (0.83 & 0.52 Ma respectively). The ^{4}He production rate (^{4}He atoms g^{-1} yr^{-1}) is calculated based on the decay constants and crustal ratios of U and Th (= (3.115 x 10^6 + 1.272 x 10^5) [U] + 7.710 x 10^5 [Th]; Ballentine & Burnard, 2002), where the contribution from Th is an order of magnitude less than that from U; in other words, the ^{4}He coming from Th is not as significant as that coming from U, therefore any small changes in Th should not make a significant difference in the resulting age.

The two dates from MAPL are rather close in age (with overlapping uncertainties) which suggests that the major discontinuity that separates these two blocks is of a relatively short duration. However, the nearly 6 Ma that separates BC1-4_{Base} (9.35 ± 0.52 Ma) and BC1-4_{Top} (3.23 ± 0.65 Ma, dated in Germany) is questionable. Growth rate estimates worked out from these two dates (0.03 μm yr^{-1}) also raise suspicion about the ages, as they are not typical of other cold-climate flowstone accretion rates. These do not compare well with the growth rate estimated from the epi-fluorescent study within BC1-3 (~24 μm yr^{-1}); however it is possible that these laminations may not have been annual, and may be representative of decadal-scale events. Accretion rates this low are not necessarily unheard of, but are rare: stalagmites from caves from central Texas dating back to the Last Glacial Maximum (~20 ka) exhibit growth rates as low as 0.5 μm yr^{-1} (Musgrove *et al.*, 2001), an order of magnitude greater in comparison. Growth rates of this magnitude may be indicative of prevailing cool and dry conditions at the time of deposition, yet they remain suspect because of their atypical nature.

The experimental procedure of ^{4}He gas extraction at the MAPL Noble Gas laboratory also confirmed that there was no significant loss of ^{4}He in ambient conditions, suggesting that the harder columnar-calcite crystals specifically chosen for analysis are fairly retentive of radiogenic ^{4}He, and likely experienced little to no diffusion of He, further strengthening the assertion that these fabrics are pristine. The sample dated near the top of the BC1 flowstone in Germany (~3.23 ± 0.65 Ma) was carried out previous to the detailed crystallographic study; referencing this crystallographic record (*Figure 4.9*) indicates that this date was completed within a zone of transitional calcite with infilling diagenic textures (*Columnar-with-Sparite*), which may explain the younger age. It is possible that this zone where ^{4}He was measured has

been subject to diffusion as the crystals here are not as tightly packed, resulting in a significantly younger age (lower amounts of radiogenic ^{4}He). Additionally, this fabric is one of many within the profile of BC1 found to be associated with diagenic alteration. If these secondary diagenic crystals are also retentive of radiogenic ^{4}He, this younger age may reflect the time during which the secondary in-filling took place; in other words, initial deposition may have taken place sometime around ~9 Ma, where some of the porous calcite fabrics were subject to later diagenesis, possibly around ~3 Ma.

A similar and ongoing He-dating study of the base of BC1-4 completed by Bassam Ghaleb and Daniele Pinti at the GEOTOP laboratory at UQAM in 2010 also show similar values to those measured in this study. *Table 5.3.* compares these results from both studies completed on the base of BC1-4. Th was found to be present in low concentrations (0.0052 ppm, measured by TIMS), which would explain why it fell below the LOD established in this study (0.0078 ppm, measured by ICP-MS). Using the same method outlined by Ballentine & Burnard (2002), the age derived from the values measured at UQAM is ~9.63 ± 0.26 Ma, which compares well with the 9.35 ± 0.52 Ma measured along the same horizon at MAPL. Age uncertainty doubles on account of the large error margin associated with using the LOD for Th; however the date reported from MAPL falls within the associated error range of one acquired at UQAM. These results confirm the dates obtained from MAPL, and stipulate that an age of ~9 Ma is more fitting for the BC1 flowstone.

Table 5.3. Radiogenic He-dating of BC1-4_{Base} at (I) MAPL and (II) UQAM

Laboratory	He^4 (ccSTP)	U (ppm)	Th (ppm)	He^4 atoms g^{-1} yr^{-1} [φ]	Age (Ma) [α]
(I) uOttawa (MAPL)	$2\ 209 \times 10^{7}$ ($\pm 1\ 1 \times 10^{8}$)	0 194 (± 0 0045)	0 0078 (- 0 0078)[β]	$6\ 350 \times 10^{5}$ ($\pm 1\ 58 \times 10^{4}$)	9 35 (± 0 52)
(II) UQAM (GEOTOP)	$2\ 441 \times 10^{7}$ ($\pm 6\ 46 \times 10^{9}$)	0 209 (± 0 0007)	0 0052 (± 0 00002)	$6\ 81 \times 10^{5}$ ($\pm 3\ 38 \times 10^{3}$)	9 63 (± 0 26)

[β] *Represents the LOD*
[φ] Using *Equation 5 (see Section 1 5)*
[α] Using *Equation 6 (see Section 1 5)*

Future focus should be aimed at continuing the He-dating chronology for the BC1 flowstone and resolving the innately low Th concentrations. More importantly, it may be worthwhile to attempt to date the calcite within the diagenically altered zones to see how they compare with the younger age obtained by the initial He-dating performed in Germany. In order

for this method to be successful, it is essential that Th concentrations can be detected with high precision. Th is present in the speleothem, but in very small quantities (below the 0.0078 ppm LOD) and difficult to analyze by ICP-MS with a high Ca matrix; therefore if a method can be employed to lower the LOD on Th or extract U and Th from Ca, radiogenic He-dating can be a powerful method to constrain the age estimates for the BC1 flowstone. Chelating resins are often used to extract and pre-concentrate U and Th from solution; however they remain fairly expensive and require a large time investment. Some ICP-MS have the capability of handling a high Ca matrix, therefore this may offer another venue for detecting low levels of Th. One prospective approach would be to pre-sample U and Th prior to analyzing He to ensure that there is a measureable quantity of the two. Thermal Ionization Mass Spectrometry (TIMS) offers a high precision technique for measuring isotopic compositions of Th at extremely low levels; however this method also involves time consuming sample preparation and is often prone to experimental error (Hoffmann *et al.*, 2008). Recent technical developments combining Laser ablation (LA) with ICP-MS (LA-ICP-MS) have enabled in situ measurements, bypassing these mechanical and chemical separation preparation procedures (Hoffmann & Mangini, 2003).

Other dating methods also deserve further exploration. As mentioned previously, ESR dating proved to be unfeasible for the speleothem calcite due to the inherently high organic content; however this method may prove possible for the quartz conglomerate grains at the base of the flowstone (Tissoux *et al.*, 2008) in order to constrain an upper limit on the age of BC1. Another venue that merits additional investigation is U-Pb dating. Because this dating method requires materials with high U and low Pb concentrations, new methodologies in this field also involve pre-screening U-rich layers that do not have too much common lead (not a result of radioactive decay) in order to identify datable layers (Pickering *et al.*, 2010; Woodhead *et al.*, 2010). These new technologies have placed stalagmites recovered near Richards Spur, Oklahoma in the early Permian period, which currently stand as the oldest speleothem to be directly dated by radiometric means (Woodhead *et al.*, 2010). It would be essential to target the unaltered layers of the harder *Palisade* and *Elongate Columnar* calcite within BC1, as recrystallization and diagenesis may have disturbed the initial decay chain. Establishing an internal chronology can be difficult given the resolution of this method (also a limitation with He-dating); nevertheless, it has immense potential to further refine the timeframe of deposition for the BC1 flowstone.

6. SUMMARY & CONCLUSION

A detailed study of the petrography and geochemistry of the flowstone from Bear Cave assisted in understanding the processes that took place at the time of and subsequent to speleothem deposition. The results confirm that a number of zones within the flowstone were not initially deposited under equilibrium conditions, which are largely represented by the softer microfabrics (*Micrite* & *Branched*). Furthermore, this study shows that although other zones may have originally been deposited in isotopic equilibrium, they have since been subject to diagenic modification, representing a two-stage deposition namely by secondary in-filling (*Columnar-with-Sparite* & *Columnar-with-Branched*). Complete recrystallization was also observed within several horizons (*Sparite*). All of the abovementioned processes ultimately compromise the integrity of the flowstone in terms of its paleoclimatic suitability, masking the original climate signal. Nonetheless, the pristine and coherent geochemical and petrographic records of the harder microfabrics imply that these sequences were deposited in isotopic equilibrium with their parent drip waters, and are representative of primary deposition as they are resistant to post-depositional diagenesis, preserving the original climate signal. This supports the hypothesis that harder facies are more reliable as geochemical proxies, thus these zones are ideal to use for detailed paleoclimatic and paleoenvironmental research.

Although geochemical proxies from the softer and transitional facies within the BC1 flowstone should not be used to infer detailed information about the paleo-environment/climate, they can still provide insight into the general environmental conditions of formation. Variations in speleothems fabric along with hiatuses in the depositional record can be related to changes in flow rate, as a result, these variations are indirectly linked to large scale spatial and temporal climatic and environmental changes on the land surface above (White, 2007, p.168). Thus the varying sequences of hard and soft calcite along the profile of BC1 likely represent alternating warm/wet and cool/dry conditions (respectively), and suggest that water flow has been considerably variable over the course of deposition.

Stable isotope variations within the more reliable calcite can provide a more detailed look at the time of deposition. $\delta^{18}O$ variations from these harder sections of the flowstone are comparable with interglacial deposits from the Rocky Mountains of Alberta, leading to the

conclusion that deposition took place under relatively cool climatic conditions, yet somewhat warmer than the prevailing conditions in the region today. This is also verified by $\delta^{13}C$ variations, which imply a marked organic presence at the time of deposition, confirming that permafrost must have been absent from vital feedwater paths (Lauriol *et al.*, 1997). The patterns of both isotopes within most of the harder sequences are relatively consistent, suggesting that these crystals were deposited from a constant drip source. In fact, the majority of the variability in the entire profile of the BC1 flowstone can be observed within the softer and transitional sequences, attributable to disequilibrium or diagenic processes. Comparing the reliable values from the harder calcite to those in zones identified to be associated with either disequilibrium conditions or diagenic modification shows that the former have generally more enriched $\delta^{18}O$ values, owing to evaporative processes, whereas the latter have more enriched $\delta^{13}C$ and more depleted $\delta^{18}O$ values. Therefore paleoclimatic interpretations from these zones would result in an under-estimations or over-exaggerations of actual depositional conditions.

The ages obtained from the radiogenic ^{4}He dating study at the MAPL Noble Gas laboratory also supports the assertion that the harder calcite proved to be more reliable. This study was completed on the harder palisade layers in the middle of the BC1 profile and revealed two concordant ages from the late-Miocene, centering around 9.35 ± 0.52 Ma and 9.66 ± 0.83 Ma, where the first date compares well with another obtained along the same horizon at UQAM (9.63 ± 0.26 Ma). These dates are also in line with geomorphic interpretations which speculate that the cave had reached an unsaturated state sometime during the mid-Miocene, inferred from the entrenchment of the Fishing Branch River, therefore speleothem deposition likely took place sometime shortly after this point in time. The younger age of 3.23 ± 0.65 Ma dated previously near the top of BC1 is located within a zone of diagenic calcite (unbeknown at the time of dating), therefore this age may be explained by diffusive loss of ^{4}He (resulting in a younger age), or if the grains are retentive of ^{4}He, the time during which recrystallization took place, resetting the decay chain.

This thesis emphasizes the importance of a complimentary petrographic study in speleothem geochemical studies used as paleoclimatic and paleoenvironmental proxies. Understanding stable isotope data from speleothems often calls upon interpretation of fractionation behaviour and identification of equilibrium deposition; however few studies

consider diagenic phenomena. The loss of primary textures in speleothems leads to important changes in mineralogy, textural attributes and geochemistry, ultimately masking the original climate signal. Despite the fact that this may have grave implications for misinterpretation of geochemical records, many speleothem studies overlook petrographic considerations.

With this being said, there is a need for more careful selection of speleothems as climate proxies. A complimentary petrographic study is essential for the identification of primary textures in speleothem used as detailed paleoenvironmental and paleoclimatic proxies. Likewise, the study of the geochemical signatures of individual microfabrics, like that examined in this thesis, can provide a potential tool for the recognition of the possible effects of environmentally related factors on isotope fractionation and diagenic modification (Frisia *et al.*, 2000). Hendy Tests are insufficient in this respect, as demonstrated in this thesis, where integration of both petrography and geochemistry is a more comprehensive assessment of the integrity of speleothem as climate proxies. Hence, this research constitutes as a basis for future studies in its application as establishing criteria for reliable speleothem proxies.

Speleothem records are intrinsically complex: their climatic sensitivity which makes them so attractive to paleo-research is confounded by the complicated processes that distort climate signals. However, with the use of carefully-constructed chronologies, they can be decoded to provide valuable proxy records, particularly in the case of ancient speleothem deposits, such as the one studied in this thesis. The flowstone from Bear Cave has enormous wealth in that the information preserved in this deposit will enrich our knowledge of the environmental and climatic conditions at the limits of Beringia when permafrost was absent from the area. This is particularly true as there are no records to date for this region in the late-Tertiary. Establishing a chronology from the BC1 flowstone can be difficult given the current limitations with absolute dating methods. With the high error ranges that surround these dates, best estimates place the flowstone to at least ~9 Ma. However the continued improvement of analytical tools and procedures may help to refine these uncertainties, having excellent implications for chronological applications. At any rate, this remains an area of immense potential.

References

Ayalon, A. Bar-Matthews, M. and Kaufman, A., 1999. Petrography, strontium, barium and uranium concentrations, and strontium and uranium isotope ratios in speleothem as paleoclimatic proxies: Soreq Cave, Israel. *The Holocene*, 9(6): 715-722.

Baker A. and Smart P.L., 1995. Recent flowstone growth rates: Field measurements in comparison to theoretical predictions, *Chemical Geology*, 122: 121-128.

Baker, A., Smart, P.L., Edwards, R.L., 1995. Paleoclimate implications of mass spectrometric dating of a British flowstone, *Geology*, 23: 309–312.

Baker, A. and Bradley, C., 2009. Modern stalagmite $\delta^{18}O$: Instrumental calibration and forward modelling, *Global and Planetary Change*, in press, doi: 10.1016/j.gloplacha.2009.05.002.

Baldini, J.U.L., McDermott, F., Hoffmann, D.L., Richards, D.A., Clipson, N., 2008. Very high-frequency and seasonal cave atmosphere pCO_2 variability: implications for stalagmite growth and oxygen isotope-based paleoclimate records. *Earth and Planetary Science Letters*, 272: 118–129.

Ballentine, C. and Burnard, P., 2002. Production, Release and Transport of Noble Gasses in the Continental Crust, *Reviews in Mineralogy and Geochemistry*, 47(1): 481-538.

Blyth, A.J., Baker, A., Collins, M.J., Penkman, K.E.H., Gilmour, M.A., Moss, J.S., Genty, D. and Drysdale, R.N., 2008. Molecular organic matter in speleothem and its potential as an environmental proxy. *Quaternary Science Reviews*, 27: 905-921.

Büdel, J., 1982. Climatic Geomorphology, Princeton University Press, New Jersey.

Clark, I.D. & Fritz, P., 1997. Environmental Isotopes in Hydrogeology, CRC Publishers, Florida.

Clark, I.D., Lauriol, B., 1992. Kinetic enrichment of stable isotopes in cryogenic calcites. *Chemical Geology*, 102: 217–228.

Cooper, R.A., Agterburg, F.P., Alloway, B.V., Beu, A.G., Crampton, J.S., Graham, I.J., Naish, T.R., Sadler, P.M. & Wilson, G.S., 2004. Chapter 1, Introduction. in Cooper, R.A. (ed.), 2004. The New Zealand Geological Timescale. Institute of Geological and Nuclear Sciences Monograph 22, pp. 1-28.

Couchoud, I. 2007. Interet de analyse petrographique des speleothems pour les reconstitutions paleoenvironnementales. *Karstologia,* 50: 9-18.

Courtillot, V., Gallet, Y., Le Mouël, Fluteau, F. And Genevey, A., 2007. Are there connections between the Earth's magnetic field and climate?, *Earth and Planetary Science Letters*, 253: 328-339.

Cruz Jr., F.W., Burns, S. J. Jercinovic, M., Karmann, I., Sharp, W.D., and Vuille, M., 2007. Evidence of rainfall variations in Southern Brazil from trace element ratios (Mg/Ca and Sr/Ca) in a Late Pleistocene stalagmite. *Geochimica et Cosmochimica Acta*, 71: 2250-2263.

Desmarchelier, J.M., Hellstron, J.C., McCulloch, M.T., 2006. Rapid Trace element analysis of speleothem by ELA-ICP-MS, *Chemical Geology*, 231: 102-117.

Dickson, J.A.D., 1991. Disequilibrium carbon and oxygen isotope variations in natural calcite. *Nature*, 353: 842-844.

Dickson, J.A.D., 1995. Isotopic homogeneity among nonequivalent sectors of calcite: comment. *Geology*, 24: 95.

Dickson, J.A.D., 1997. Synchronous intracrystalline $\delta^{13}C$ and $\delta^{18}O$ differences in natural calcite crystals, *Mineralogical Magazine*, 61: 243-248.

Dorale, J.A. and Liu, Z., 2009. Limitations of Hendy Test Criteria in Judging the paleoclimatic suitability of speleothems and the need for replication, *Journal of Cave and Karst Studies*, 71(1): 73-80.

Dowsett, H.J., Barron, J.A., Poore, R.Z., Thompson, R.S., Cronin, T.M., Ishman,S.E., and Willard, D.A., 1999. Pliocene Paleoenvironmental Reconstruction: U.S. Geological Survey PRISM II Project, Open File Report 99-535., http://ccsr.columbia.edu/paleoclimate/pliocene/index.html.

Dreybrodt, W., 2004. 'Erosion Rates: Theoretial, Models', p. 323, *Encyclopedia of Caves and Karst Science*. New York.

Drysdale, R., Zanchetta, G., Hellstrom, J., Maas, R., Fallick, A., Pickett, M., Cartwright, I., Piccini, L., 2006. Late Holocene drought responsible for the collapse of Old World civilizations recorded in an Italian cave flowstone, *Geology*, 34: 101–104.

Duk-Rodkin, A. and Hughes, O.L., 1994. Tertiary-Quaternary drainage of the pre-glacial Mackenzie Basin, *Quaternary International*, 22/23: 221-241.

English, J.M. and Johnston, S.T., 2004. The Laramide Orogeny: What Were the Driving Forces? *International Geology Review*, 46: 833-838.

Environment Canada, Monthly data report 2004: Old Crow Station, [http://climate.weatheroffice.gc.ca/climateData/monthlydata_e.html?Prov=XX&timeframe=3&StationID=1582&Month=1&Day=1&Year=2004&cmdB1=Go]. April 2009.

Environment Yukon, "Ni'iinlii Njik (Fishing Branch) Territorial Park", [http://environmentyukon.gov.yk.ca/parksconservation/FishingBranch.php]. June 2010.

Fairchild, I.J., Borsato, A., Tooth, A.F., Frisia, S., Hawkesworth, C.J., Huang, Y., McDermott, F. and Spiro, B., 2000. Controls on trace element (Sr-Mg) compositions of carbonate cave waters: implications for speleothem climatic records, *Chemical Geology*, 166: 255-269.

Fairchild, I.J., Baker, A., Borsato, A., Frisia, S., Hinton, R.W., McDermott, F. and Tooth, A.F., 2001. High-resolution, multiple trace-element variation in speleothems, *Journal of the Geological Society (London)*, 158: 831-841.

Fairchild, I.J., Smith, C.L., Baker, A., Fuller, L., Spötl, C., Mattey, D., McDermott, F., and E.I.M.F., 2006. Modification and preservation of environmental signals in speleothems, *Earth Science Reviews*, 75: 105– 153.

Fairchild, I.J. and McMillan, E.A., 2007. Speleothem as indicators of wet and dry periods. *International Journal of Speleology*, 36(2): 69-74.

Fairchild, I.J., and Treble, P.C., 2009. Trace elements in speleothem as recorders of environmental change, *Quaternary Science Reviews*, 28: 449-468.

Fantidis, J., and Ehhalt, D.H., 1970. Variations of the carbon and oxygen isotopic composition in stalagmites and stalactites: evidence of non-equilibrium isotopic fractionation. *Earth and Planetary Science Letters*, 10: 136-144.

Farley, K., 2002. (U-Th)/He Dating: Techniques, Calibrations, and Applications, *Reviews in Mineralogy and Geochemistry*, 47(1): 819-844.

Folk, R.L. and Assereto, R., 1976. Comparative fabrics of length-slow and length-fast calcite and calcitized aragonite in a Holocene speleothem, Carlsbad Caverns, New Mexico, *Journal of Sedimentary Petrology*, 46(3): 486-496.

Ford, D. & Williams, P.W., 1989. Karst Geomorphology and Hydrology, Kluwer Academic Publishers.

Fornaca-Rinaldi, E., Panichi, C., and Tongiorgi, E., 1968. Some causes of variations of the isotopic compositions of carbon and oxygen on cave concretions. *Earth and Planetary Science Letters*, 4: 321-324.

Frappier, A.B. 2007. A stepwise screening system to select storm-sensitive stalagmites: Taking a targeted approach to speleothem sampling methodology, *Quaternary International*, doi: 10.1016/j.qua int.2007.09.042.

Frisia, S., 1996. Petrographic evidences of diagenesis in speleothems: some examples. *Speleochronos*, 7: 21-30.

Frisia, S., Borsato, A., Fairchild, I.J. and McDermott, F., 2000. Calcite fabrics, growth mechanisms, and environments of formation in speleothems from the Italian Alps and southwestern Ireland, *Journal of Sedimentary Research*, 70: 1183-1196.

Gascoyne, M., Latham, A.G., Harmon, R.S., Ford, D.C. 1983. The antiquity of Castleguard Cave, Columbia Icefields, Alberta, Canada. *Arctic and Alpine Research*: 15(4): 463-470.

Genty, D, 1992. Les spéléothemes du tunnel de Godarville (Belgique)—un exemple exceptionnel de concrétionnement moderne—intérêt pour l'étude de la cinétique de la precipitation de la calcite et de sa relation avec les variations d'environnement, *Speleochronos,* 4: 3-29.

Gonzalez, L.A., and Lohmann, K.C., 1987. Controls on mineralogy and composition of spelean carbonates: Carlsbad Caverns, New Mexico, *in* James, N.P., and Choquette, P.W. (eds.) Paleokarst: New York, Springer-Verlag, p. 81-101.

Greene, S., Battye, N., I. C., Kotzer, T., Bottomley, D., 2008. Canadian Shield brine from the Con Mine, Yellowknife, NT, Canada: Noble gas evidence for an evaporated Palaeozoic seawater origin mixed with glacial meltwater and Holocene recharge, *Geochimica et Cosmochimica Acta*, 72(16): 4008-4019.

Harmon, R.S., Atkinson, T.C., Atkinson, J.L., 1983. The mineralogy of Castleguard Cave, Columbia Icefields, Alberta, Canada. *Arctic and Alpine Research*: 15: 503–516.

Harmon, R.S., Schwarcz, H.P., Gascoyne, M., Hess, J.W. and Ford, D.C., 2007. Paleoclimate information from speleothems: The present as a guide to the past. In *Studies of Cave Sediments – Physical and Chemical Records of Paleoclimate*. Kluwer Academic, New York, p. 199-226.

Heginbottom, J.A., Dubreuil M.A., and Harker, P.A., 1995. Canada permafrost, in National Atlas of Canada *5th edition*, Natural Resources Canada, Ottawa, Canada.

Hendy, C.H., 1971. The isotopic geochemistry of speleothems, *Geochimica et Cosmochimica Acta*, 35: 801-824.

Hill, C.A. and Forti, P., 1997. Cave minerals of the world. National Speleological Society, Huntsville, USA.

Hill, C.A. and Forti, P. 2004. 'Speleothems: Carbonate', p. 690, *Encyclopedia of Caves and Karst Science*. New York.

Hoffmann, D., Mangini, A., 2003. A method for coupled ESR/U-series dating of teeth showing post-depositional U-loss, *Quaternary Science Reviews*, 22: 1367-1372.

Hoffmann, D.L., Paterson, B.A. and Jonckerre, R., 2008. Measurements of the uranium concentration and distribution in a fossil equid tooth using fission tracks, TIMS and laser ablation ICPMS: Implications for ESR dating, *Radiation Measurements*, 43: 5-13.

Hoffmann, D.L., Spötl, C. and Mangini, A., 2009. Micromill and in situ laser ablation sampling techniques for high spatial resolution MC-ICPMS U-Th dating of carbonates, *Chemical Geology*, 259: 253-261.

Holzkämper, S., Spötl, C., Mangini, A., 2005. High-precision constraints on timing of Alpine warm periods during the middle to late Pleistocene using speleothem growth periods, *Earth and Planetary Science Letters*, 236: 751–764.

Hopkins, D.M., Matthews, J.V., Schweger, C.E. and Young, S.B., 1982. Paleoecology of Beringia, Academic Press, New York.

Hopley, P.J., Marshall, J.D. and Latham, A., 2009. Speleothem preservation and diagenesis in South African hominin sites: Implications for paleoenvironments and geochronology, *Geoarchaeology: An International Journal*, 24(5): 519-547.

Hopley, P.H., Marshall, J.D., Weedon, G.P., Latham, A.G., Herries, A. and Kuykendall, K.L., 2007. Orbital forcing and the spread of C_4 grasses in the late Neogene: stable isotope evidence from South African speleothems, *Journal of Human Evolution*, 53: 620-634.

Huang, Y., Fairchild, I.J., Borsato, A., Frisia, S., Cassidy, N.J., McDermott, F., and Hawkesworth, C.J., 2001. Seasonal variations in Sr, Mg and P in modern speleothem (Grotta di Ernesto, Italy). *Chemical Geology*, 175: 429-448.

Jo, K., Woo, K.S., Cheng, H., Edwards, L.R., Wang, Y., Kim, R. And Jiang, X., 2010. Textural and carbon isotopic evidence of monsoonal changes recorded in a composite-type speleothems from Korea since MIS 5a, *Quaternary Research*, 74: 100-112.

Johnson, K.R., Hu, C., Belshaw, N.S., Henderson, G.M., 2006. Seasonal trace-element and stable-isotope variations in a Chinese speleothem: The potential for high-resolution paleomonsoon reconstruction, *Earth and Planetary Science Letters*, 244: 394-407.

Kim S.T., and O'Neil, J.R., 1997. Equilibrium and nonequilibrium oxygen isotope effects in synthetic carbonates, *Geochimica et Cosmochimica Acta*, 61: 3461–3475.

Kendall, A.C. and Broughton, P.L., 1978. Origin of fabrics in speleothems composed of columnar calcite crystals, *Journal of Sedimentary Petrology*, 48(2): 519-538.

Klein, R.T., and Lohmann, K.C., 1995. Isotopic homogeneity among non-equivalent sectors of calcite, *Geology*, 23: 633-636.

Kolodny, Y., Bar-Matthews, M., Ayalon, A., McKeegan, K.D., 2003. A high spatial resolution $\delta^{18}O$ profile of a speleothem using an ion-microprobe, *Chemical Geology*, 197: 21–28.

Lachniet, M.S., 2009. Climatic and environmental controls on speleothem oxygen-isotope values, *Quaternary Science Reviews*, 28: 412-432.

Lacelle, D., 2007. Environmental setting, (micro)morphologies and stable C–O isotope composition of cold climate carbonate precipitates—a review and evaluation of their potential as paleoclimatic proxies, *Quaternary Science Reviews*, 26: 1670–1689.

Latham, A.G., Ford, D.C., Schwarcz, H.P. and Birchall, T., 1988. Secular variation from Mexican stalagmites: their potential and problems, *Physics of the Earth and Planetary Interiors, 56:* 34-48.

Lauriol, B., Ford, D.C., Cinq-Mars, J., and Morris, W.A., 1997. The chronology of speleothem deposition in northern Yukon and its relationships to permafrost, *Canadian Journal of Earth Science*, 34: 962-911.

Lauritzen, S.E., 1995. High-resolution paleotemperature proxy record for interglaciation based on Norwegian speleothems, *Quaternary Research*, 43:133-146.

Laurtizen, S.E., 1996. Calibration of speleothem stable isotope against historical records: a Holocene temperature curve for north Norway?, *in* Lauritzen, S.-E., ed., Climate *Change: The Karst Record: Karst Water Institute, Special Publication*, 2: 78–80.

Lauritzen, S. and Lundberg, J., 1999. Speleothems and climate: a special issue of *The Holocene*, *The Holocene*, 9(6): 643-647.

Lichti-Federovich, S., 1973. Palynology of six sections of late Quaternary sediments from the Old Crow river, Yukon Territory, *Canadian Journal of Earth Science*, 51: 553-564.

Lohmann, K.C., 1988. Geochemical patterns of meteoric diagenetic systems and their application to studies of paleokarst. In N.P. James & P.W. Choquette (Eds.), Paleokarst. New York: Springer-Verlag.

Mankinen, E.A., and Dalrymple, G.B., 1979. Revised geomagnetic polarity time scale for the interval 0-5 m.y. B.P., *Journal of Geophysical Research*, 84: 615-626.

Mattey, D., Lowry, D., Duffet, J., Fisher, R., Hodge, E., Frisia, S., 2008. A 53 year seasonally resolved oxygen and carbon isotope record from a modem Gibraltar speleothem: reconstructed drip water and relationship to local precipitation, *Earth and Planetary Science Letters*, 269: 80-95.

Matthews Jr , J Schweger, C , and Hughes, O , 1990 The last (Koy-Yukon) interglaciation in the northern Yukon Evidence from unit 4 at Ch'ijee s Bluff, Bluefish basin, *Geography physique et Quaternaire*, 44(3) 341 362

Marshall, D , Ghaleb, B , Countess, R and Gabities, J , 2009 Preliminary paleoclimate reconstruction based on a 12,500 year old speleothem from Vancouver Island, Canada stable isotopes and U-Th disequilibrium dating, *Quaternary Science Reviews*, 28 2507-2513

Martin-Garcia, R , Alonza-Zarza, A M and Martin Perez, A , 2009 Loss of primary texture and geochemical signatures in speleothems due to diagenesis Evidences from Castanar Cave, Spain, *Sedimentary Geology*, 221 141 149

McDermott F Frisia S , Huang Y , Longinelli A Spiro B Heaton, T H E , Hawkesworth, C J Borsato, A , Keppens, E , Fairchild, I J , Van Der Borg, K , Verheyden, S , and Selmo, E , 1999 Holocene climate variability in Europe Evidence from $\delta^{18}O$, textural and extension-rate variations in three speleothems *Quaternary Science Reviews*,18 1021-1038

McDermott, F , 2004 Paleo-climate reconstruction from stable isotope variations in speleothems a review, *Quaternary Science Reviews*, 23 901 918

McGarry, S F and Baker, A , 2000 Organic acid fluorescence applications to speleothem palaeoenvironmental reconstruction *Quaternary Science Reviews*, 19 1087 1101

Meyer M C Spotl C Mangini A 2008 The demise of the Last Interglacial recorded in isotopically dated speleothems from the Alps *Quaternary Science Reviews* 27 476 496

Meyer M C Cliff R A Spotl, C , Knipping, M and Mangini A , 2009 Speleothems from the earliest Quaternary Snapshots of paleoclimate and landscape evolution art the northern rim of the Alps *Quaternary Science Reviews*, 28 1374 1391

Miller, G H , Brigham Grette, J , Alley, R B , Anderson, L , Bauch, H A , Douglas, M S V , Edwards, M E , Elias, S A , Finney, P B , Fitzpatrick, J J , Funder, S V , Herbert, T D , Hinzman, L D , Kaufman, D S , MacDonald, G M , Polyak, L , Robock, A , Serreze, M C , Smol, J P , Spielhagen, R , White, J W C , Wolfe, A P and Wolff, E W , 2010 Temperature and precipitation history of the Arctic, *Quaternary Science Reviews*, 29 1679 1715

Musgrove M , Banner, J L Mack, L E , Combs, D M , James, E W , Cheng, H And Edwards, R L , 2001 Geochronology of late Pleistocene to Holocene speleothems from central Texas Implications for regional paleoclimate, *GSA Bulletin* 113(12) 1532 1543

Norris, D 1978 Geology Porcupine River, Yukon Territory Geological Survey of Canada Map 1522A, scale 1 250000

Paquette, J and Reeder, R J , 1990 New types of compositional zoning in calcite Insights into crystal growth mechanisms *Geology,* 58 1244 1247

Park, W C , 1967 Early Diagenetic Framboidal Pyrite, Bravoite and Vaesite from the Cave-In Rock Fluorspar District, Southern Illinois, *Mineralium Deposita*, 2 372-375

Perrette Y Delannoy J J Desmet M , Lignier, V and Destombes, J L 2005 Speleothem organic matter content imaging The use of a Fluorescence Index to characterize the maximum emission wavelength *Chemical Geology*, 214 193-208

Pickering, R., Kramers, J., Partridge, T., Kodolanyi, J. and Pettke, T., 2010. U-Pb dating of calcite-aragonite layers in speleothems from hominin sites in South Africa by MC-ICP-MS, *Quaternary Geochronology*, doi: 10/1016.

Railsback, L. B. 2000. An Atlas of Speleothem Microfabrics, University of Georgia Laboratory for Speleothem Studies, Department of Geology, University of Georgia, Athens, Georgia, U.S.A. http://www.gly.uga.edu/speleoatlas/SAindex1.html

Reeder, R. J., and Grams, J. C., 1987. Sector zoning in calcite cement crystals: Implications for trace element distributions in carbonates, *Geochimica et Cosmochimica Acta*, 51: 187-194.

Reeder, R.J., Valley, J.W., Graham, C.M. and Eiler, J.M., 1997. Ion microprobe study of oxygen isotopic compositions of structurally non-equivalent growth surfaces on synthetic calcite, *Geochimica et Cosmochimica Acta*, 61: 5057-5063.

Richards, D., Bottrell, S., Cliff, R., Ströhle, K. And Rowe, P., 1998. U-Pb dating of a speleothem of Quaternary age, *Geochimica et Cosmochimica Acta*, 62: 3683-3688.

Ritchie, J.C., 1984. Past and present vegetation of the far north-west Canada. University of Toronto Press, Toronto.

Roberts, M.S., Smart, P.L., and Baker, A., 1998. Annual trace element variations in a Holocene Speleothem. *Earth and Planetary Science Letters*, 154: 237-246.

Sancho, C., Pena, J.L., Mikkan, R., Osácar, C. and Quinif, Y. 2004. Morphological and speleothemic development in Brujas Cave (Southern Andean Range, Argentine): palaeoenvironmental significance, *Geomorphology*, 57: 367-384.

Sharp, Z., 2007. Principles of Stable Isotope Geochemistry, Pearson Prentice Hall, Upper Saddle River, NJ.

Shopov, Y.Y. 2004. 20 Years of Speleothem Paleoluminescence records of environmental changes: An overview. *International Journal of Speleology*, 33(1): 5-17.

Smart, C.C. and Ford, D.C., 1983. The Castleguard karst, main ranges, Canadian Rocky Mountians, *Journal of Hydrology*, 61: 193-197.

Smith, C.L., Fairchild, I.J., Spötl, C., Frisia, S., Borsato, A., Moreton, S.G., and Wynn, P.M., 2009. Chronology building using objective identification of annual signals in trace element profiles of stalagmites, *Quaternary Geochronology*, 4: 11-21.

Spötl, C., Mangini, A., Frank, N., Eichstädter, R., Burns, S.J., 2002. Start of the last interglacial period at 135 ka: evidence from a high alpine speleothem, *Geology*, 30: 815–818.

Spötl, C. and Mattey, D., 2006. Stable isotope microsampling of speleothems for palaeoenvironmental studies: a comparison of microdrill, micromill and laser ablation techniques, *Chemical Geology*, 235: 48–58.

Spötl, C. and Mangini, A., 2007. Speleothems and paleoglaciers, *Earth and Planetary Science Letters*, 254: 323–331.

Tarnocai, C. and Schweger, C.E., 1991. Late Tertiary and Early Pleistocene paleosols in Northwestern Canada. *Arctic*, 44: 1-11.

Thibodeau, P., 1988. Queslques aspects de la géomorphology karstique du basin de la Haute Porcupine, Nord du Yukon. 119p. M.A. Thesis, University of Ottawa, Ottawa, ON.

Tipper, E.T., Louvat, P., Capmas, F., Galy, A. and Gaillerdet, J., 2008. Accuracy of stable Mg and Ca isotope data obtained by MC-ICP-MS using the standard addition method, *Chemical Geology*, 257: 65-75.

Tissoux, H., Toyoda, S., Christophe, F., Coinchet, P., Takada, M., Bahain, J-J. and Despriée, J. 2008. ESR dating of sedimentary quartz from two pleistocene deposits using Al and Ti-centers, *Geochronometria*, 30: 23-31.

Treble, P., Shelley, J.M.G. and Chappell, J., 2003. Comparison of high resolution sub-annual records of trace elements in a modern (1911–1992) speleothem with instrumental climate data from southwest Australia, *Earth and Planetary Science Letters*, 216: 141-153.

Treble, P.C., Chappell, J., Gagan, M.K., McKeegan, K.D., Harrison, T.M., 2005. In situ measurement of seasonal $\delta^{18}O$ variations and analysis of isotopic trends in a modem speleothem from southwest Australia. Earth and Planetary Science Letters, 233: 17-32.

Turgeon, T. And Lundberg, J., 2001. Chronology of discontinuities and petrology of speleothems as paleoclimatic indicators of the Klamath Mountains, southwest Oregon, USA, *Carbonates and Evaporites*, 16(2): 153-167.

Turgeon, S.C. and Lundberg, J., 2007. Establishing a speleothem chronology for southwestern Oregon. In *Studies of Cave Sediments – Physical and Chemical Records of Paleoclimate*. Kluwer Academic, New York, p. 273-302.

Van Beynen, P., Bourbonniere, R., Ford, D. and Schwarcz, H., 2001. Causes of colour and fluorescence in speleothem. *Chemical Geology*, 175: 319-341.

Van Beynen, P.E., Soto, L., Pace-Graczky, K., 2007. Paleoclimate reconstruction derived from speleothem strontium and $\delta^{13}C$ in Central Florida, *Quaternary International*, doi: 10.1016/j.quaint.2007.03.019

Wahl, H.E., Fraser, B.B., Harvey, R.C., and Maxwell, J.B., 1987. Climate of the Yukon. Climatological Studies No. 40, 323 p. Atmospheric Service, Environment Canada, Toronto.

White, W.B., 2007. Paleoclimate records from speleothem in limestone caves. In *Studies of Cave Sediments – Physical and Chemical Records of Paleoclimate*. Kluwer Academic, New York, p. 135-175.

White, W.B., 2009. The evolution of Appalacian fluviokarst: Competition between stream erosion, cave development, surface denudation, and tectonic uplift, *Journal of Cave and Karst Studies*, 71(3): 159-167.

Woodhead, J., Reisz, R., Fox, D., Drysdale, R., Hellstrom, J., Maas, R., Cheng, H. And Edwards, R., 2010. Speleothem climate records from deep time? Exploring the potential with an example from the Permian, *Geology*, 38(5): 455-458.

Yonge, C.J., Ford, B.C., Gray, J., and Schwarcz, H.P. 1985. Stable isotope studies of cave seepage water. *Chemical Geology*, 58: 97-185.

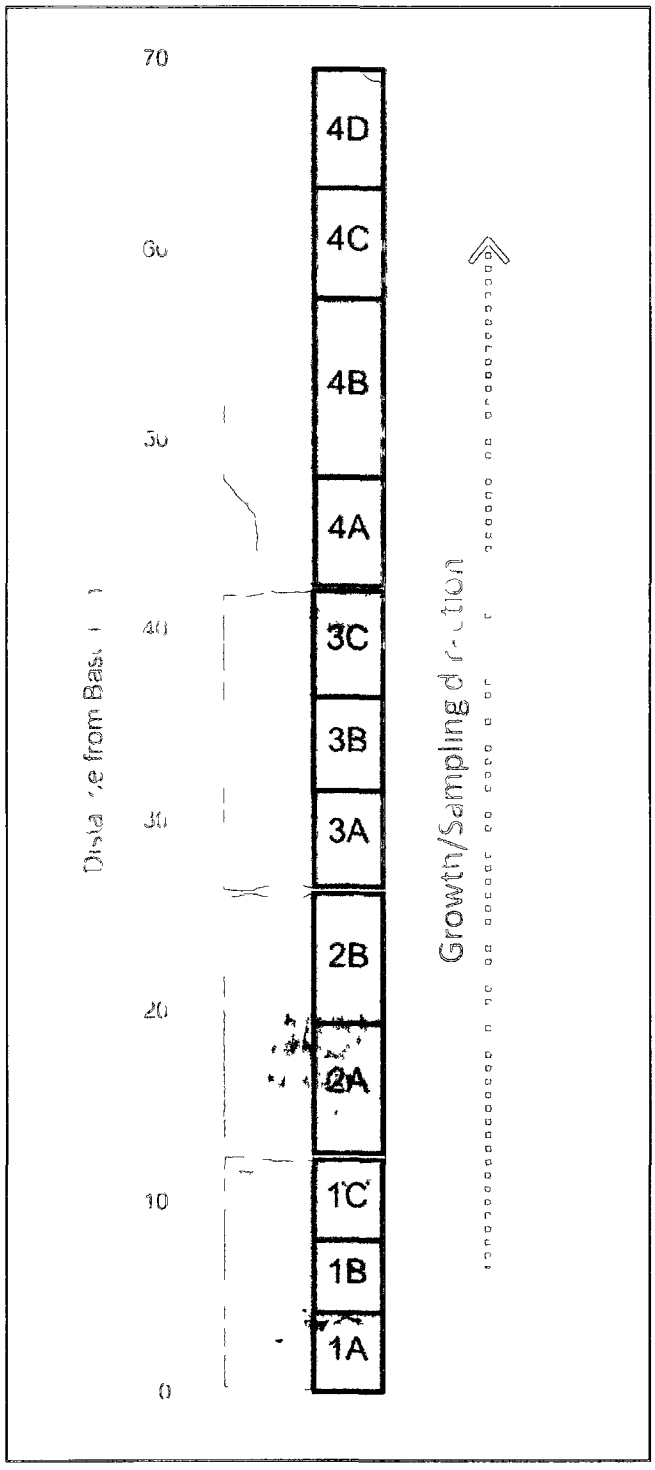

Figure A. Locations of thin section transects for crystallographic study.

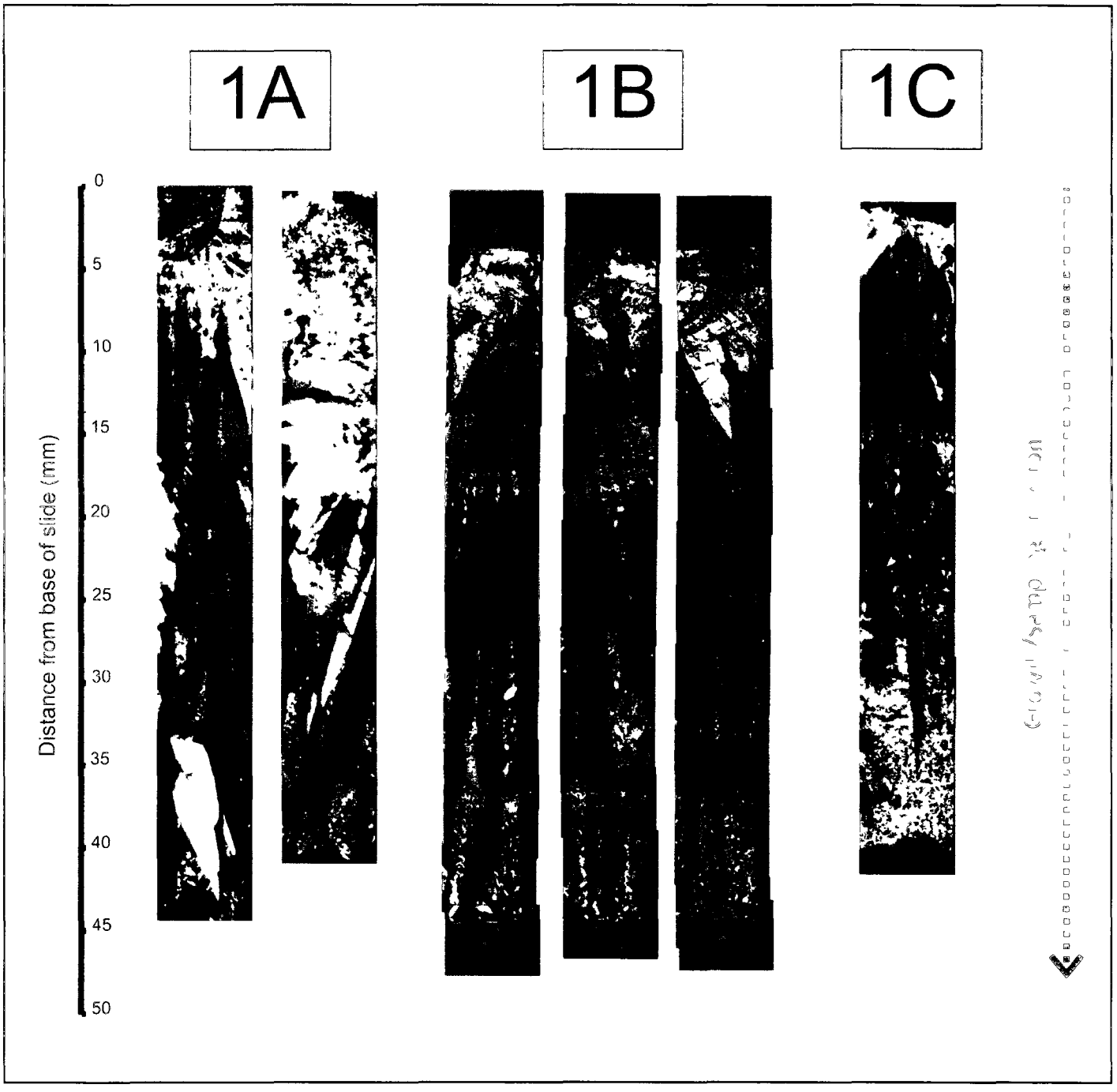

Figure B. Crossed-polar petrographic transects of calcite crystals in BC1-1.

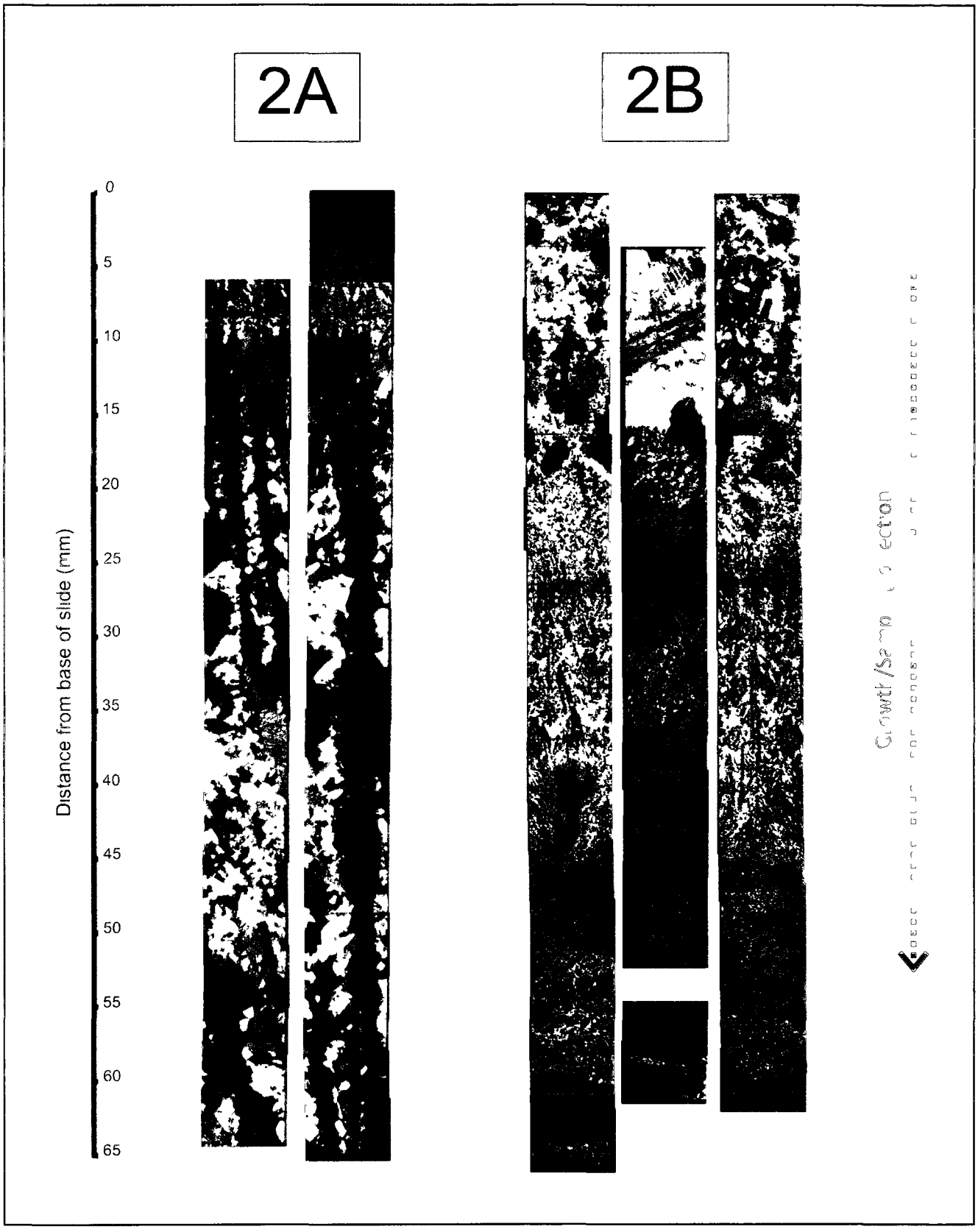

Figure C. Crossed-polar petrographic transects of calcite crystals in BC1-2.

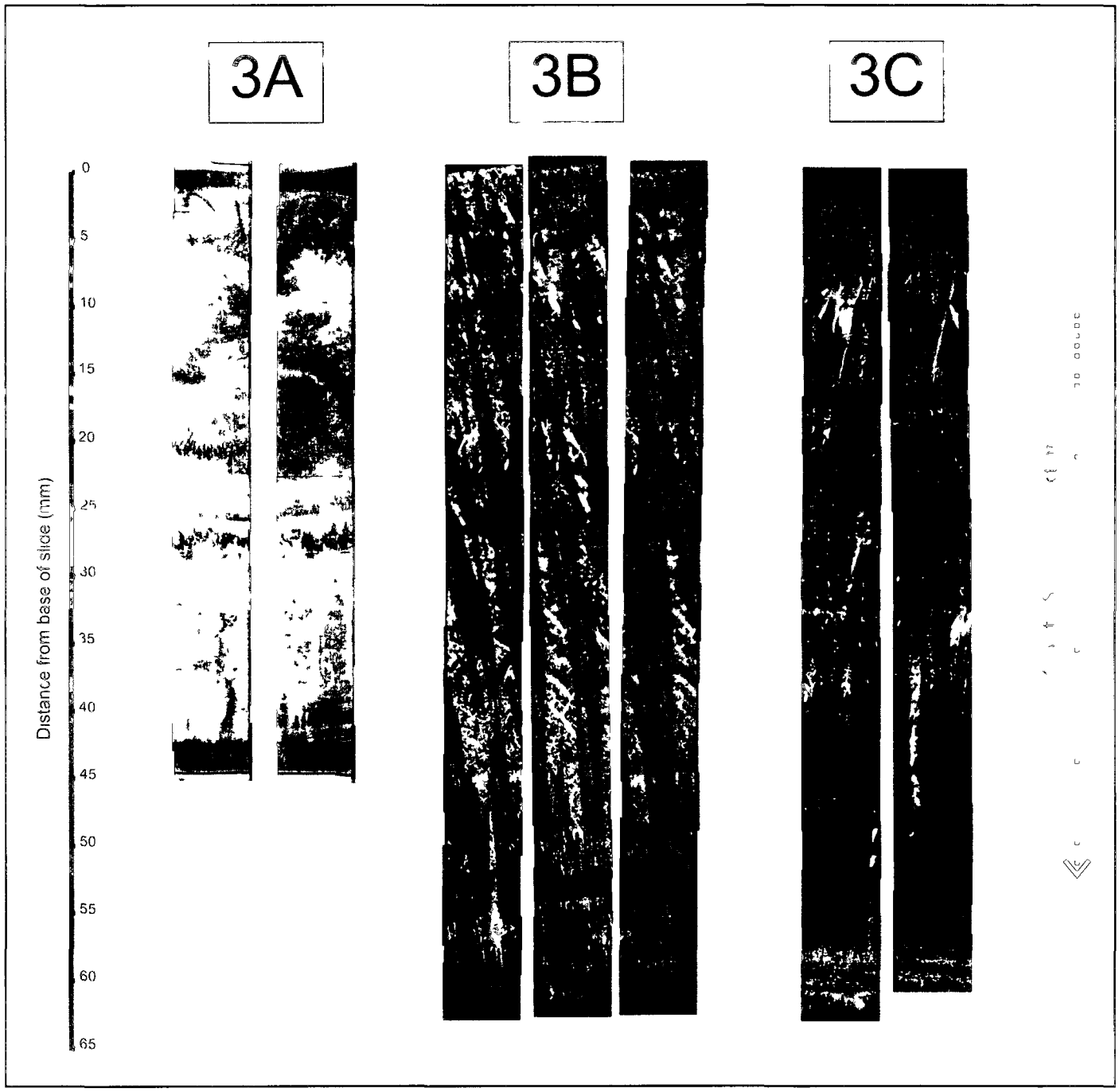

Figure D. Crossed-polar petrographic transects of calcite crystals in BC1-3.

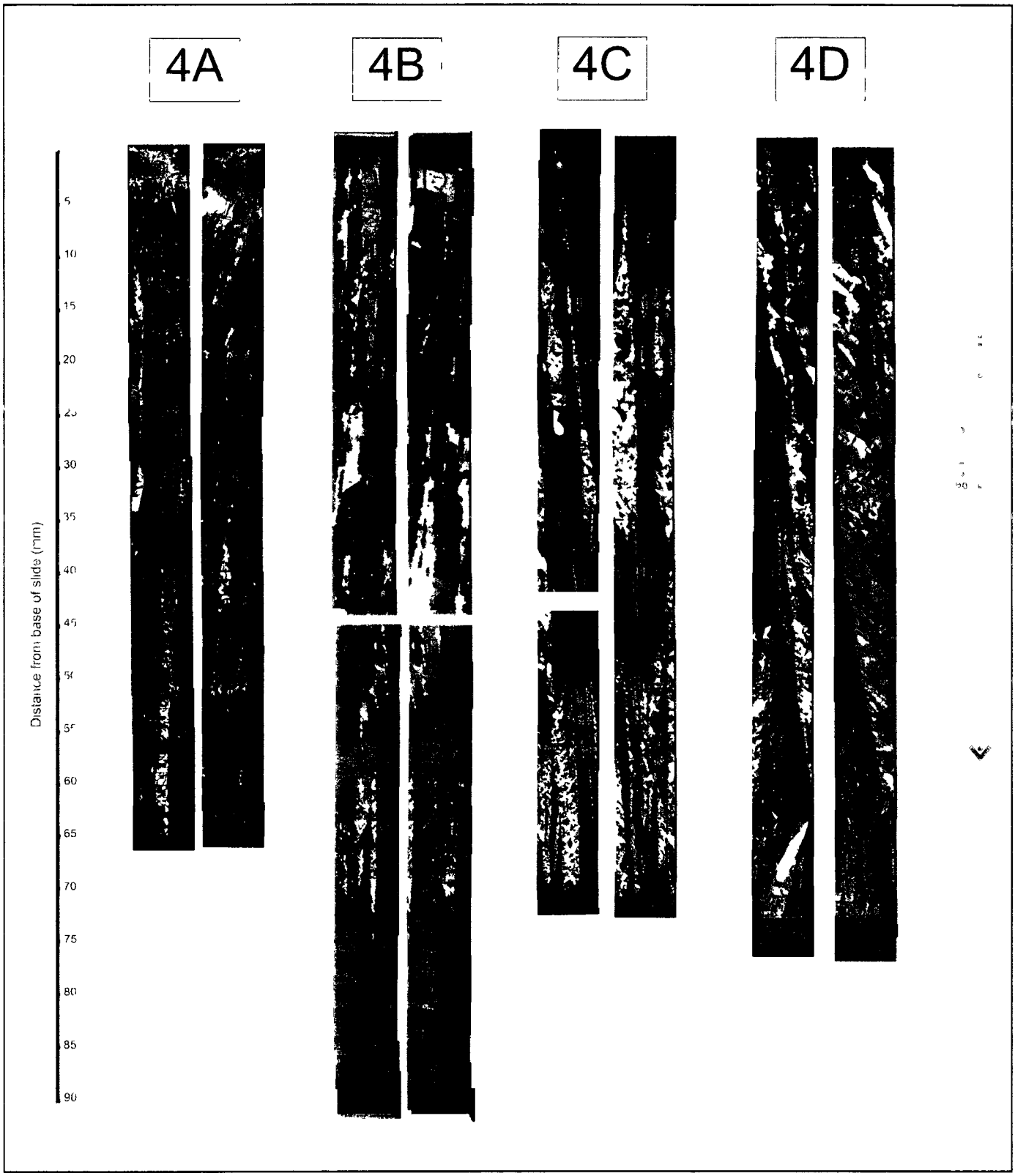

Figure E. Crossed-polar petrographic transects of calcite crystals in BC1-4.

Appendix II – ICP-AES procedural methodology

i. Sample collection and preparation

Powdered samples for both ICP-AES and stable isotope analysis were obtained on thick sections using the same method as outlined in *Section 3.2.1* for each successive lamina for the two transects. Samples for ICP-AES were prepared using approximately 1.5 mg powder digested with 0.25 ml of concentrated HNO3, and heated to 50 °C for 1 hour to ensure all components, trace metals in particular, were dissolved into the solution. 1.0 ml of 20 ppm Sc was subsequently added to each of the samples as an internal standard, followed by 3.0 ml of distilled deionized water, to bring the total solution volume to approximately 4.5 ml, and ultimately bring the internal Sc standard concentration to approximately 4.5 ppm.

ii. Calibration standards (by gravimetry)

A total of three series of calibration standards were prepared for the analysis: i) 0, 0.5, 1.0, 2.0, 5.0, 10 ppm in 5% HNO3 + 5.0 ppm Sc internal standard; ii) 0, 0.5, 1.0, 2.0, 5.0, 10 ppm in 5% HNO3 + Ca (matrix matched standard, approximately 100ppm in solution) + 5.0 ppm Sc internal standard; iii) and a series of Ca standards of 0, 20, 50 and 100 ppm. The matrix matched standard solution series (ii) were only utilized in this experiment as a check for drift (*see Figure 4.12*). Several sample solutions were prepared without the added Sc internal standard to determine if there is any naturally occurring Sc present in the flowstone, and later determined that the inherent concentration levels were below the limits of detection.

iii. Data processing and analysis

All calibration solutions and samples were run by an auto-sampler on the ICP-AES machine in the Department of Earth Sciences at the University of Ottawa. The series of calibration standards were run first, followed by several blank solutions which were used to calculate the limits of detection (LOD = 3 x σ_B). The BC1-3 flowstone samples were subsequently analyzed followed by the set of Ca calibration standards. Known sample concentrations (5.0 ppm and 10.0 ppm) were run at regular intervals (every 10 measurements) to check for instrumental drift, with a blank solution run immediately afterward in order to flush the

system. No significant drift was observed with the known sample concentrations, which suggests that instrumental drift did not influence the results.

Prior to analysis, specific parameters were set and an optimization was carried out in order to maximize efficiency. The pump rate was run at 12 rpm with a 30 s delay, with a 10 s replicate read time including 6 replicates and a viewing height of 10 mm. Several lines were chosen for each analyte, with specific attention payed to avoid interferences. Intensities for each of the analytes were obtained at different RF powers, ranging from 0.9 to 1.4 at 0.1 increments. From this, the best internal standard scandium line (out of a possible 5) was chosen for each analyte line based on the highest correlation coefficient of the intensities of varying RF powers. Each of the analyte lines were corrected based on the best matched Sc internal standard line that behaved the same way. Corrections for the matrix effect and noise (i.e. transport efficiency, effective power, etc.) were completed by comparing the ratio of observed vs. expected Sc internal standard concentration added to each individual sample. The best line(s) for each analyte were chosen by eliminating the ones that fell below the LOD, and by comparing the correlation coefficients of several lines for one analyte (*see Figure F*). The concentrations for the best fitting lines were averaged to obtain final concentrations for each analyte. For example, four lines were chosen for Sr: Sr 216.596, Sr 407.771, Sr 421.552, and Sr 460.733. Sr 460.733 was uncalibrated and eliminated from the analysis. The intensities of the three remaining lines were plotted against one another in *Figure F*, and it was found that Sr 407.771 and Sr 421.552 behaved in a similar way as they produced the highest correlation coefficient (R^2 = 0.9976), therefore the corrected concentrations of these two lines were averaged to produce the final Sr concentrations. Final concentrations of the powder were obtained by multiplying the solution concentrations by the dilution factor (approximately 3000x).

Ca concentrations were initially found to be outside of the calibration range. The concentrations were revised and obtained at a later date by recalibrating the instrument. Inherent Sc concentrations in the flowstone determined from the 6 random samples were found to be fairly insignificant (1-800 ppb), and fairly close, if not below, the LOD and therefore were disregarded. Corrections for inherent Sc concentrations would have been problematic due to variability and very low concentrations, and difficult as it would have been impossible to determine the exact concentration of inherent Sc that was present in each of the samples that were analysed with the Sc internal standard already added.

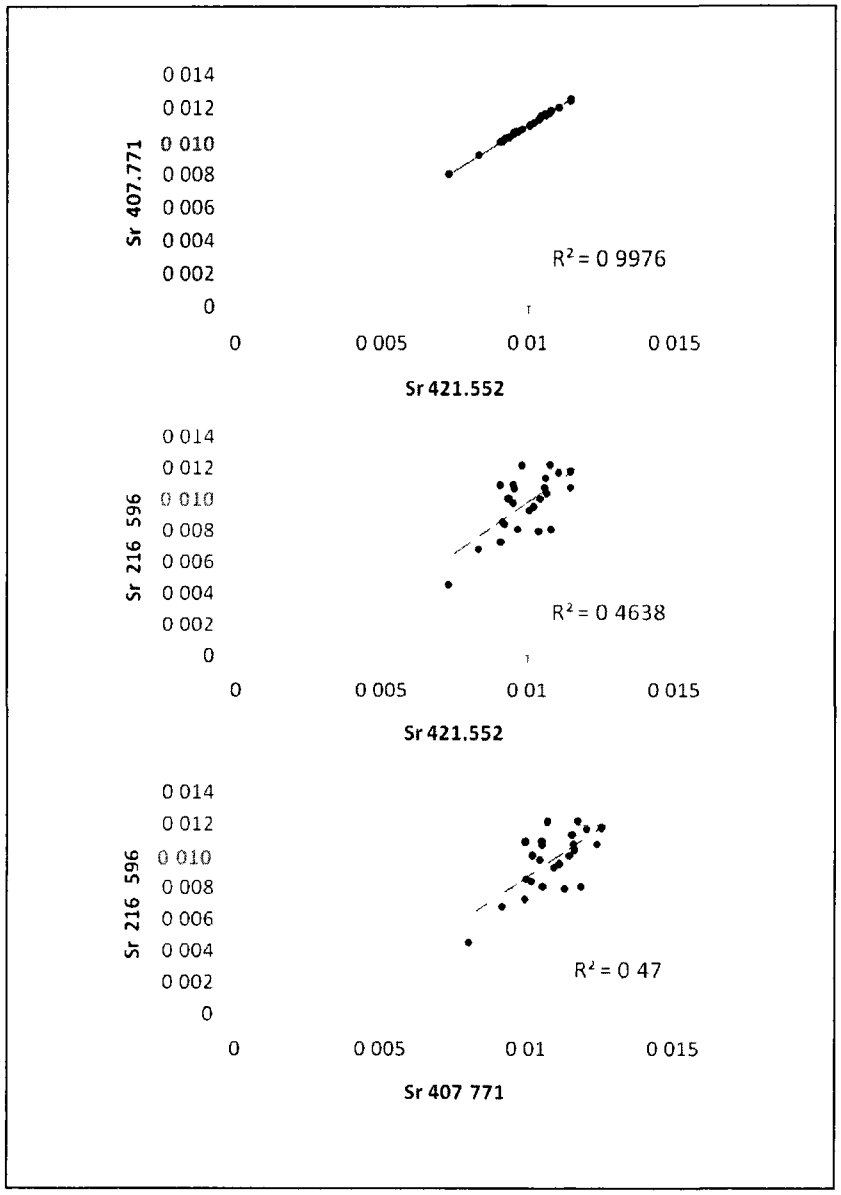

Figure F. Determination of best Sr lines

Appendix III – Stable isotope and crystallographic record for BC1

Block	Distance from Base (mm)	$\delta^{18}O$ (‰)	$\delta^{13}C$ (‰)	Microfabric
BC1-1	0.0	-17.72	-6.33	2
	10.0	-18.89	-5.94	8
	30.0	-17.92	-6.33	5
	40.0	-17.80	-5.96	5
	55.0	-17.08	-5.95	8
	65.0	-16.81	-4.50	5
	75.0	-16.69	-5.85	5
	85.0	-16.38	-4.82	8
	90.0	-16.59	-4.31	8
	100.0	-16.84	-3.97	5
	112.0	-17.16	-5.61	2
BC1-2	113.5	-16.80	-5.61	1
	115.0	-15.17	-5.81	1
	116.5	-16.04	-4.35	1
	118.0	-16.16	-4.09	4
	119.5	-18.50	-5.98	4
	121.0	-18.61	-6.46	5
	122.5	-18.82	-6.56	5
	124.0	-18.40	-5.52	7
	125.5	-18.60	-5.28	8
	127.0	-18.80	-5.24	8
	128.5	-18.85	-5.69	8
	130.0	-18.33	-5.84	5
	131.5	-18.18	-5.33	5
	133.0	-18.64	-5.51	5
	134.5	-18.62	-5.41	5
	136.0	-18.48	-5.34	5
	137.5	-18.44	-5.31	5
	139.0	-19.05	-5.89	5
	140.5	-18.81	-5.93	5
	142.0	-18.62	-5.90	5
	143.5	-19.26	-5.90	5
	145.0	-19.03	-5.83	5
	146.5	-18.83	-5.42	5
	148.0	-18.90	-5.38	5
	149.5	-18.76	-5.25	5
	151.0	-18.80	-5.43	5
	152.5	-18.85	-5.52	5
	154.0	-18.78	-5.39	5
	155.5	-19.09	-5.49	5
	157.0	-18.84	-5.41	5
	158.5	-18.61	-5.56	5
	160.0	-18.68	-5.60	5
	161.5	-18.86	-5.91	5
	163.0	-18.69	-5.96	5
	164.5	-18.74	-5.98	5
	166.0	-19.02	-6.24	5
	167.5	-18.94	-6.00	5

Block	Distance from Base (mm)	$\delta^{18}O$ (‰)	$\delta^{13}C$ (‰)	Microfabric
BC1-2	169.0	-19.19	-5.96	5
	170.5	-19.17	-6.15	5
	172.0	-18.89	-6.22	5
	173.5	-17.06	-6.30	5
	175.0	-17.09	-6.09	5
	176.5	-17.01	-5.62	5
	178.0	-17.12	-5.20	5
	179.5	-17.53	-5.68	5
	181.0	-17.58	-5.04	5
	182.5	-17.44	-5.04	5
	184.0	-17.59	-4.96	5
	185.5	-17.46	-4.84	2
	187.0	-17.37	-4.85	2
	188.5	-17.40	-4.87	2
	190.0	-17.34	-4.64	2
	191.5	-17.26	-4.18	2
	193.0	-17.54	-4.56	2
	194.5	-17.77	-4.52	2
	196.0	-17.34	-5.31	2
	197.5	-17.51	-5.82	2
	199.0	-17.70	-6.22	2
	200.5	-17.67	-6.00	4
	202.0	-17.21	-5.60	3
	203.5	-15.68	-5.48	3
	205.0	-16.46	-6.05	3
	206.5	-16.59	-6.91	3
	208.0	-16.35	-6.45	3
	209.5	-16.44	-5.60	3
	211.0	-16.79	-6.43	3
	212.5	-15.52	-6.32	3
	214.0	-16.72	-6.91	3
	215.5	-16.92	-6.88	3
	217.0	-17.24	-6.49	3
	218.5	-16.77	-6.37	3
	220.0	-16.96	-6.41	3
	223.0	-17.17	-6.60	3
	224.5	-17.30	-6.21	3
	226.0	-16.92	-6.00	3
	227.5	-16.82	-6.69	1
	229.0	-16.81	-6.82	1
	230.5	-16.73	-6.92	1
	232.0	-16.84	-6.47	1
	233.5	-16.41	-6.01	1
	235.0	-16.46	-4.77	1
	236.5	-16.57	-4.90	1
	238.0	-16.72	-5.18	1
	239.5	-16.91	-4.68	1
	241.0	-17.01	-4.63	1

Block	Distance from Base (mm)	$\delta^{18}O$ (‰)	$\delta^{13}C$ (‰)	Microfabric
BC1-2	242.5	-17.11	-4.52	1
	244.0	-16.72	-5.54	1
	245.5	-16.73	-5.72	1
	247.0	-16.78	-6.16	1
	248.5	-17.60	-7.36	2
BC1-3	250.0	-16.84	-6.20	1
	251.5	-16.86	-5.77	1
	253.0	-17.25	-6.25	1
	254.5	-17.26	-6.26	1
	256.0	-17.10	-6.23	1
	257.5	-17.14	-6.48	1
	259.0	-16.64	-5.32	1
	260.5	-16.86	-5.76	1
	262.0	-16.72	-5.38	1
	263.5	-17.01	-5.88	1
	265.0	-16.51	-5.09	1
	266.5	-16.50	-4.89	1
	268.0	-16.52	-5.00	1
	269.5	-16.90	-6.80	1
	271.0	-16.65	-7.12	1
	272.5	-16.71	-7.26	1
	274.0	-17.12	-6.99	3
	275.5	-17.59	-5.78	3
	277.0	-17.75	-6.08	1
	278.5	-17.32	-7.75	1
	280.0	-17.34	-7.73	1
	281.5	-16.10	-6.06	4
	283.0	-16.33	-7.85	7
	284.5	-15.63	-6.60	7
	286.0	-16.05	-6.75	7
	287.5	-14.98	-6.68	7
	289.0	-15.77	-6.86	7
	290.5	-15.44	-6.75	7
	291.5	-16.55	-7.00	7
	293.0	-16.48	-6.90	7
	294.5	-16.60	-6.88	5
	296.0	-16.72	-6.89	5
	297.5	-16.95	-6.58	5
	299.0	-17.48	-6.54	5
	302.0	-17.45	-6.69	5
	303.5	-17.28	-6.77	5
	305.0	-16.78	-6.82	5
	306.5	-17.22	-6.78	5
	308.0	-17.20	-6.87	5
	309.5	-17.20	-7.03	5
	311.0	-16.90	-6.81	5
	312.5	-17.41	-6.51	5
	314.0	-17.41	-7.07	5
	315.5	-17.26	-7.07	6
	317.0	-17.15	-6.80	6
	318.5	-16.70	-6.91	6
	320.0	-16.28	-6.81	6

Block	Distance from Base (mm)	$\delta^{18}O$ (‰)	$\delta^{13}C$ (‰)	Microfabric
BC1-3	321.5	-14.88	-5.89	6
	323.0	-15.26	-5.95	6
	324.5	-16.10	-5.66	6
	326.0	-16.77	-6.04	6
	327.5	-16.81	-6.24	6
	329.0	-17.03	-6.27	6
	330.5	-16.39	-6.12	7
	332.0	-16.66	-5.90	7
	333.5	-16.61	-6.32	7
	335.0	-16.27	-6.20	7
	336.5	-17.30	-6.35	7
	338.0	-17.24	-6.03	7
	339.5	-17.13	-6.07	7
	340.0	-17.88	-6.28	7
	341.5	-17.04	-6.96	3
	343.0	-17.36	-7.09	3
	345.0	-17.30	-7.51	3
	346.5	-16.98	-7.36	3
	348.0	-16.47	-7.16	4
	350.0	-16.86	-7.57	7
	351.5	-16.53	-7.10	7
	353.0	-17.32	-6.97	7
	355.0	-17.53	-6.57	7
	356.5	-17.38	-6.35	7
	358.0	-17.22	-5.89	7
	360.0	-17.39	-5.31	7
	361.5	-16.95	-5.59	7
	363.0	-17.06	-5.48	7
	365.0	-17.10	-5.42	7
	366.5	-17.02	-5.25	7
	368.0	-17.26	-5.40	7
	370.0	-17.37	-6.10	7
	371.5	-17.32	-6.04	7
	373.0	-17.06	-5.81	7
	375.0	-17.20	-5.73	5
	376.5	-16.82	-5.77	5
	378.0	-16.80	-5.95	5
	380.0	-17.04	-5.71	5
	381.5	-16.98	-5.36	5
	383.0	-17.31	-5.68	8
	385.0	-17.26	-5.56	8
	386.5	-17.35	-5.43	8
	388.0	-17.73	-5.54	8
	390.0	-18.40	-5.55	8
	391.5	-17.23	-5.35	8
	393.0	-17.28	-5.45	8
	395.0	-17.24	-5.04	8
	396.5	-17.09	-5.20	8
	398.0	-16.99	-5.44	8
	400.0	-16.75	-6.29	1
	401.5	-16.92	-5.78	1
	405.0	-17.13	-6.60	1

Block	Distance from Base (mm)	$\delta^{18}O$ (‰)	$\delta^{13}C$ (‰)	Microfabric
BC1-3	408.0	-17.00	-6.52	1
	410.0	-16.73	-4.82	4
BC1-4	415.0	-18.15	-6.95	7
	420.0	-17.44	-6.23	8
	425.0	-17.48	-6.84	8
	430.0	-17.56	-6.80	8
	435.0	-16.85	-6.68	8
	440.0	-16.98	-6.89	8
	445.0	-16.75	-6.76	8
	450.0	-16.65	-7.09	8
	455.0	-17.76	-7.02	8
	460.0	-17.51	-6.75	8
	465.0	-17.52	-6.94	8
	470.0	-17.52	-6.86	8
	475.0	-17.24	-6.33	8
	480.0	-17.14	-6.71	8
	485.0	-16.74	-7.01	8
	490.0	-16.87	-6.86	8
	495.0	-16.72	-7.04	8
	500.0	-17.03	-6.97	8
	505.0	-16.96	-6.48	8
	510.0	-17.02	-6.46	8
	515.0	-16.96	-6.40	8
	520.0	-16.66	-6.26	8
	525.0	-17.41	-5.76	5
	530.0	-16.38	-5.96	5
	535.0	-16.52	-5.83	8
	540.0	-16.68	-5.67	8

Block	Distance from Base (mm)	$\delta^{18}O$ (‰)	$\delta^{13}C$ (‰)	Microfabric
BC1-4	545.0	-17.04	-5.34	8
	550.0	-16.78	-5.20	8
	555.0	-17.00	-4.56	5
	560.0	-16.79	-4.52	5
	565.0	-16.74	-4.11	5
	570.0	-16.46	-4.95	5
	575.0	-16.69	-4.60	5
	580.0	-16.07	-3.83	5
	585.0	-16.32	-4.39	5
	590.0	-16.35	-4.88	5
	595.0	-16.23	-5.07	5
	600.0	-16.08	-5.80	5
	605.0	-16.22	-5.69	5
	610.0	-16.62	-5.73	5
	615.0	-16.23	-5.71	5
	620.0	-16.42	-5.80	5
	625.0	-16.37	-4.85	5
	630.0	-16.48	-5.26	5
	635.0	-16.89	-5.26	5
	640.0	-17.08	-6.18	6
	645.0	-17.11	-6.42	6
	650.0	-17.37	-6.87	6
	655.0	-17.69	-7.46	6
	660.0	-17.47	-6.48	6
	665.0	-17.48	-7.48	6
	670.0	-17.76	-8.21	5
	675.0	-17.49	-7.83	6
	680.0	-18.52	-8.32	1

Microfabric number key: 1-Micrite, 2-Sparite, 3-Branched, 4-Short Columnar, 5-Columnar-with-Sparite, 6-Columnar-with-Branched, 7-Elongate Columnar, 8-Palisade.

Appendix IV – Comparison of paleomagnetic and stable isotope variations

Solar forcing has long since been established as a significant driver of climate, yet recent research have appealed to magnetic variability as a cause of climatic change (Courtillot *et al.*, 2007). The sun governs the overall behaviour of the ionosphere, magnetosphere and external geomagnetic field, effectively modulating incoming fluxes of cosmic rays, which are increasingly recognized as potential drivers of changes in cloud cover and albedo. Scientists postulate that changes in paleomagnetic intensity may be related to changes in the magnetic field of the Earth, in turn related the modulation of cosmic ray fluxes and low cloud cover, where paleointensity maxima may correlate with cosmic ray flux minima, hence lesser cloud cover and albedo and higher temperatures (Courtillot *et al.*, 2007). Although these assumptions remain up for debate, it was speculated that the BC1 flowstone may exhibit this phenomena, where increases (decreases) in paleomagnetic intensities may correlate with higher (lower) temperatures, thus increases (decreases) in vegetation, or more enriched (depleted) $\delta^{13}C$ values.

Variations in stable isotopes ($\delta^{18}O$ & $\delta^{13}C$) and paleomagnetic variables (intensity, declination and moment) along the length of the BC1 flowstone are illustrated in *Figure G*. Comparisons of these variations proved to be difficult as there are several limitations associated with both data. Firstly, the intensity variations are those carried by the sample and only represent a relative variation of the Earth's magnetic field assuming the content of the magnetic materials within the sample remains constant (Jean-Pierre Pozzi, personal communication, 2010). Laboratory calibration needs to be carried out on these same samples in order to verify this, which has yet to be completed; therefore the relative variations in intensity expressed here cannot be related to the Earth's magnetic field. Attempts were made to normalize the magnetic content of the minerals in the sample with magnetic susceptibility, but they were too weak and even diamagnetic. It may however still be interesting to correlate the geochemistry with the intensity of the sample as it may or may not be related to climate; however this link remains ambiguous.

In addition to this, the issue of sampling resolution must be resolved in order to make any inferences about relations to climate. Paleomagnetic variations were sampled along the profile of the BC1 flowstone at 1.0 cm intervals, where stable isotope variations were sampled at 1.5 or 5.0 cm intervals (*Figure G*), where areas sampled at a higher resolution may imply a noisy isotopic signature.

Finally, the issue of using reliable vs. unreliable fabrics is also of concern. The majority of the profile of BC1 is eliminated if comparison between geochemistry and paleomagnetism is limited exclusively to the reliable zones (marked in brown in *Figure G*). The reliable zones may not necessarily apply with respect to paleomagnetic variations; for fabrics deposited under non-equilibrium conditions, it may not be of importance as they may be representative of initial deposition where the magnetic minerals in the rock may have been preserved. This may not be true for the horizons that were diagenically modified, as the quantities of magnetic minerals are so small, any change to these particles (i.e. introduction of newer quantities or removal by secondary infiltration waters) may affect the magnetic properties of the sample.

From this initial study, there are no conclusive correlations between the geochemical and paleomagnetic variations of the BC1 flowstone; however this may be shadowed by the sampling uncertainties and does merit additional investigation.

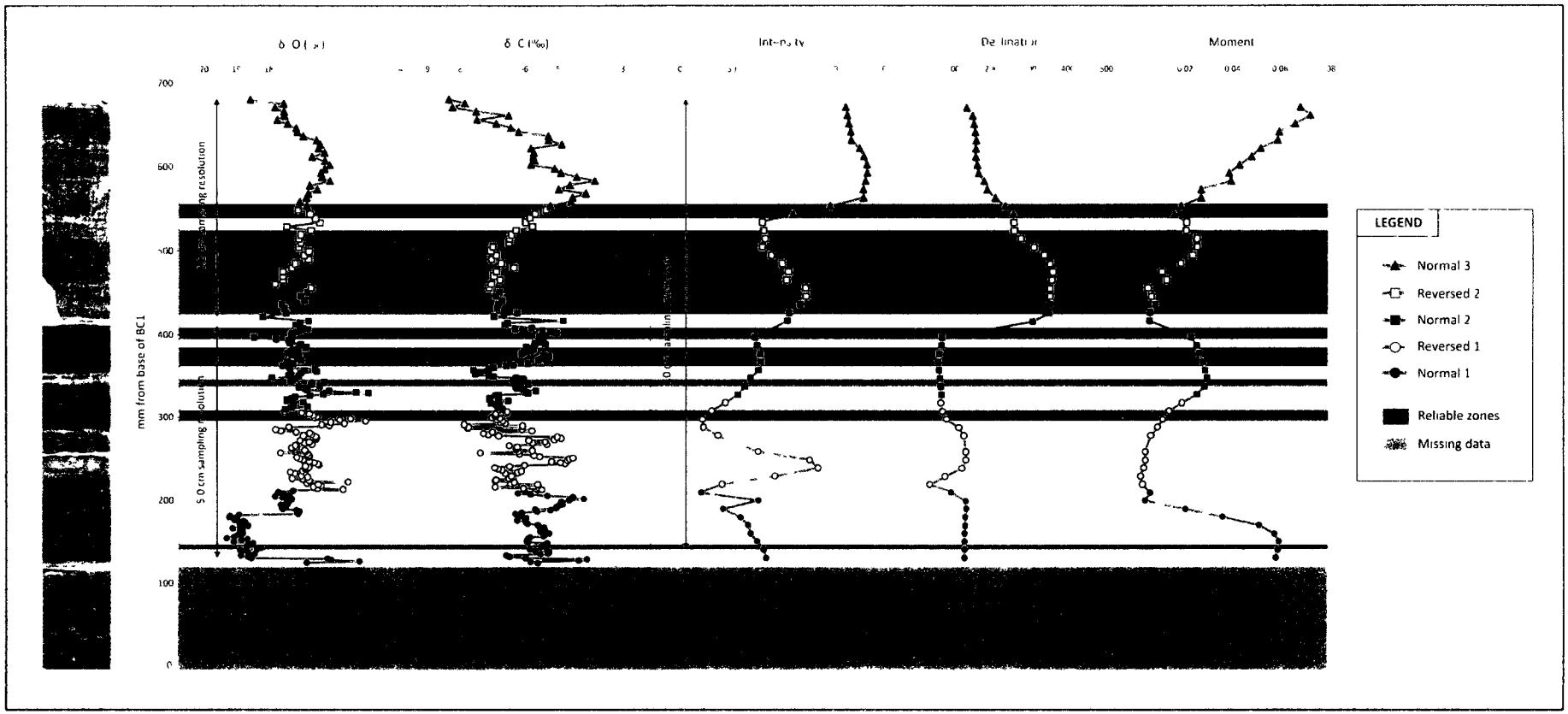

Figure G. Comparison of stable isotopes ($\delta^{18}O$ & $\delta^{13}C$) and paleomagnetic variables (intensity, declination & moment).